Development of Polymeric Abradable Coatings for Aero Engine Applications

Nezhla Madabadi

A Thesis in
The department
of
Mechanical, Industrial and Aerospace Engineering

Presented in the Partial Fulfillment of the
Requirements for the Degree of Master of Applied Science (Mechanical Engineering)
at Concordia University
Montreal, Quebec, Canada

October 2024

CONCORDIA UNIVERSITY

SCHOOL OF GRADUATE STUDIES

This is to certify that the thesis prepared

By: Nezhla Madabadi

Entitled: Development of Polymeric Abradable Coatings for Aero Engine Applications

and submitted in the partial fulfillment of the requirements of the degree of

Master of Applied Science (Mechanical Engineering)

complies with the regulations of the University and meets the accepted standards with respect to originality and quality.

Signed by the final Examining Committee:

______________________________ Chair

Dr. Muthukumaran Packirisamy

_____________________________ Examiner

Dr. Mehdi Hojjati

_____________________________ Examiner

Dr. Pantcho Stoyanov

______________________________ Thesis Supervisor

Dr. Farjad Shadmehri

Approved by ____

Dr. Martin D. Pugh

Chair of Department of Mechanical, Industrial and Aerospace Engineering

____

Dr. Mourad Debbabi

Dean, Gina Cody School of Engineering and Computer Science

Abstract

Development of Polymeric Abradable Coatings for Aero Engine Applications
Nezhla Madabadi

In the field of aerospace engineering, the enhancement of engine performance and reliability under extreme conditions is paramount. This study is dedicated to the development of polymeric abradable coatings for fan core and Low-Pressure Compressor stage. These coatings are specifically engineered to wear away in a controlled manner, thus reducing friction and improving the sealing capabilities of engines, a critical factor for optimizing efficiency.

The research evaluates two primary material types: thermosets and thermoplastics, comparing them against two commercially available materials which are epoxy based and named as ref1 and ref2. The assessment involves a series of tests, including erosion resistance, tribology pin-on-flat testing, and rub rig testing, to gauge the performance of these materials under operational stress.

Furthermore, the study explores the incorporation of various fillers—Graphite, Silicone Powder, PTFE, Carbon Nanotubes, Milled Carbon Fiber, Aramid Fiber, and Hollow Glass Microspheres—into selected thermoset. These fillers are evaluated at two distinct concentrations to ascertain their influence on erosion resistance.

Through this research, effective filler concentrations were identified, optimizing the balance between wear resistance and erosion resistance. Notably, a formulation comprising Epoxy with 10% PTFE, and 0.1% Carbon Nanotubes introduced as a potential abradable coating, exceeding the commercial benchmarks in terms of both erosion resistance and friction reduction.

This investigation underscores the critical role of precise material selection in the development of advanced abradable coatings that enhance the efficiency and longevity of aircraft turbine components, offering implications for future aerospace applications.

Keywords: Abradable Coatings, Polymeric composites, Erosion Resistance, Fillers, erosion, Tribology Pin-on-Flat Test, Aero Engine.

Acknowledgements

I would like to express my sincere gratitude to my supervisor, Dr. Farjad Shadmehri, for giving me the opportunity to join his team. His support and guidance have been instrumental in my growth, and I am truly grateful for the friendly and encouraging learning environment he created.

I would also like to extend my heartfelt thanks to Dr. Tahere Ebrahimi Sadrabadi, Farzad Kashefi, and Dr. Daniel Rosca for their collaboration throughout this project. This was a great opportunity for me to collaborate and learn from highly knowledgeable individuals in this field. I would like to give special thanks to Farzad for his invaluable guidance during the experiments.

Many thanks also go to Dr. Pantcho Stoyanov and his team, Kauê Bertuol, and Bruno Arendarchuck, for allowing me access to the tribology lab and its facilities, including the tribology machine and the rub-test machine. This research utilized a custom-built rub rig developed by doctoral researcher Mr. Kauê Bertuol under the supervision of Dr. Stoyanov. Their insights and willingness to share their expertise made a significant difference in this work.

Last but not least, I want to thank my family for their endless love, support, and continuous encouragement throughout my entire life.

Contents

List of Tables

List of Figures

Chapter 1

Literature Review

1. Literature Review

1.1 Introduction

In recent years, polymers and their composites have become increasingly popular as alternatives to traditional materials due to their easy processing, lightweight, affordability, and superior corrosion resistance.[1] In aerospace engineering, improving materials is crucial, particularly in aeroengine design where enhancing turbine efficiency and reducing power consumption are ongoing goals. In this matter a key strategy involves maintaining tight clearance between the stator and rotor blades in compressor sections to improve efficiency. These specialized sealing materials, known as abradables or clearance control materials, are crucial for protecting the engine. They not only ensure tight seals to prevent air escape but also protect the rotor blades from potential damage during operation. Additionally, these materials are designed to be abradable to minimize damage to the blades while also being resistant to erosion, a common challenge in operational environments.[2]

This thesis focuses on exploring polymer abradable coatings, essential for such aerospace applications. It specifically investigates the optimal coatings for jet engine fan core and Low-Pressure Compressor (LPC) stages (Figure 1), capable of withstanding temperatures below 100°C. The study compares two main groups of materials: thermosets and thermoplastics. To embark on this extensive investigation, a range of materials has been carefully selected based on the individual properties that lend themselves to creating effective coatings. The chosen materials include thermosets, which are set permanently when heated, thermoplastics, which can be softened and reshaped, and various pre-made products known for their reliability. We have also included commercially used materials to provide a baseline for our comparisons. This allows us to understand how the new coatings stack up against the known performance of existing polymeric abradable materials.

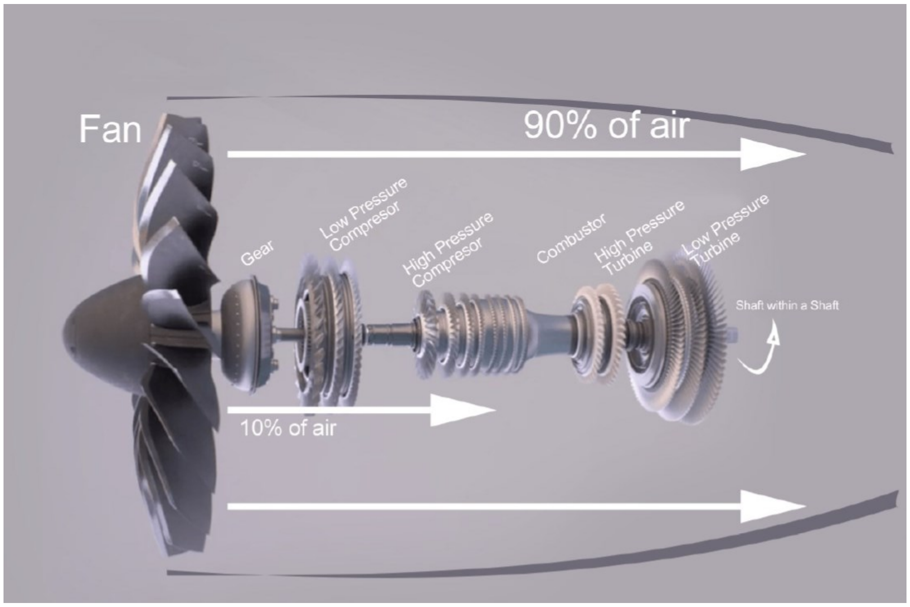

Figure 1. A simplified cutaway of a jet engine core and fan [3]

The methodology for exploring the abradability of these coatings is by performing pin-on-flat test and a rub rig test. For erosion resistance, we evaluate how the materials behave using ASTM G76 erosion tests. We look at how the different types of polymers behave and how well they stand to being worn down.

The research includes a comparison against two abradable commercially available materials that are epoxy based with hollow glass microspheres. This benchmarking helps us determine the effectiveness of our coatings.

The upcoming sections will detail the methodology, materials, the testing processes, the results that were obtained, and the insights we've gained. The thesis ends by identifying the best polymer options and proposing their possible uses in aerospace engineering. By documenting our research process and findings, this thesis contributes to the ongoing innovation in aerospace materials, particularly focusing on the enhancement of engine performance with advanced polymer abradable coatings.

1.2 Solid Particle Erosion

Solid particle erosion (SPE) is a process where materials lose mass due to the repeated impact of particles that are energized in a carrier fluid. The erosion rate is defined as the ratio of mass loss to the mass of the impacting particles, and erosion resistance is its reciprocal.[4] Research indicates that the erosion behavior of materials in SPE tests is affected by over twenty different parameters, which interact in complex ways[4], [5], [6]. These parameters are broadly categorized into three groups: erosion conditions, substrate characteristics, and erosion mechanisms.

The SPE behavior of materials is profoundly influenced by various erosion conditions, which include the physical and chemical characteristics of erodent particles such as size, shape, hardness, and mass. For instance, erosion rates are generally considered constant above a critical particle size range of 100-200 micrometers. The shape of the particles also plays a crucial role in how they interact with surface materials, while the hardness of the particles tends to have a lesser impact on the erosion rate. Moreover, the mass of the particles significantly affects the overall impact of erosion.

Impact angles also play a critical role in the erosion process. Normal impacts occur at 90°, where the particle strikes the surface perpendicularly, leading to one type of wear pattern, while oblique impacts (angles less than 90°) promote different wear processes such as abrasion, significantly influencing how particles interact with the surface.

Additionally, the velocity at which particles strike a surface and the mass of material impacting a unit area over time are crucial in determining the intensity of erosion. These factors together contribute to a complex and varied erosion landscape, where each variable can significantly influence the outcome of SPE tests. This intricate interplay of conditions highlights the need for an understanding of erosion to develop materials that can withstand such challenging conditions effectively[4].

The substrate characteristics significantly affect how materials respond to erosion under different impact conditions. In the case of ductile erosion, there is an initial period where the surface of the material may increase in weight because particles become embedded within it. Once these particles are removed, the erosion rate becomes steady, particularly during normal impacts where particles strike the surface perpendicularly. Ductile erosion typically results in the greatest material loss at low impingement angles.

Conversely, brittle erosion occurs predominantly at high impingement angles and involves more abrupt material removal processes, such as cracking or chipping. This type of erosion is associated with more aggressive impacts that cause material to break away sharply.

These distinctions highlight the importance of the material properties of the substrate in influencing the erosion dynamics, impacting both the erosion rate and the pattern of material loss. Figure 2 presents these erosion behaviors.

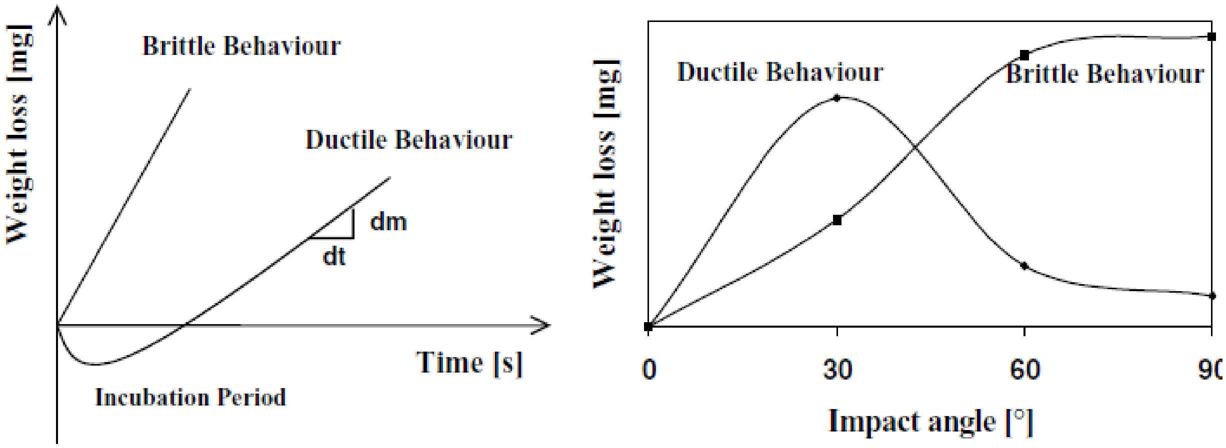

Figure 2. Erosion behavior of ductile and brittle materials [4].

Ductile polymers, like elastomers, often show high erosion rates when impacted at oblique angles. They generally lose less material over time compared to more brittle polymers, such as certain ductile thermoplastics, which can crack and break apart under similar conditions. Polyurethanes with hard segments display enhanced erosion resistance due to their crystalline structure. These hard segments form tightly packed, ordered regions within the polymer chain, which provide increased mechanical strength and resistance to wear, thus helping to minimize erosion.[7]. This phenomenon can be attributed to the inherent mechanical properties of elastomers, which allow them to absorb energy more effectively during particle impact, thereby minimizing material loss[8]

Epoxy resins are an example of brittle polymers, which typically exhibit characteristics of brittle erosion, leading to sharp and sudden material loss upon impact [7].

In materials like crosslinked polyethylene and some thermosets such as epoxy/polyurethane blends, a higher crosslink density usually leads to reduced erosion resistance. The properties of the eroded surface often differ from the bulk material due to thermal, mechanical, and chemical degradation. The friction coefficient and hardness can vary significantly during erosion, heavily influenced by the impact angle.

Figure 3 shows the mechanisms of material removal during erosion which vary widely and depend on the type of material involved. Rubbers often undergo tearing and fatigue due to their flexible nature. Ductile metals and polymers, which can deform plastically under stress, are typically susceptible to cutting and chip formation. On the other hand, more rigid materials like ceramics, glasses, and brittle polymers are prone to crack formation and brittle fracture because of their inherent fragility. At the point of impact, the concentration of energy is crucial in determining the nature of erosive wear and is greatly influenced by the material's ductility. Friction also plays a significant role in erosion; particles do not simply strike the surface but may also shift and rotate within the contact area, further contributing to wear. [4]

Employing highly elastic materials helps absorb and dissipate the kinetic energy of impacting particles, thus minimizing the erosive effect. Moreover, the strategic incorporation of fillers, varying in nature, shape, and proportion, can finely adjust the erosion behavior of polymers, optimizing their performance under erosive conditions [9].

Generally, solid particle erosion has several mechanisms that depend on impact conditions and material properties. Figure 3 is illustrates these mechanisms. At low impact angles (Mechanism a), particles strike the surface obliquely, leading to abrasion through micro-cutting and micro-ploughing actions. Micro-cutting involves the removal of tiny material fragments as particles cut into the surface, while micro-ploughing displaces material to the sides without immediately removing it. Sharp, hard particles slide across ductile materials, removing material by cutting grooves or ploughing through the surface. This results in higher erosion rates at low impact angles.

At high impact angles and low particle velocities (Mechanism b), surface fatigue becomes the dominant mechanism. Repeated impacts cause minor elastic deformations without immediate material removal. Over time, these cyclic stresses lead to the initiation and growth of micro-cracks. In materials exhibiting ductile erosion behavior, these micro-cracks merge, resulting in material loss due to fatigue failure after numerous impacts.

When particles impact at medium speeds and large impact angles (Mechanism c), brittle fracture or multiple plastic deformation occurs. In materials that show brittle erosion behavior, the impact energy exceeds the fracture strength, causing cracks to initiate and propagate rapidly, leading to chipping. Ductile materials may undergo significant plastic deformation, and repeated impacts can cause hardening, increasing brittleness and leading to eventual fracture and material removal.

At high impact speeds (Mechanism d), the kinetic energy of particles is so high that upon impact, it converts into heat due to internal friction, leading to localized surface melting. Materials with low melting points or low thermal conductivity are particularly susceptible to this mechanism. The melting weakens the surface, making it more prone to erosion as the molten material can be easily displaced by subsequent impacts.

Finally, macroscopic erosion with secondary effects (Mechanism e) involves large-scale damage due to secondary phenomena such as thermal shock, oxidation, or other chemical reactions induced by the erosive environment. High particle flux rates and environmental conditions can contribute to this mechanism, leading to significant degradation beyond mechanical erosion, including extensive surface damage, structural failures, or accelerated chemical wear [4]

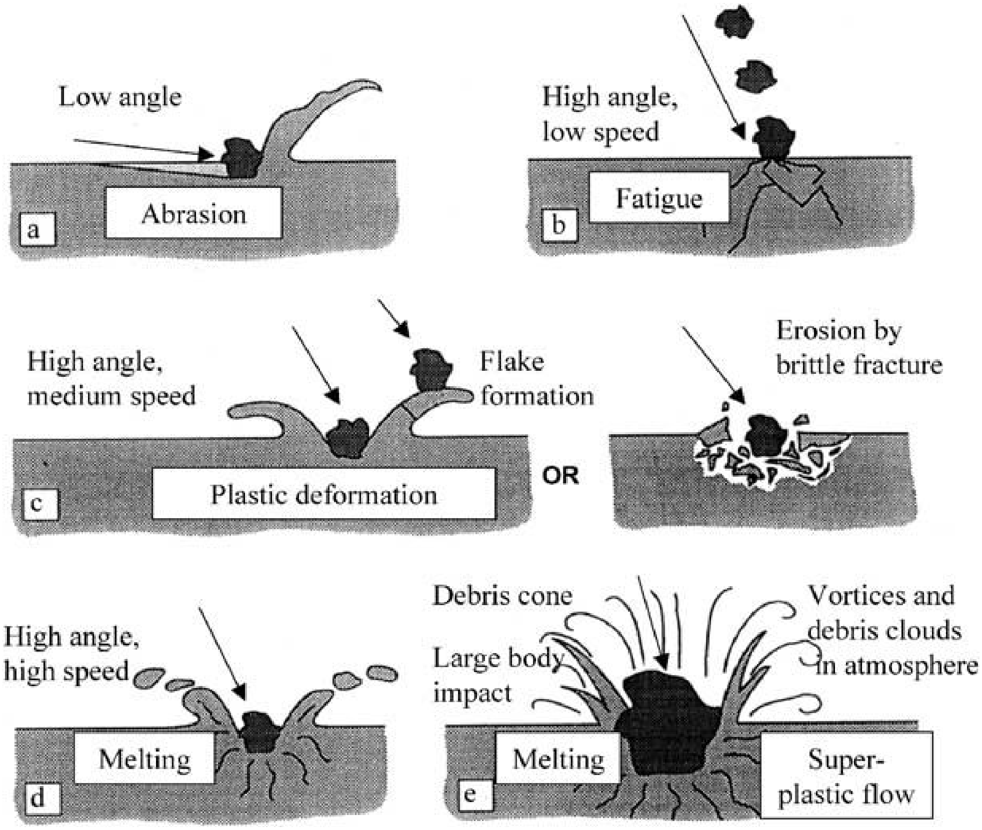

Figure 3. Possible mechanisms of solid particle erosion; (a) abrasion at low impact angles, (b) surface fatigue during low speed, high impingement angel, (c) brittle fracture or multiple plastic deformations during medium speed, large impingement angle, (d) surface melting at high impact speeds, (e) macroscopic erosion with secondary effects [4]

1.3 Erosion of Thermosets and Their Composites

The study conducted by Trezona et al.[10] investigated the impact of curing conditions on clear coat materials and found a slight negative correlation, indicating that while curing conditions do influence erosion resistance, their impact isn't definitive. Similarly, Duan [6] reported that epoxy and polyurethane paints used in hydraulic machinery show lower erosion resistance than rubber coatings, suggesting that the choice of coating significantly affects machinery durability in erosive environments. Further, Zaib.[11] studied the effect of fibers on erosion resistance and observed that fibers might decrease resistance, also providing a detailed comparison of erosion rates across various types of polymers. Observations by Zaib [11] highlight that replacing carbon fibers with aligned carbon nanotube (CNT) films in reinforcement materials can shift wear behavior from brittle to ductile. CNTs can absorb more energy during fracture or bending, and their erosive wear properties can be enhanced with additional functionalization. Conversely, composite materials that use glass fibers as fillers typically exhibit higher erosive wear than those reinforced with carbon fibers. This difference is often due to variations in fiber/matrix bonding and the inherent properties of the fibers.

Additionally, nano-silica is recognized as a cost-effective nanoparticle commonly used in the fabrication of composites aimed at improving erosion endurance. Thanks to its self-lubricating properties, nano-silica bonds effectively with the matrix, thus enhancing the composite's overall resistance to erosive wear [12].

Barkoula [13] discovered that incorporating hydrothermally decomposed polyester-urethane (HD-PUR) into epoxy resin (EP) enhances the material's fracture energy (Gc) and significantly boosts its resistance to solid particle erosion. This improvement in properties is depicted in Figure 4. The addition of HD-PUR to the epoxy resin contributes to a tougher composite that is better equipped to withstand the impacts and stresses involved in erosive environments, demonstrating the potential of material modifications for enhancing durability and performance in challenging conditions.

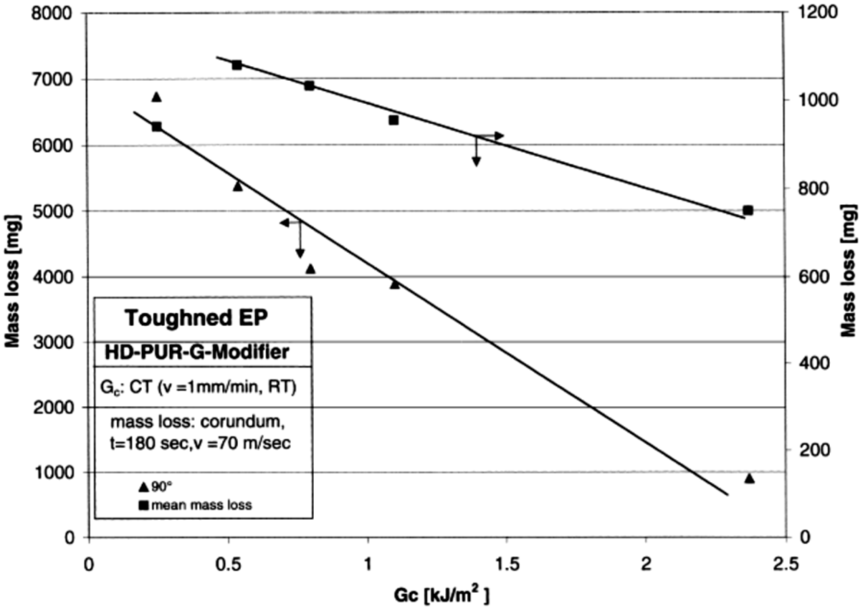

Figure 4. Variation of mass loss as function of Gc for the EP/HD-PUR-G compositions[13].

Fernández-Álvarez [14] found that incorporating silica nanoparticles into epoxy resins resulted in improved erosion resistance, as illustrated in Figure 5.

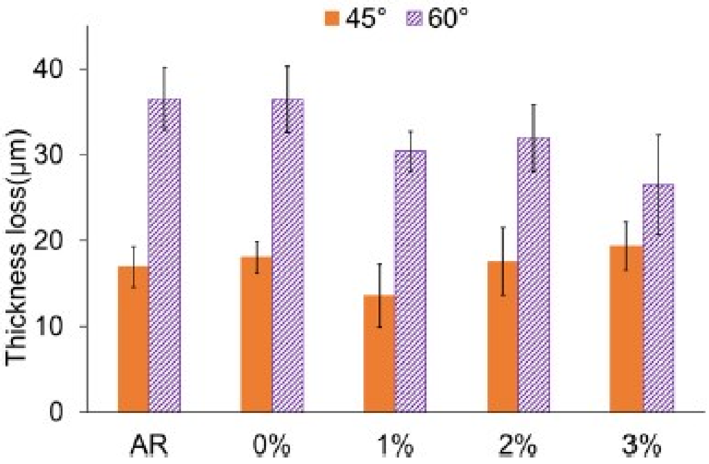

Figure 5. Thickness loss vs. NP load at different angles[14].

Song [15] conducted a comparative analysis on the erosion rate and maximum particle load among three different types of coatings: PU-R (Polyurethane), SPU1-3% (a novel slippery polyurethane with 1% to 3% wt% of surface-modifying polymers), and SPU2-3%, as presented in Figure 6. The study used blue bars to show the erosion rate, measured in micrograms per gram (µg/g), and orange bars to indicate the maximum particle load, in grams per square centimeter (g/cm²). The findings showed that PU-R had a lower erosion rate at 117 µg/g and a higher maximum particle load at 73 g/cm², suggesting better durability against particle impact. In contrast, SPU1-3% exhibited a higher erosion rate at 131 µg/g and a slightly lower maximum particle load at 66 g/cm². SPU2-3% displayed the highest erosion rate at 140 µg/g but maintained the same maximum particle load as PU-R. This data implies that while the modifications in SPU1-3% and SPU2-3% might improve some properties, they also result in increased erosion under the tested conditions.

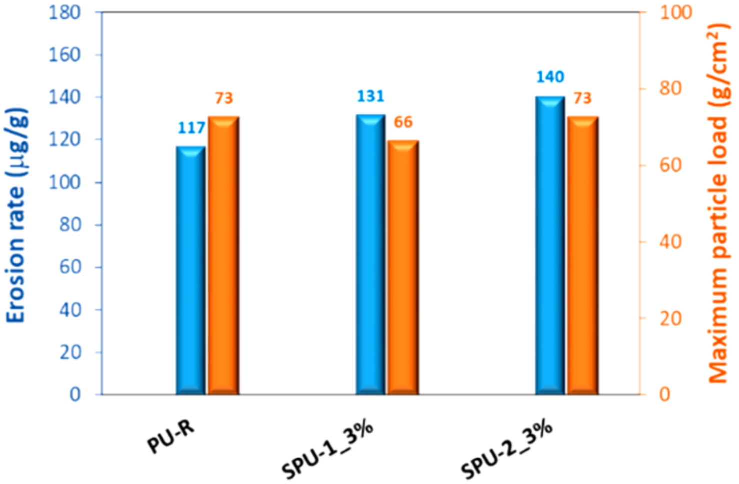

Figure 6. Sand erosion resistance of PU-R (erosion-resistant polyurethane) and SPU (slippery polyurethane) coatings. Test conditions: 50um angular alumina particles, impact velocity of 150 m/s, impact angle of 30 deg[15].

Ozen [16] discovered that polyurethane (PU) tape surfaces exhibited significantly better erosion resistance compared to surfaces made from carbon fiber/epoxy (CF/EP) and glass-fiber/epoxy (GF/EP) composites as depicted in Figure 7. As shown, PU tape maintains a consistently low erosion rate across all impact angles. This finding highlights the superior performance of PU tape in withstanding erosive forces.

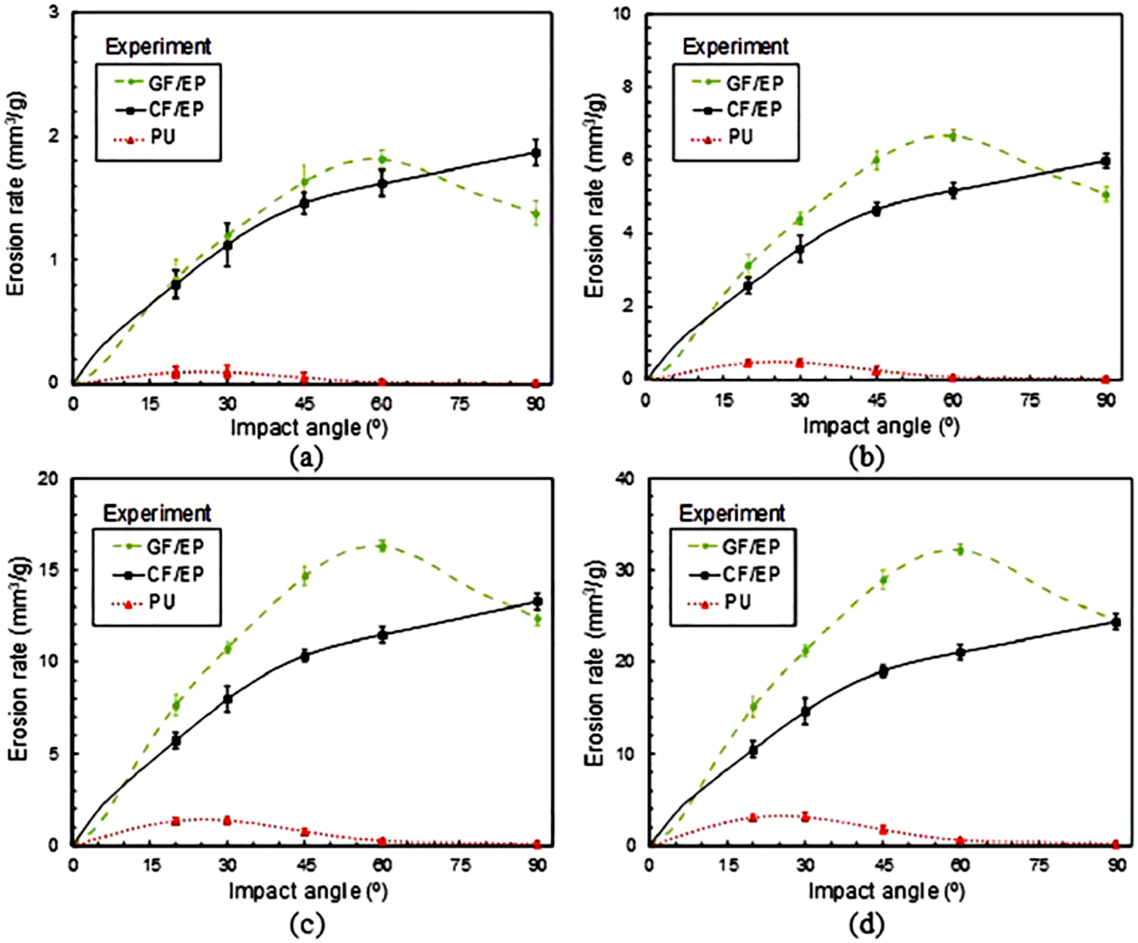

Figure 7. Variations of the erosion rates vs. the impact angle of the PU tape, CF/EP and GF/EP composite materials; a-70 m/s, b -110m/s, c- 150m/s, d-190m/s[16].

Kulkarni [17] found that adding 2% carbon black to glass-epoxy composites reduced erosion rates by 15 to 30%. Additional reductions of 10 to 30% in erosion rates can be achieved by incorporating rubber fillers. Shahapurkar [18] observed that crumb rubber can increase the erosion resistance of neat epoxy. Figure 8 shows the erosion rates of epoxy composites with varying concentrations of crump rubber particles (10%, 20%, and 30%) and neat epoxy, under different velocities of impinging particles (30, 45, 60 m/s). Composites with higher rubber content (EC-20 and EC-30) demonstrate lower erosion rates than those with lower rubber content (EC-10) and neat epoxy, indicating that the inclusion of crump rubber enhances the material's resistance to erosion.

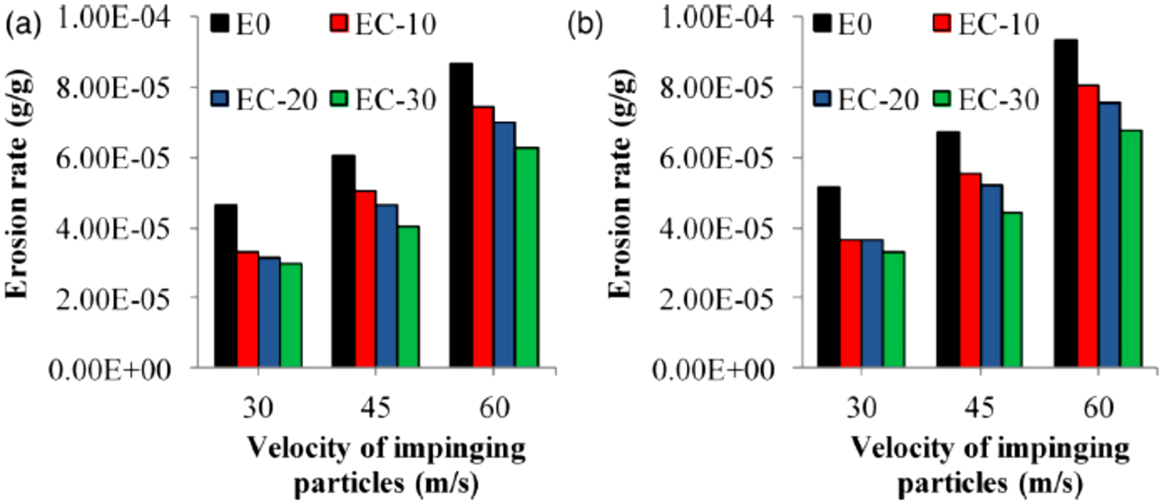

Figure 8. Erosion rate vs particle velocity at 45° (a) and 60° (b) angles[18].

Limin [19] found that adding carbon nanotubes to polyester resin increased flexural strength and erosion resistance (Figure 9).

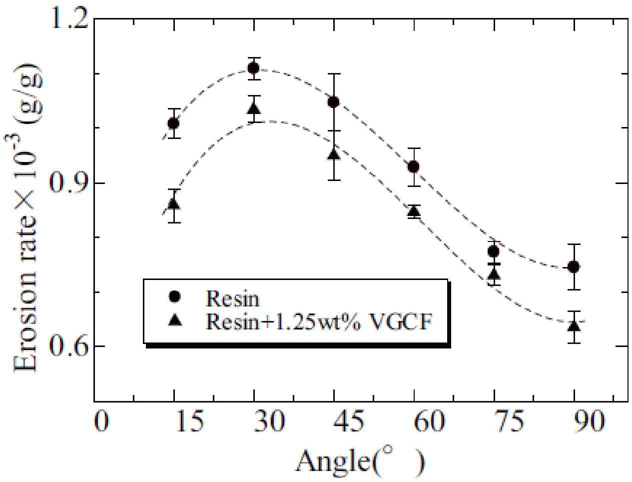

Figure 9. Erosion rates vs. impact angles at 128m/s[19].

1.3.1 Effect of Filler, Hollow Glass Microspheres (HGM) in Polymeric Matrix

Based on research by Pinisetty et al. [20], Hollow Glass Microspheres (HGM) serve multiple roles and demonstrate varied properties when incorporated into different materials. As functional fillers in plastics, HGM enhance properties like stiffness and heat distortion resistance while reducing costs. They are characterized by their low density and the ability to lower the Coefficient of Thermal Expansion (CTE) of composites, which minimizes noise, vibration, and harshness. Additionally, their low thermal conductivity and electric properties, such as a low dielectric constant and loss tangent, are beneficial.

In thermoplastics, HGM contributes to productivity benefits by enabling faster cooling rates from the melt and improves dimensional stability, reducing sink and warpage. They also support increased stiffness and reduce both thermal conductivity and dielectric constant, maintaining good survival rates during extrusion processes, with breakage under 5 vol% even at high melt viscosity.

When used in thermoset epoxy syntactic foams, HGM improves compressive properties, provides thermal insulation, and enhances dimensional stability. Furthermore, when blended into a rubber matrix like Nitrile Butadiene Rubber (NBR), HGM can significantly reduce the friction coefficient and boost anti-wear properties, enhancing the material's overall performance in demanding applications.

1.3.2 Effect of Filler, Carbon Nanotube (CNT) in Polymeric Matrix

Lau, Kin-Tak, et al. [21], 2003, investigated the properties of multiwalled carbon nanotubes (CNTs) combined with epoxy resin. They dispersed the CNTs into the resin using sonication and then measured the Vickers hardness with a micro-hardness tester. Their findings showed that samples with less than 2% weight of CNTs exhibited a reduction in hardness compared to bare resin. However, samples with 2% weight of CNTs showed an increase in hardness by about 20% as depicted in Figure 10.

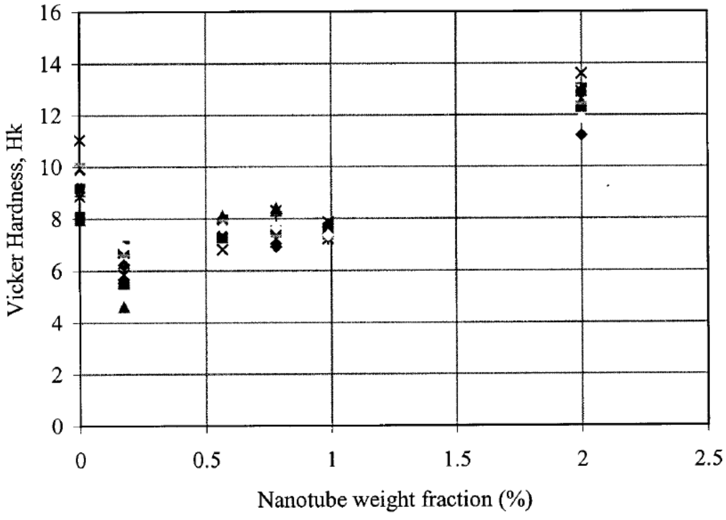

Figure 10. hardness vs CNT w%[21].

Biercuk, M. J., et al. (2002) [22] incorporated single-walled carbon nanotubes (SWCNT) into Epon 862 epoxy resin. They achieved dispersion of the carbon materials by ultrasonically treating them in an organic solvent (either dichloroethane or N–N dimethylformamide) for up to 48 hours to create a stable suspension. This method allowed the epoxy resin to dissolve into the carbon-solvent mixture, forming a smooth emulsion indicative of high-quality dispersal. Their findings highlighted a significant increase in hardness, which tripled at a concentration of 2wt%.

Kuzumaki, Toru, et al.[23] (2000) explored the use of carbon nanotubes (CNT) in titanium to develop metallic nanocomposites. They noted a substantial increase in hardness when CNTs were added to pure titanium. This research also included the examination of other fillers, as detailed in Figure 11. The results from both studies underscore the potential of CNTs to enhance the mechanical properties of various composite materials.

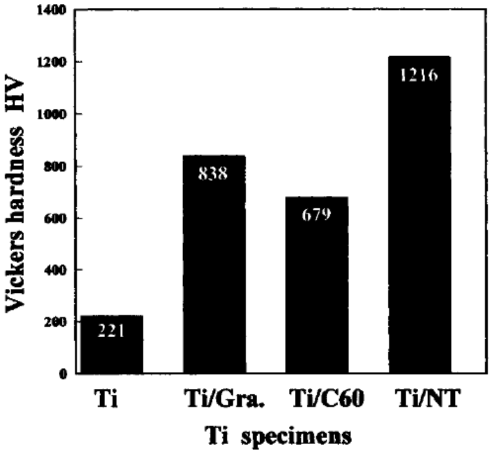

Figure 11. Vickers' hardness for pure Ti, Ti/graphite, Ti/C60, and Ti/NT[23].

1.3.3 Silicone Rubbers

Silicone rubbers are highly resistant to solvents and oils, even at elevated temperatures. They effectively maintain their integrity when in contact with polar organic compounds and can revert to their original state following exposure to non-polar organic substances. However, they are susceptible to degradation by strong acids.[24].

Moreover, the innovation in silicone rubbers includes the development of the first autonomic self-healing elastomer in 2007, which can almost completely regain its initial tear strength, demonstrating enhanced fatigue capabilities [25], [26].

Particularly relevant to aerospace applications, Haijun AUAN et al. [27] have studied the abrasion behavior of abradable silicone rubber against a Ti-6Al-4V blade. This study utilized vulcanized silicone rubber tested at various blade speeds and constant incursion rates, showcasing its potential in high-wear aerospace environments where maintaining tight clearances and ensuring minimal debris are crucial.

The testing of silicone abradable materials against a titanium blade demonstrated that the softer silicone does not wear or damage the harder titanium blade tip. However, the abrasion pattern on the silicone abradable increased as the blade velocity was raised, indicating that while the silicone protects the blade from damage, it experiences greater wear under higher speeds.

During the wear testing between the blade and the silicone abradable, an interesting phenomenon of debris generation was observed. As the sharp blade tip makes contact with the silicone rubber, it concentrates stress on the surface, slicing through the rubber and producing debris. At lower blade velocities, this debris is generally uniform, typically smaller than 0.5mm in size. However, as blade velocity increases, the debris particles become larger and more irregular in shape. For example, at a blade velocity of 225m/s, the debris sizes range from 1-2mm. Further increases in blade velocity result in even larger debris sizes, reaching 3-5mm, illustrating a clear correlation between blade speed and the size and uniformity of debris produced. The study reveals that silicone rubbers, while useful in some abradable applications, exhibit poor wear behavior characterized by significant debris generation at varying blade speeds.

Kumar, Vineet, et al. [28] (2021) published a review paper on the effect of different nanofillers on silicone rubber properties. They reviewed a paper, published by Sarath, P. S., et al. [33] on tribological properties of exfoliated graphite (EG) filled silicone rubber (SR). They observed that both coefficients of friction (COF) and specific wear rate are decreased by adding different content of EG. The trend of their observation is presented in Figure 12. The effect of different filler content for different experimental specifications (load and velocity) is illustrated in Figure 13. Based on these graphs there is an optimum concentration of EG that minimizes the wear in silicone rubbers. COF, Specific wear rate are defined as follows:

$$COF = \frac{F_f}{F_n}$$

$$Specific\ Wear\ rate = \frac{\Delta m}{\rho\ F_n L}$$

Where F_f (frictionalforce), F_n (normalload which is applied), Δm is the weight loss, ρ is the composites' density, F_n is the applied load and L is the sliding distance (meters).

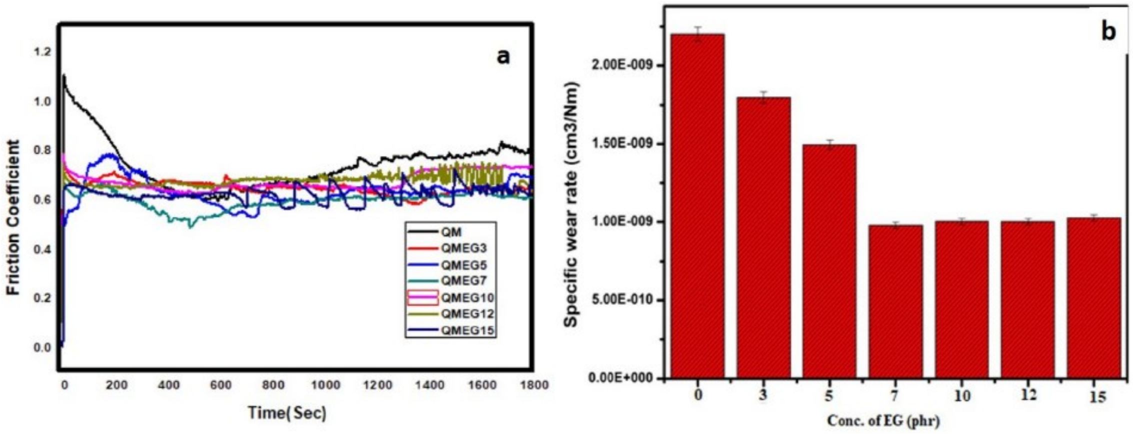

Figure 12. (a) Friction coefficient of composites as a function of time (b) specific wear rate of the composites with various contents of EG (load-30 N, speed-2 m/s)[29].

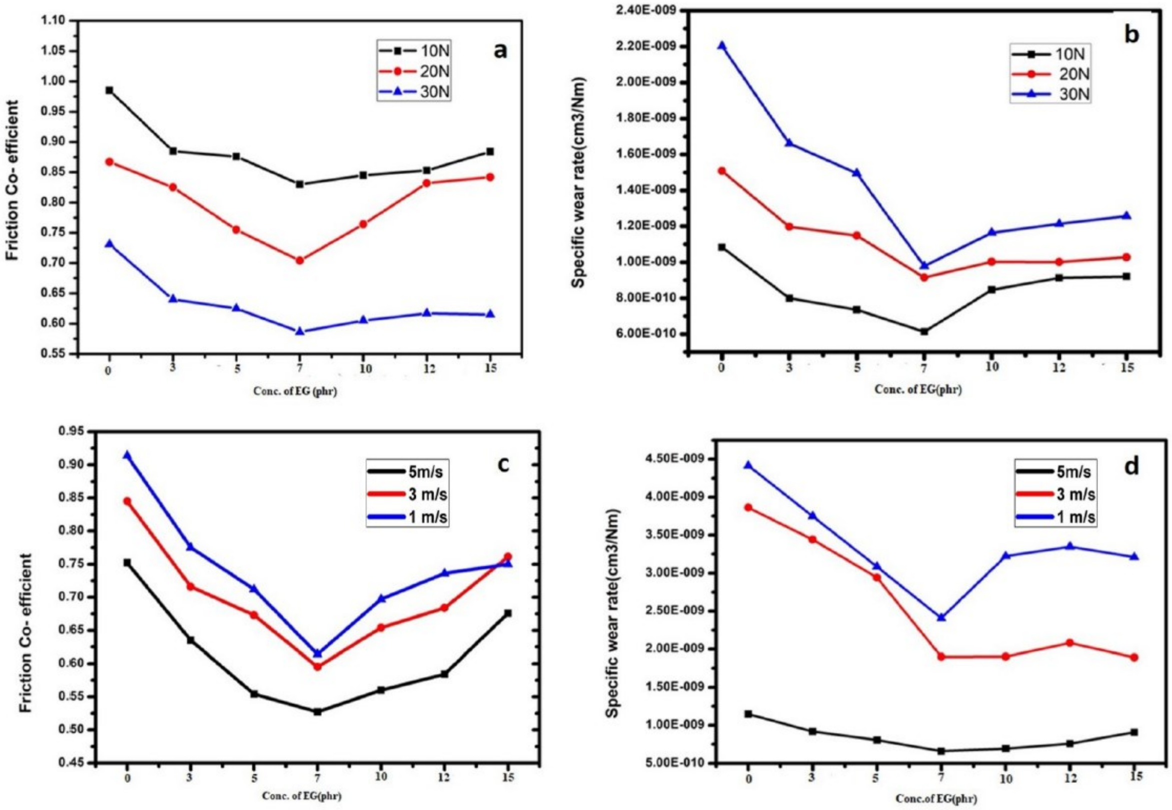

Figure 13. (a) **Friction coefficient** (b) **specific wear rate of composites with different loads (1800 m, RT,2 m/s) and** (c) **Friction coefficient** (d) **specific wear rate of the composites with different sliding velocity (30 N, RT, 1800 mm)**[30].

1.4 Erosion of Thermoplastic Polymers and Their Composites

Harsha et al. [31] conducted a comprehensive study on the erosion properties of various polyaryletherketones (PAEKs), including polyetheretherketone (PEEK), polyetherketone (PEK), and polyetherketoneketone (PEKK). Their research also explored the effects of reinforcing these polymers with short fibers and incorporating fillers such as carbon fiber, glass fiber, polytetrafluoroethylene (PTFE), and graphite. The aim was to assess how these fillers influence the erosion resistance of the PAEKs. The results and comparisons of the different samples studied are detailed in Table 1, highlighting the variations in erosion resistance based on the type of filler and fiber reinforcement used.

Table 1. Various polyaryletherketones (PAEKs) samples [31]

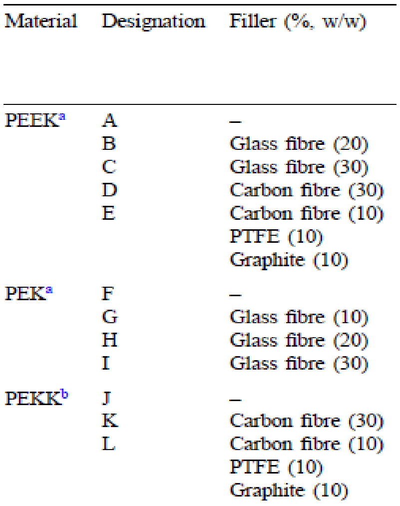

Material	Designation	Filler (%, w/w)
PEEK[a]	A	–
	B	Glass fibre (20)
	C	Glass fibre (30)
	D	Carbon fibre (30)
	E	Carbon fibre (10) PTFE (10) Graphite (10)
PEK[a]	F	–
	G	Glass fibre (10)
	H	Glass fibre (20)
	I	Glass fibre (30)
PEKK[b]	J	–
	K	Carbon fibre (30)
	L	Carbon fibre (10) PTFE (10) Graphite (10)

In the research presented in Figure 14, Harsha et al. [31] measured the erosion rate (ER) for various polyaryletherketones (PAEKs) including PEEK, PEK, and PEKK, under different velocities and impingement angles. The results indicated that for PEEK, the maximum erosion rate occurs at an impingement angle of 30 degrees. In contrast, for the other two types of PAEKs studied, the maximum erosion rate is observed at 60 degrees. Generally, the trend across all materials shows that the highest erosion rates are most frequently observed at an impingement angle of 60 degrees.

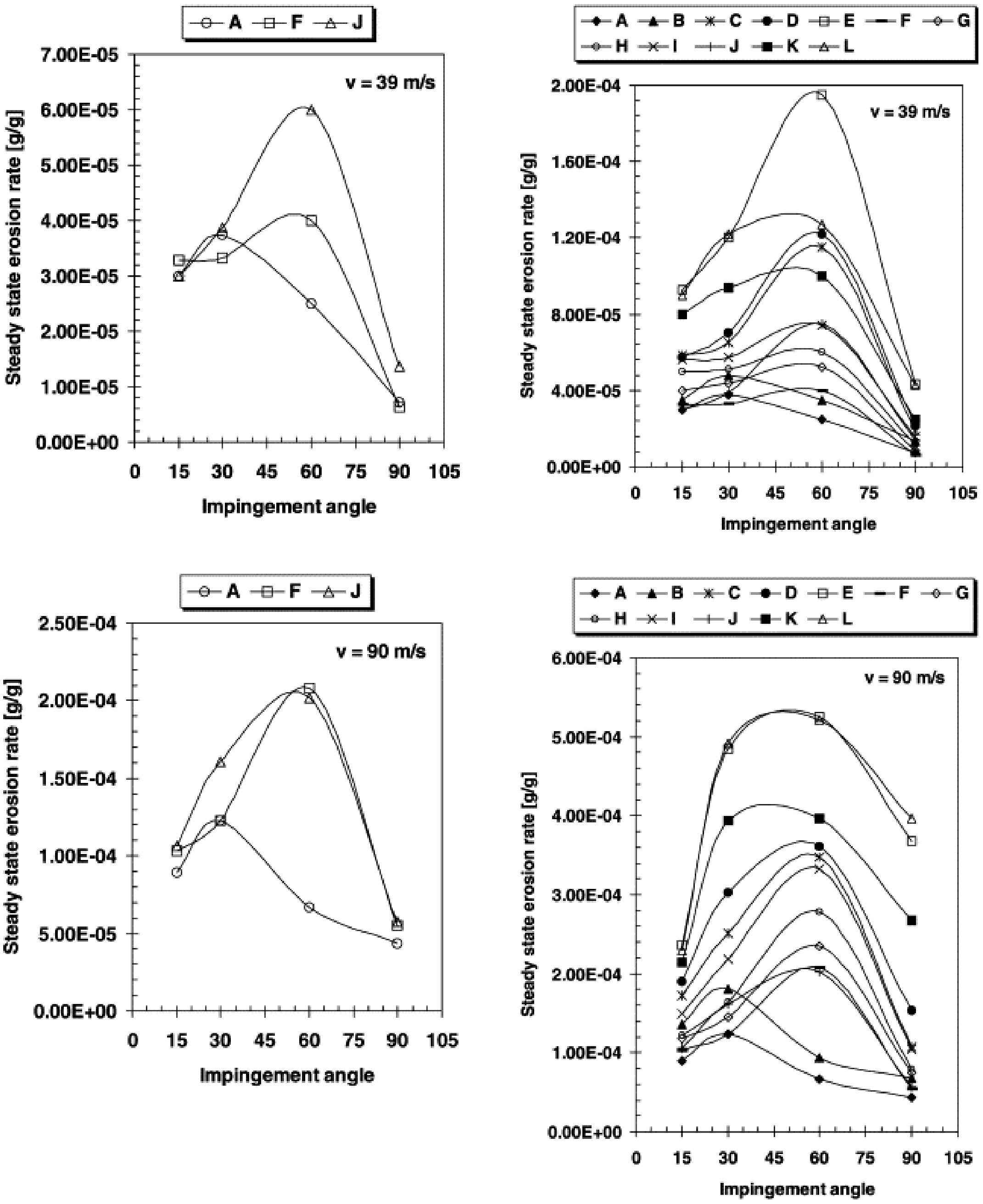

Figure 14. Influence of impingement angle on erosion rates of PAEKs and their composites[31].

Numerous studies have been dedicated to exploring the relationships between mechanical properties and erosion rates. Harsha et al. specifically investigated how mechanical properties such as hardness, tensile strength, modulus of elasticity, fracture toughness, yield stress, yield strain, rebound resilience, ultimate strength, and elongation impact the steady-state erosion rate. This study focused on various impingement angles and found significant correlations at specific angles. For instance, at 30° and 90° impingement angles with an impact velocity of 90 m/s, as depicted in Figure 15, the research demonstrated that ultimate tensile strength, ultimate elongation to break, and hardness are closely linked to erosion rates. The detailed results in panels (a), (c), and (e) illustrate erosion rates at a 30° angle under various conditions, whereas panels (b), (d), and (f) represent rates at 90°. Each panel correlates erosion rates with different mechanical treatments and conditions, highlighted by specific symbols like [Se]¹ and [He]¹, and points labeled from A to L representing various experimental setups as listed in Table 3.

The findings indicated a strong correlation between the steady-state erosion rate and the aforementioned mechanical properties at a 30° impingement angle. At a 90° angle, however, the correlation was primarily noted with ultimate tensile strength and hardness. No significant correlations were noted at 15° and 60° angles. Ultimately, this extensive analysis confirmed that certain mechanical properties, particularly ultimate tensile strength, ultimate elongation, and hardness, substantially influence the erosion rate of the composites tested. Additionally, the study highlighted that neat polyaryletherketones (PAEKs) exhibited superior erosion resistance, likely due to their high ultimate tensile strength.

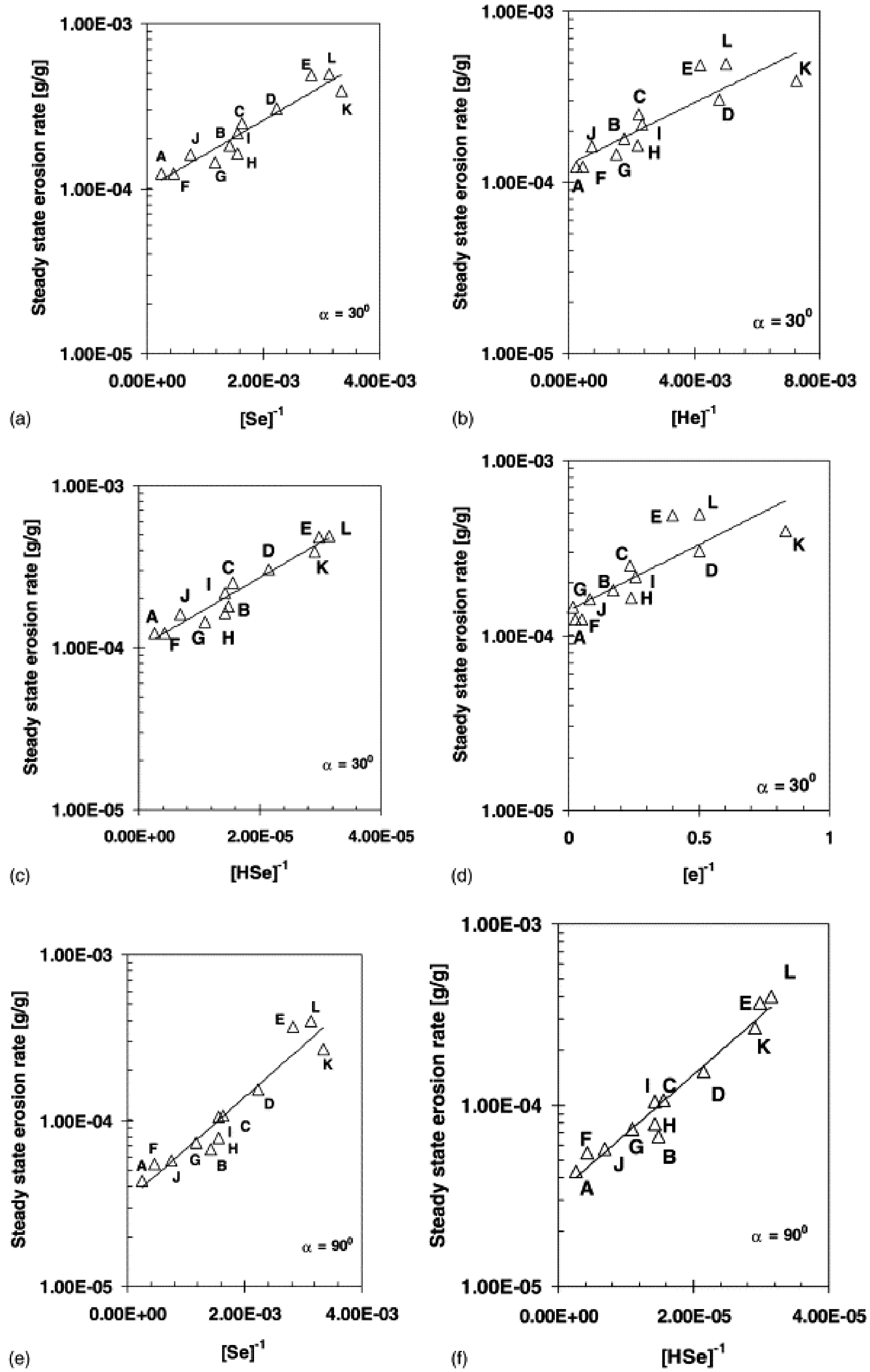

Figure 15. Steady-state erosion rate at different impingement angles as a function of various mechanical properties for PAEKs and their composites at impact velocity of 90 m/s. Where *S* is the ultimate tensile strength, *e* the ultimate elongation at break and *H* the hardness (M scale)[31].

Tamer Sınmazçelik et al.[33] conducted a study on polyphenylene sulfide (PPS) composites, enhancing them with short glass fibers and calcium carbonate (CaCO3) mineral particulates. They performed erosion tests on these composites across a range of erodent velocities and angles to assess their durability and resistance. The outcomes of these tests are comprehensively summarized in Figure 16, providing insights into how the added materials influence the erosion resistance of PPS under various conditions.

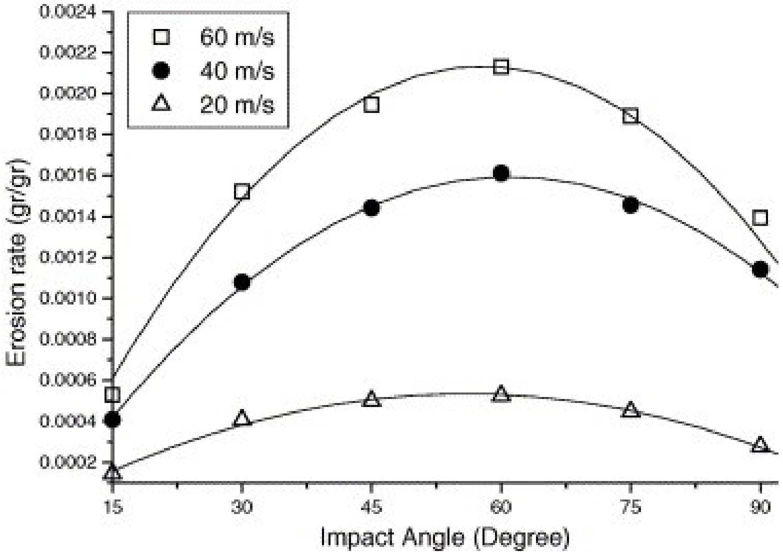

Figure 16. Normalized erosion rate as a function of impingement angles for different particle speeds [33]**.**

M. Dong et al. [34] investigated the impact of incorporating carbon nanotubes (CNTs) into thermoplastic polyurethane on its erosion rate (ER). Their study, detailed in Figure 17, found that as the concentration of CNTs in the polyurethane increases, the erosion rate improves. This suggests that the dispersion of CNTs within the polymer matrix enhances its resistance to erosive wear, highlighting the beneficial effects of nanomaterial reinforcements in thermoplastic composites. M. Dong et al. [34] also explored how particle size and impinging angle affect the erosion rate (ER) of thermoplastic polyurethane reinforced with carbon nanotubes (CNTs). Their findings demonstrate that both the size of the particles and the angle at which they strike the surface significantly influence the erosion rate.

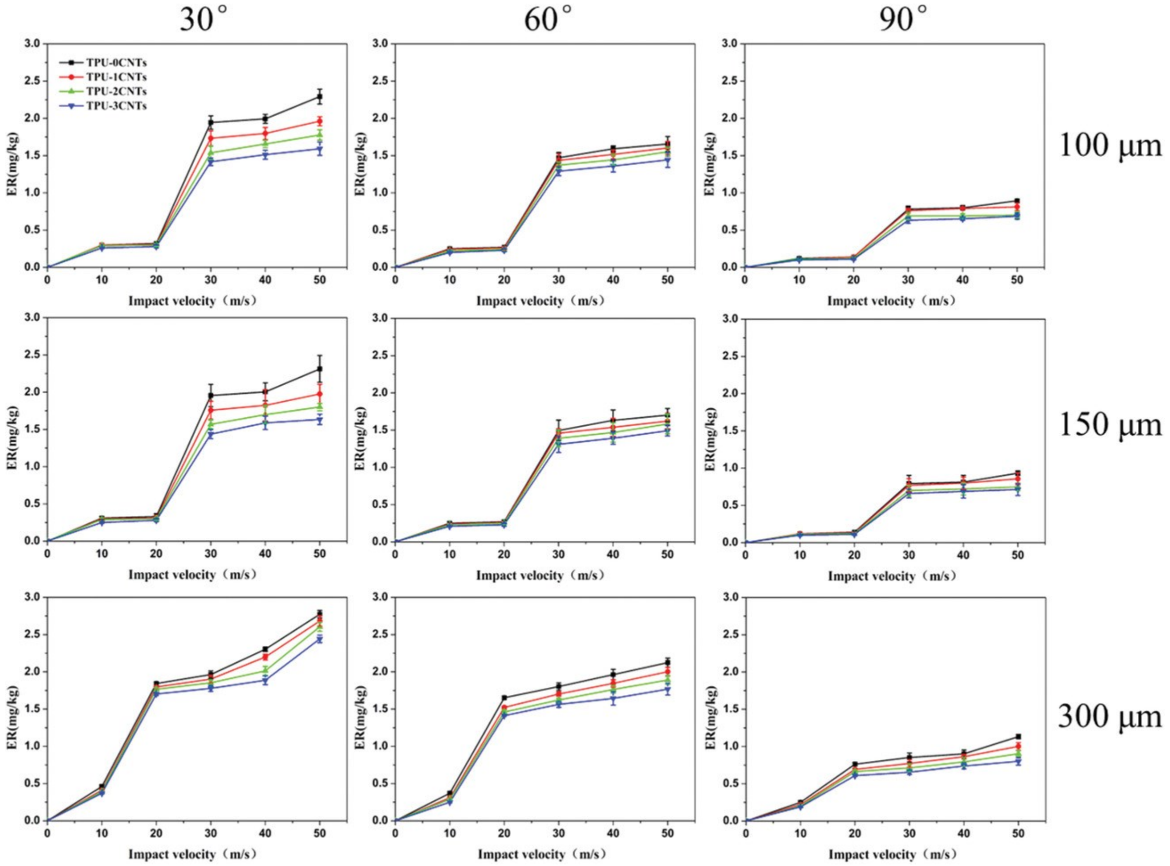

Figure 17. Erosion rate (ER) of CNTs/TPU nanocomposites as a function of impact velocity at 30°, 60°, and 90° impact angles with erodent sizes of 100, 150, and 300 µm[34].

S. Arjula et al. [35] conducted an extensive study on the erosion behavior of various high-performance thermoplastic polymers, including PEI, PEEK, PEK, PPS, PES, PSU, and UHMWPE. Their findings, summarized in Figure 18, revealed that these polymers experienced the highest erosion rates at an impact angle of 30 degrees and the lowest at 90 degrees, indicating ductile behavior. The study showed that erosion rates varied with the impact angle and velocity. Notably, PEEK demonstrated superior erosion resistance at oblique impact angles, while PPS was more resistant at higher impact angles due to the softening of the matrix and the embedment of erodent particles.

The research also highlighted the significant role of mechanical properties such as hardness, fracture toughness, tensile strength, and ultimate elongation in influencing the erosive wear of these polymers. The glass transition temperature was another critical factor affecting erosion resistance. The predominant wear mechanisms changed with the impact angle: oblique impacts mainly led to micro cutting, microchipping, micro ploughing, ductile tearing, and plastic deformation, whereas material removal at normal impacts occurred primarily through microcracking and plastic deformation. This detailed analysis provides insights into how material properties and testing conditions influence the erosion resistance of advanced thermoplastic materials.

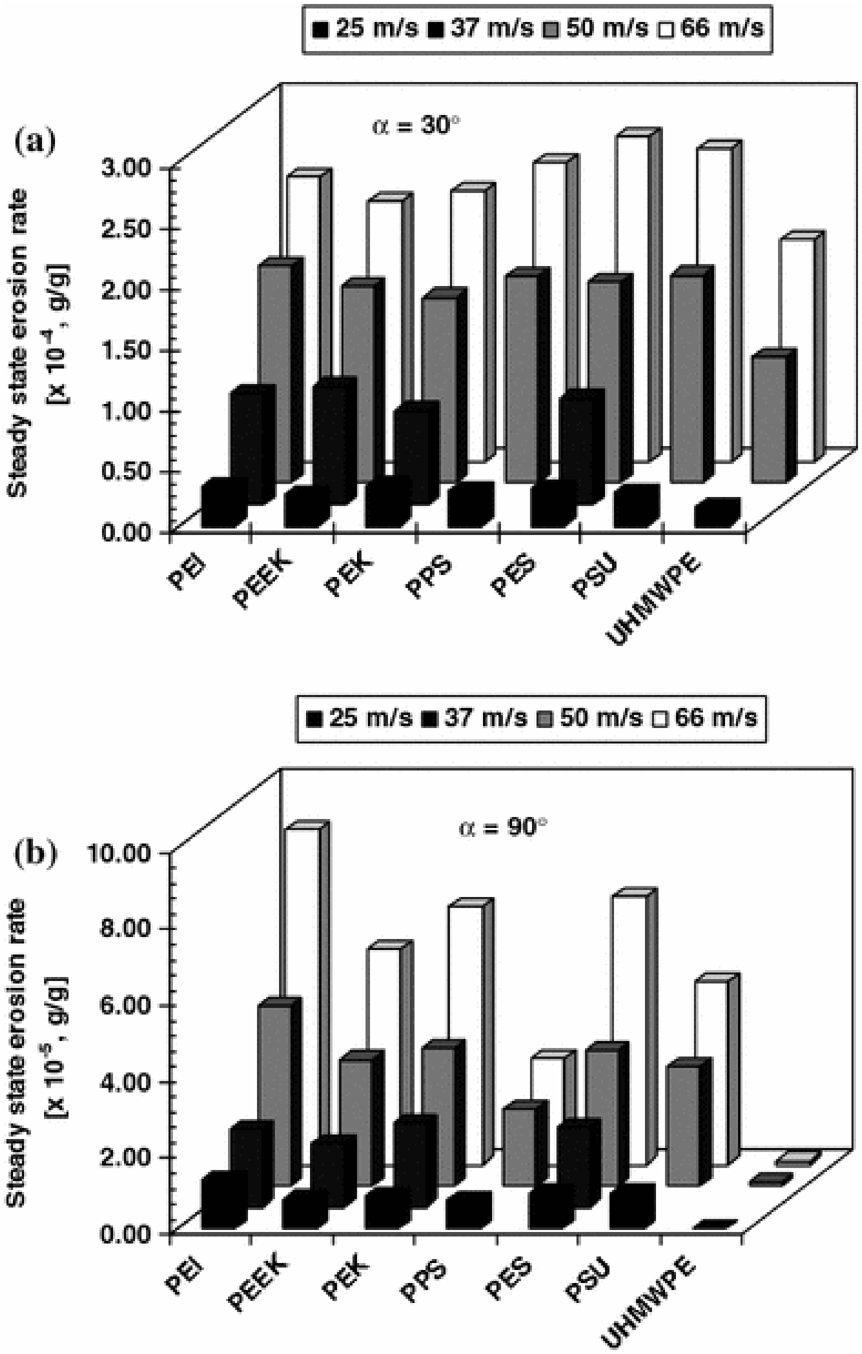

Figure 18. Histograms showing the steady-state erosion rate of various polymers at different impact velocities[35]

M. Dong et al. [36] conducted a comprehensive study on the effects of incorporating carbon black into thermoplastic polyurethane to create a nanocomposite coating. They employed a co-coagulation technique followed by hot pressing to fabricate these nanocomposites with varying concentrations of carbon black. Their findings, documented in Figure 19Figure 19, indicated significant improvements in the electrical conductivity, mechanical properties, and thermal stability of the nanocomposites.

The research further examined the erosion behavior of these carbon black-reinforced thermoplastic polyurethane nanocomposites under different conditions, including various impact angles, velocities, and durations. The results demonstrated that carbon black, when used at optimal concentrations, significantly reduced the erosion rate of the nanocomposites. This enhancement in erosion resistance was attributed to increased toughness and hardness of the material, pointing to the efficacy of carbon black as a reinforcing agent in polyurethane composites for improved durability and performance under erosive conditions.

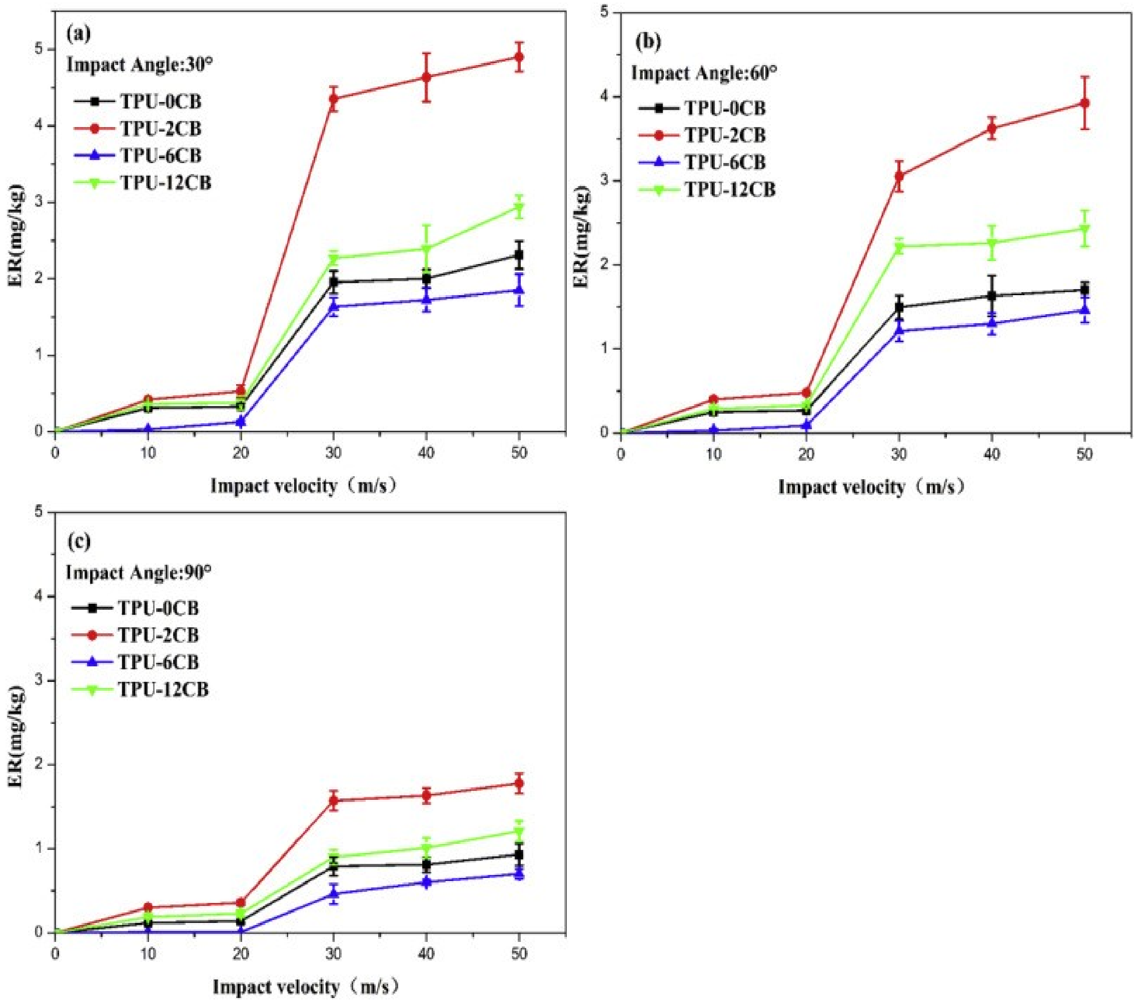

Figure 19. Erosion rate (ER) of tested samples as a function of impact velocity at (a) 30°, (b) 60° and (c) 90° impact angles with the impact time of 300 s, CB=Carbon Black[36].

Miyazaki et al. [37], [38] conducted a series of experimental research on the erosion of polymer composites. In one of their studies [19], they examined the erosion rates (ER) of Nylon 66 and ABS. They observed that the ER increased with the addition or increase of fiber content compared to the neat polymers. Specifically, the findings illustrated in Figure 20 showed that the ER for

Nylon was almost half that of ABS, indicating a significant difference in erosion resistance between these two materials.

In another study by the same researchers [39], the erosion behavior of polyetherketone (PEK) and polyetherimide (TPI) was investigated. They noted a similar trend to that observed in earlier study, with both PEK and TPI showing comparable patterns to PEEK in terms of erosion rates. It was notable that the ER of neat PEK and TPI had similar ranges but differed in the maximum angle at which the highest erosion rate occurred, as detailed in Figure 21. This series of studies highlighted how the incorporation of fibers and the specific type of polymer significantly influence erosion behavior under varying conditions.

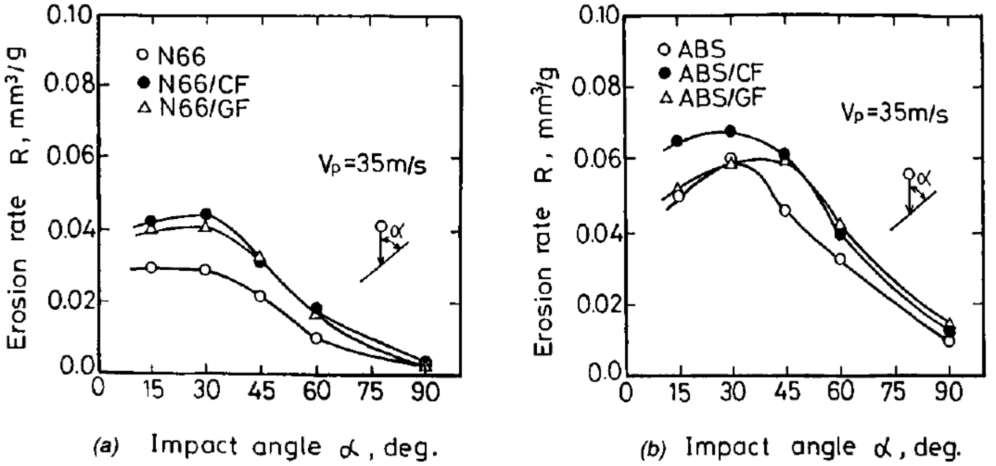

Figure 20. Relation between erosion rate and impact angle (Vp = 35 m/s): (a) N66 FRPS; (b) ABS FRPs [38].

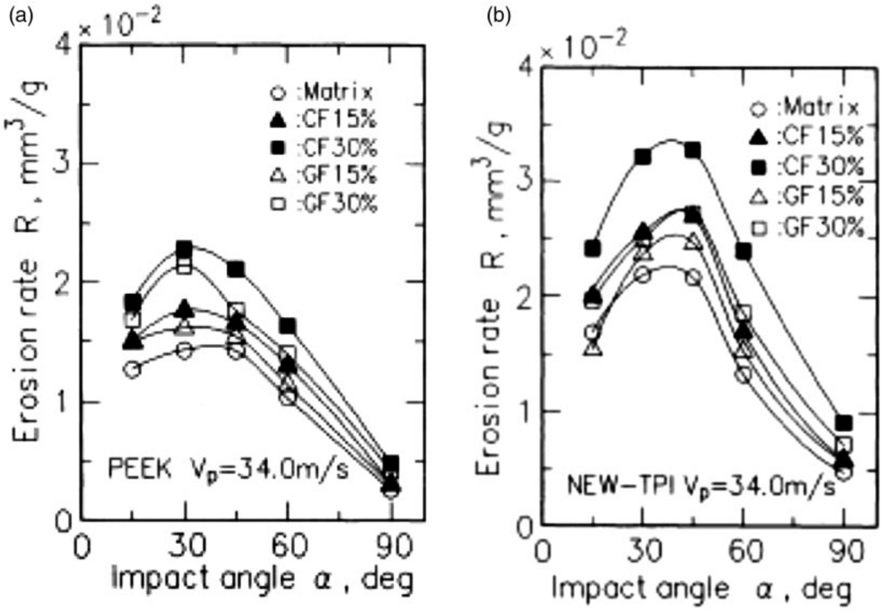

Figure 21. Relation between volumetric erosion rate and impact angle; Vp¼34.0 m/s PEEK composites. (b) New-TPI composites[39].

1.5. Knowledge Gap and Thesis Objective

The existing literature on abradable polymers and their erosion resistance provides valuable insights but often overlooks the specific demands of aerospace applications. While many studies have investigated various aspects of solid particle erosion (SPE), such as the impact of particle characteristics and environmental conditions on different materials, there is a notable lack of comprehensive research focused on abradable coatings with superior erosion resistance. These coatings need to exhibit both high erosion resistance and abradability to ensure the efficiency and longevity of engine components.

Currently, most research on erosion resistance explores the effects of individual factors like particle size or impact angle. However, these studies rarely consider how these factors interact together. This gap highlights the complexity of predicting and enhancing the erosion resistance of polymers in practical settings, where multiple variables must be managed simultaneously.

Additionally, while some polymers show potential in laboratory tests, translating these findings into effective applications remains challenging. The aerospace industry requires materials that not only perform well under laboratory conditions but also offer reliability and durability in real-world operations. This gap between laboratory research and practical application needs addressing to develop materials that can be effectively used in the field.

Moreover, advanced composites that include innovative fillers like carbon nanotubes and hollow glass microspheres have been less explored in the context of abradable coatings. These materials could improve both the mechanical properties and the erosion resistance of coatings, making them ideal for aerospace applications. Yet, detailed studies on how these fillers influence both abradability and erosion resistance in the specific context of aerospace are scarce.

Considering these knowledge gaps, this thesis sets out several defined objectives.

- The first aim is the development and evaluation of thermoset abradable polymer coatings that exhibit enhanced erosion performance suitable for aero engines.
- It also investigates the impact of various composite formulations and fillers on the erosion resistance of these coatings, ensuring they maintain their abradability.
- Furthermore, the work includes a comparative study to benchmark the proposed coatings against commercially available off-the-shelf abradable polymer materials currently used in the aerospace industry.
- Lastly, the thesis seeks to identify optimal composite formulations that balance both erosion resistance and abradability for aero engine applications.

Chapter 2

Materials and Methodology

2. Materials and Methodology

2.1 Methodology

This study aims to identify suitable polymeric material for coating applications in aeroengine environments, specifically focusing on improving engine efficiency by maintaining tight clearance between the stator and rotor blades in the compressor regions. Such coatings, known as abradables or clearance control materials, help prevent crack initiation and propagation, ensuring minimal debris production. The selection process primarily aimed to enhance the erosion resistance of the abradable coating. The research begins with the evaluation of six thermoset epoxy materials, from which one was selected based on superior performance in terms of erosion resistance and then abradability.

The chosen epoxy then served as the matrix for integration with seven different fillers, selected for their potential to enhance lubrication, provide reinforcement, or introduce porosity. Two concentration levels for each filler were tested to find the optimal balance. The main focus was on evaluating how these fillers influenced erosion resistance and also checking their performance in terms of abradability. Accordingly, the filler-filled samples underwent testing, beginning with erosion tests to assess their resistance to wear. Following this, the samples were analyzed using a tribology testing machine to evaluate their abradability. Based on the results of these tests, a subset of fillers was selected for further exploration.

A final composite sample, incorporating the selected epoxy matrix and chosen fillers, was manufactured. This sample was subjected to further tests to examine the combined effects of the fillers on erosion resistance and abradability. Additionally, a rub rig test was conducted to simulate the real-life application of the coating in a controlled setting.

Besides this, several thermoplastic samples were outsourced and evaluated. This group included four neat thermoplastic samples and fourteen compound thermoplastic samples. Each sample underwent a similar process to the thermoset group, starting with the evaluation of erosion behavior. Selected thermoplastic samples that showed promising erosion resistance were further tested for abradability as a secondary criterion to assess their suitability. From this group of materials, two neat thermoplastics and one compound thermoplastic were chosen as final candidates and subjected to rub rig tests to verify their application suitability.

To ensure the developed materials' relevance and competitive performance, all tests were conducted against two commercially available epoxy-based coatings named as reference 1 (abbreviated as ref1) and reference 2 (abbreviated as ref2). This involved consistent testing conditions using the same erosion and tribology test machines. A detailed investigation was also conducted on these benchmark materials to understand their structure.

In this chapter, the test apparatus used in this study were introduced, including the erosion test machine, tribometer abradability test machine, hardness test machine, and rub rig test machine. Additionally, this chapter explores the analysis of the reference materials and details the manufacturing process of the epoxy thermoset samples.

2.1.1. Dry Erosion Test

Erosion resistance of the materials was evaluated in accordance with ASTM G76, employing an erosion testing machine as seen in Figure 22 (TR-470 air jet erosion tester from DUCOM instruments) set to a feed rate of 5 g/min and an erodent velocity of 150 m/s. Alumina was chosen as the erodent due to its standardized application in erosion test. The procedure included the preparation of the specimens, controlled rate of the erosive, and adherence to predetermined test parameters such as duration and impact angle, the schematic of test is presented in Figure 23. Data were gathered regarding the weight loss of the specimens and alterations in surface morphology, which were then analyzed to determine erosion rates and identify wear mechanisms. To ensure the accuracy and reliability of the test results, regular calibration and monitoring were conducted throughout the experimental phases.

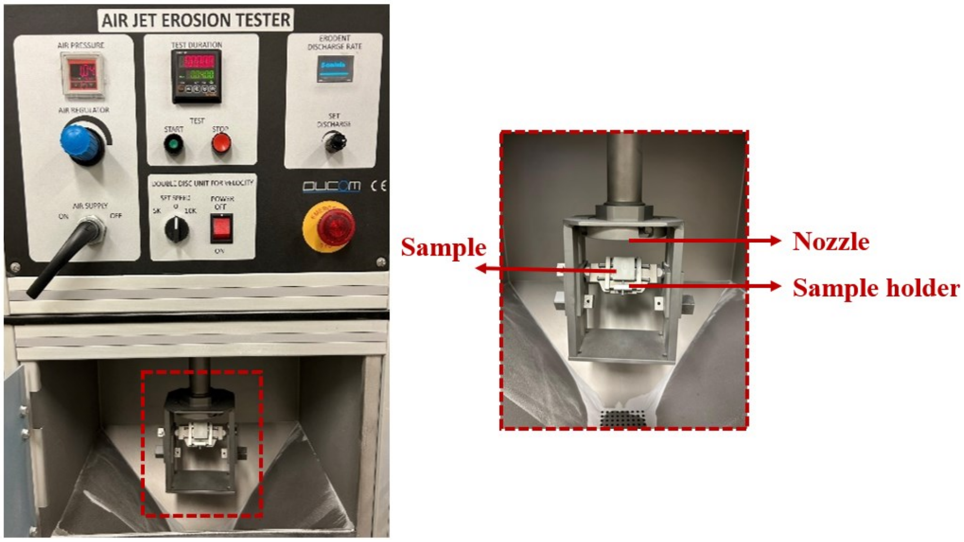

Figure 22. Erosion test instrument.

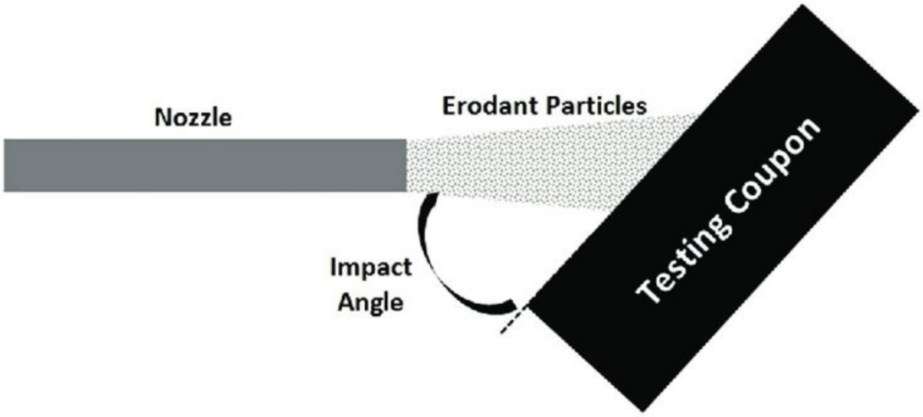

Figure 23. Schematic of erosion test.

An adjustable sample holder was specifically designed and manufactured for the tests. Each sample, approximately 1 inch by 1 inch in size, was cleaned and weighed before the erosion test. The erosion rates presented in the following chapters were conducted at intervals of 1, 2, and 4 minutes. The procedure was that the sample's initial weight was measured using a scale with four-decimal accuracy. Then, the sample was placed in the erosion machine and subjected to erosion for 1 minute. The sample's weight was recorded afterward and then placed in the test for another round of 1 minute; the sample's weight after this was recorded. Next, the sample was subjected to erosion for 2 minutes and the weight was recorded. It was then subjected to another erosion test for a 4-minute round, and the weight was recorded, followed by another 4-minute round, with the weight recorded. Finally, for each sample, the erosion rate was presented as the average of these intervals, considering the erodent rate with time.

The distance between the erodent nozzle and the sample was set at 25 mm. The erosion test was considered as primary test; therefore, this procedure was repeated in all samples for two impact angles 30º and 90º. Erosion Test Parameters are as presented in Table 2.

Table 2. Erosion testing parameters.

Equipment	DUCOM air jet erosion tester
Erodent	Alumina
Velocity	150 m/s
Angle	90º and 30º
SOD	25mm
Feed Rate	5g/min
Particle Size	50μm

2.1.2 Tribometer Pin-on-Flat Test

Dry sliding wear tests were performed on a ball-on-flat reciprocating tribometer (Anton Paar tribometer TRB3, TriTec SA, Switzerland) following ASTM G99. This test was done to find friction and wear characteristics of samples under dry conditions. This testing configuration involves a loaded pin in sliding contact with a flat specimen. Figure 24 shows the test procedure and components. The pin was a titanium-based alloy (Annealed Ti6Al4V), with a spherical shape of ¼ inch diameter. Each test was carried out in an environmental-controlled condition. The tests were performed at room temperature with 20% relative humidity for a duration of 5000 cycles going through total distance of 100m. The test load was set to 5 N and the ball moving with sliding frequency of 1 Hz. Table 3 shows the parameters used in this test.

Table 3. Tribology testing parameters.

Equipment	Anton Paar TRB3
Normal Load	5 N
Sliding speed	1 Hz
Sliding cycles	5000
Sliding amplitude	10 (mm)
Sliding distance	100 (m)
Sample size	1(in) x 1(in)
Counter ball	¼ in diameter spherical Ti6Al4V

The coefficient of friction (CoF) was calculated by the testing machine, considering the testing parameters. CoF is defined as the ratio of the frictional force to the normal force between the two contacting surfaces. The friction force is measured directly by the testing apparatus which is the force resisting the relative motion between the pin and the flat specimen and the normal force is applied by the user which in our case was 5 N. The pin-on-flat test was considered as a secondary testing procedure, to assure whether the best performing samples in terms of erosion have an acceptable abradability performance.

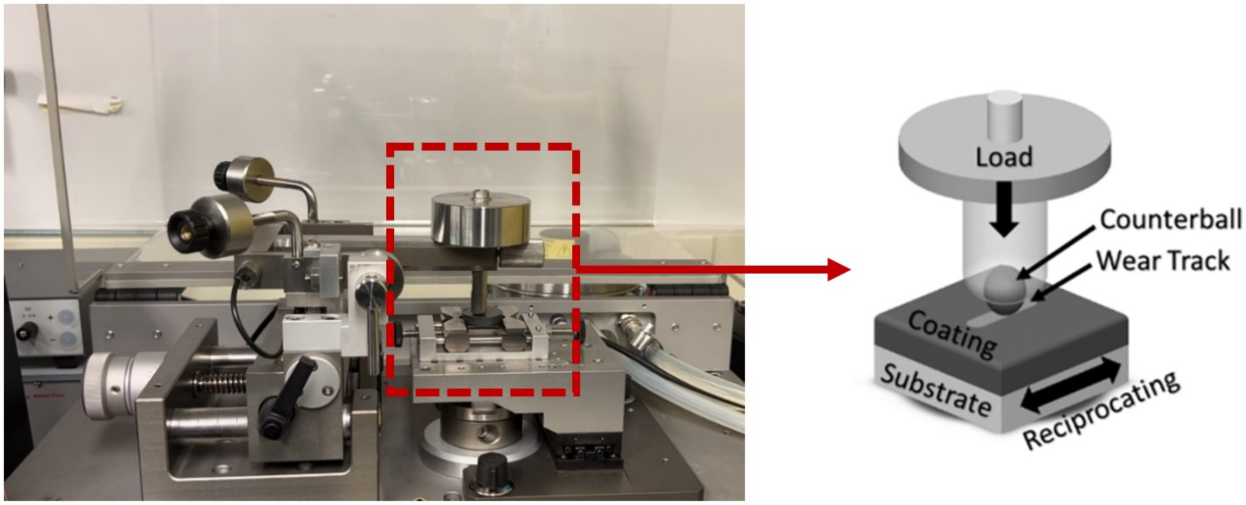

Figure 24. Visual and schematic presentation of the pin-on-flat tribological test setup.[40]

After the pin-on-flat tests the wear profile of the samples were investigated through confocal microscope (Olympus ,LEXT OLS 4100) and the vertical depth of the wear track and the worn area in a cross-section was evaluated from averaged cross-sectional profiles across different positions. The specific wear coefficient was calculated from $w_s = \frac{\Delta V}{F.d}\left(\frac{\mu m^3}{N.m}\right)$, where ΔV is the volume loss in μm^3. F is the applied load in "N" and d is the sliding distance in "m" [41]. The counter balls after this test were also analyzed using SEM, EDS microscope (SEM S-3400N, HITACHI) to examine material transfer on the balls.

2.1.3 Rub Rig Test

The rub rig test was used to evaluate the interaction between a titanium blade and final selected polymeric samples under controlled conditions. This test experimental setup and procedures was used to assess the abradability and wear characteristics of the materials.

The setup presented in Figure 25 consists of a Ti6Al4V (titanium alloy) blade with the dimensions of 10 × 25 × 3.18 mm placed and fixed in the disc rotator. The sample with the size of 1in × 3in with the thickness of no less than 4mm was placed in the sample holder. The test carried out in a way that the blade fixed on the disc rotates at 3600rpm to achieve the maximum linear speed of 50 m/s at the blade tip. The combination of the settled blade speed and incursion rate resulted in an incursion per revolution of 0.83 μm/pass. The test was carried out with a constant incursion rate of 50 μm/s until reaching 1.5 mm incursion depth in the sample. A schematic detailing of the process involved in this test is presented in Figure 26.

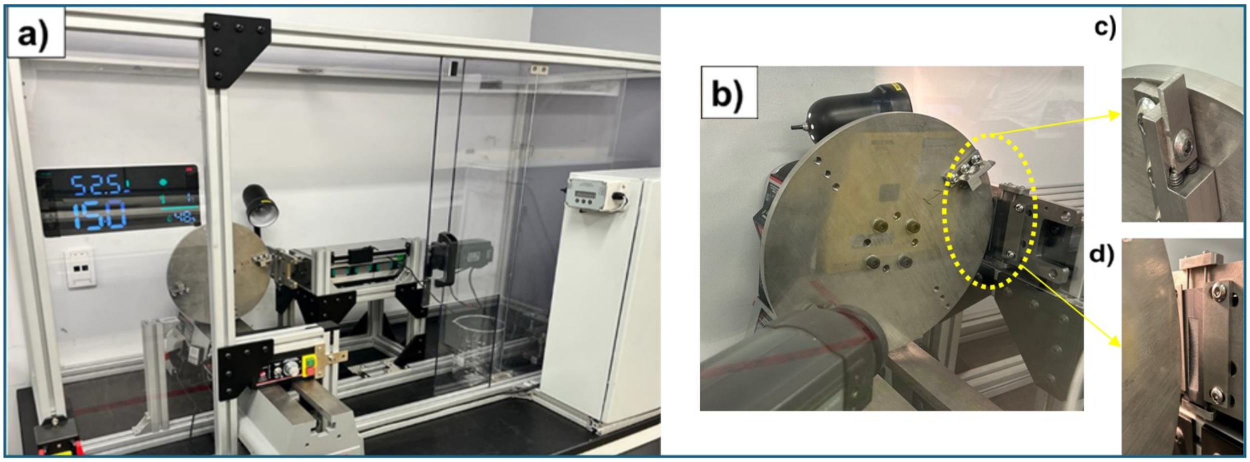

Figure 25. (a) Picture of the rub rig test [40]**; (b) movable specimen stage; (c) close view of the blade in the holder; (d) close view of the abradable sample in the sample holder (the sample of neat resin B, PTFE10%, and CNT0.1).**

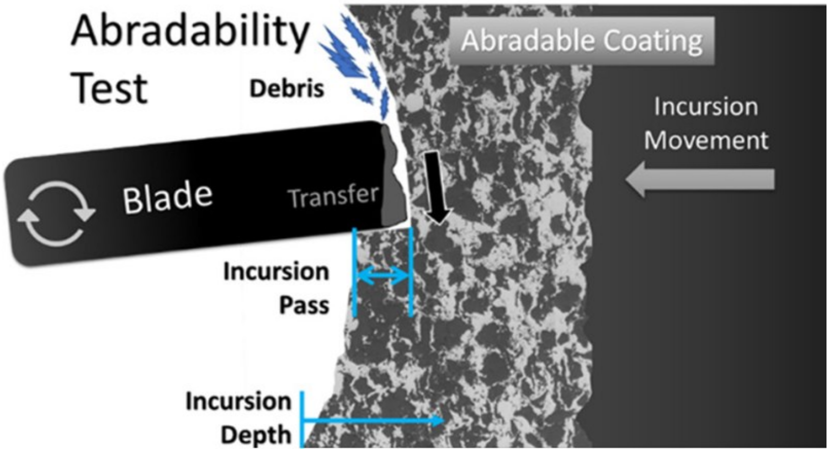

Figure 26. Schematic of the abradability rub rig test[40].

The titanium blade was set to move at parameters detailed in the provided Table 4, which included variables such as blade speed, incursion rate, and incursion depth. During the tests, each blade was indented into the polymeric sample to a maximum depth of approximately 1.5 mm. Temperature variations during the test were continuously monitored using a thermal camera. This instrumentation provided data on the heat generated due to the friction between the blade and the polymeric sample, showing the thermal stability of the materials under the test. Also, the apparatus could produce outputs obtained from the rig during testing, which included the reaction forces (normal and tangential) resulting from the interaction between the blade and the abradable material.

Table 4. Abradability testing parameters of rub rig tester [40]

Parameter	Value
Blade Material	Ti6Al4V
Blade Speed	50 m/s
Cutting Surface	10 x 3.18 mm = 31.8 mm^2
Incursion Rate	50 µm/s
Incursion per Pass	0.83 µm/pass
Incursion Depth	1500µm
Disk Rotation	3600 rpm
Sample Size	25 x 76 mm
Operating Temperature	Room Temperature
Humidity	20%

Following the completion of each test, the blades were subjected to a detailed analysis using Scanning Electron Microscopy (SEM) to assess any wear or structural changes. Additionally, Energy Dispersive Spectroscopy (EDS) was employed to detect and analyze material residues transferred from the polymeric samples to the titanium blades, giving further insight into the wear mechanisms and material compatibility. The surface roughness and characteristics of the worn areas were also examined using a confocal microscope.

2.1.4 Hardness Test (Shore D)

The tool used for the hardness test was the Shore Durometers Figure 27, with the ASTM D2240 standard. The surface microhardness was measured using a square-based pyramid-shaped indent. The average of five measurements was taken at the surface of each sample to accurately evaluate the variability of the hardness, and the error was determined by the standard deviation of the different measurements. The durometer scale reading is proportional to the indenter movement.

Figure 27. Hardness test instrument (Shore D).

2.2 Materials

2.2.1 Reference Materials

In this study, two commercially available coating materials were analyzed as reference materials. The first one, referred to as ref1 and the second one, referred to as ref2. Comprehensive information on the composition and structure of these materials was lacking. The goals were to determine the specific components of each material, establish the concentration of hollow glass microspheres (HGM) - a significant element in these coatings - and measure the size of the HGM found in these materials. This investigation utilized a mix of analytical techniques, physical testing, and microscopy.

For comparison purposes, a sample was also manufactured at Concordia, with 30% by volume concentration of hollow glass microspheres (HGM) blended with an epoxy matrix. The epoxy used was Epon 828 and Epikure 3370, sourced from Miller-Stephenson Company. The hollow glass microspheres, acquired separately from 3M (Aircraft Spruce Canada), had an average diameter of 35 µm, as shown in (Figure 28, left).

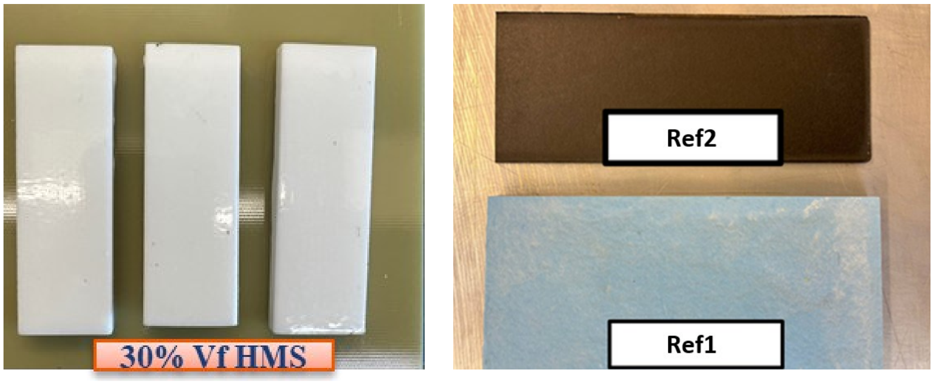

Figure 28. On the left, samples containing hollow glass microspheres (HGM) manufactured at Concordia. On the right, reference samples for comparison.

2.2.1.1 Reference Materials Characterization

2.2.1.1.1 Scanning Electron Microscopy

In the first stage of identifying the components of the reference materials, SEM/EDS analysis was performed. The SEM/EDS results for ref1 are displayed in Figure 29. Analysis of the SEM images combined with EDS data for ref1 reveals the consistent detection of carbon (C) and oxygen (O) across all analyzed spectra suggests an organic base, typical of polymer-based materials like resin.

The presence of silicon (Si) hints at the use of silica, commonly found in hollow glass microspheres (HGM) used within the matrix.

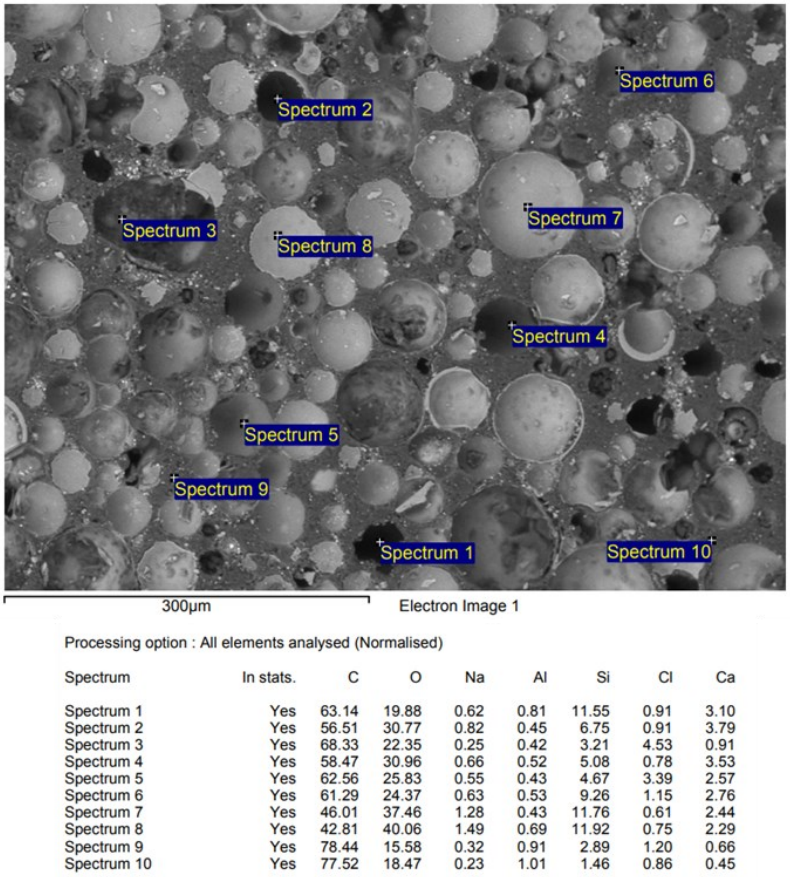

Processing option : All elements analysed (Normalised)

Spectrum	In stats.	C	O	Na	Al	Si	Cl	Ca
Spectrum 1	Yes	63.14	19.88	0.62	0.81	11.55	0.91	3.10
Spectrum 2	Yes	56.51	30.77	0.82	0.45	6.75	0.91	3.79
Spectrum 3	Yes	68.33	22.35	0.25	0.42	3.21	4.53	0.91
Spectrum 4	Yes	58.47	30.96	0.66	0.52	5.08	0.78	3.53
Spectrum 5	Yes	62.56	25.83	0.55	0.43	4.67	3.39	2.57
Spectrum 6	Yes	61.29	24.37	0.63	0.53	9.26	1.15	2.76
Spectrum 7	Yes	46.01	37.46	1.28	0.43	11.76	0.61	2.44
Spectrum 8	Yes	42.81	40.06	1.49	0.69	11.92	0.75	2.29
Spectrum 9	Yes	78.44	15.58	0.32	0.91	2.89	1.20	0.66
Spectrum 10	Yes	77.52	18.47	0.23	1.01	1.46	0.86	0.45

Figure 29. SEM/EDS results for reference 1.

The EDS data shows a variety of elemental signatures, suggesting the complexity of the composite. The occasional presence of sodium (Na) points to its possible use as either a catalyst or a stabilizer within the material's formulation, or it may be part of the hollow glass microsphere (HGM). Aluminum (Al) suggests the incorporation of fillers to enhance mechanical strength, whereas traces of chlorine (Cl) and calcium (Ca) may indicate the presence of hollow microspheres or might be residues from the manufacturing process. These elemental findings imply that the sample's structure extends beyond a simple polymer matrix, likely incorporating microspheres to boost mechanical strength and reduce density.

As follows, the SEM image and EDS data for Reference ref2 is presented in Figure 30. Like ref1, this material features a similar pattern of spherical inclusions within its matrix, but it exhibits distinct elemental differences at the analyzed points.

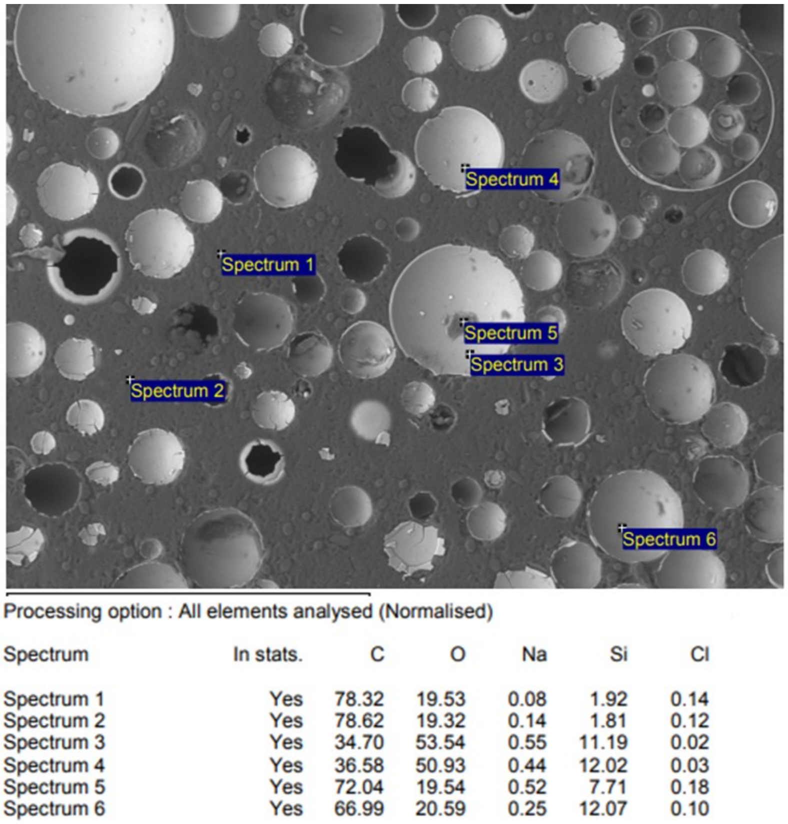

Processing option : All elements analysed (Normalised)

Spectrum	In stats.	C	O	Na	Si	Cl
Spectrum 1	Yes	78.32	19.53	0.08	1.92	0.14
Spectrum 2	Yes	78.62	19.32	0.14	1.81	0.12
Spectrum 3	Yes	34.70	53.54	0.55	11.19	0.02
Spectrum 4	Yes	36.58	50.93	0.44	12.02	0.03
Spectrum 5	Yes	72.04	19.54	0.52	7.71	0.18
Spectrum 6	Yes	66.99	20.59	0.25	12.07	0.10

Figure 30. SEM/EDS results for reference 2.

The SEM image shows a varied array of spherical inclusions within a matrix. Carbon (C) and oxygen (O) are consistent elements, indicating a polymer matrix that might differ from ref1 but is still organic due to the carbon content. Significant amounts of silicon (Si) and chlorine (Cl) suggest the use of silica or glass, typical of hollow glass microspheres. The presence of sodium (Na) indicates similarities in the composite formulations with ref1 or the inclusion of HGMs.

Although the SEM image provides a two-dimensional perspective, variations in the sizes of the spherical inclusions are noticeable. These variations in shading from dark to light imply differences in depth. Darker inclusions are likely closer to the surface cuts, while the lighter inclusions, suggest deeper cuts (Figure 31).

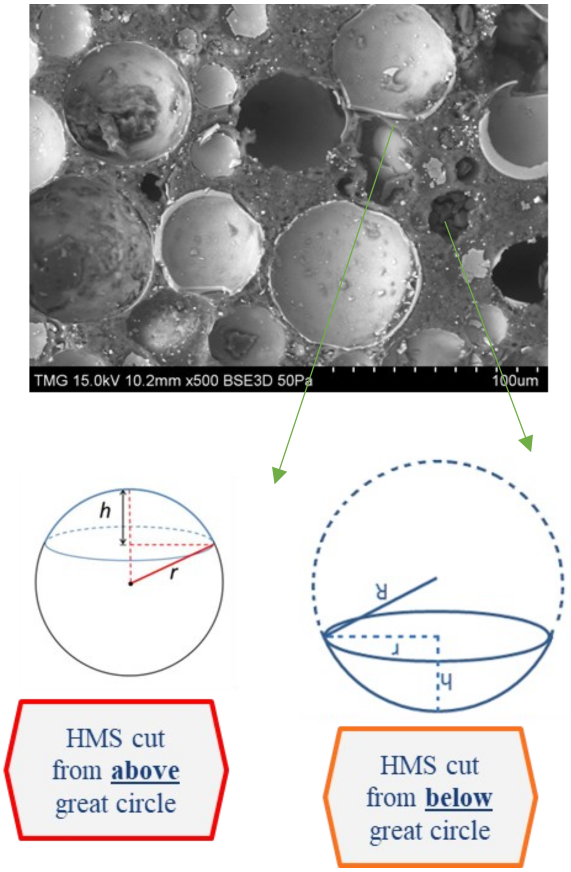

Figure 31. Diverse Sizes of Hollow Glass Microspheres in reference 1.

A thorough analysis of these microspheres enables us to estimate their average size, though the actual diameter may vary depending on the orientation of the microsphere within the material. The data collected provides an estimated size range. This estimated range represents the average size of the hollow microsphere, considering the variability caused by the cutting process.

Upon detailed inspection of the high-magnification SEM images, the small black circles visible within the composite material, determined to have an average diameter of 8.5 µm (Figure 32).

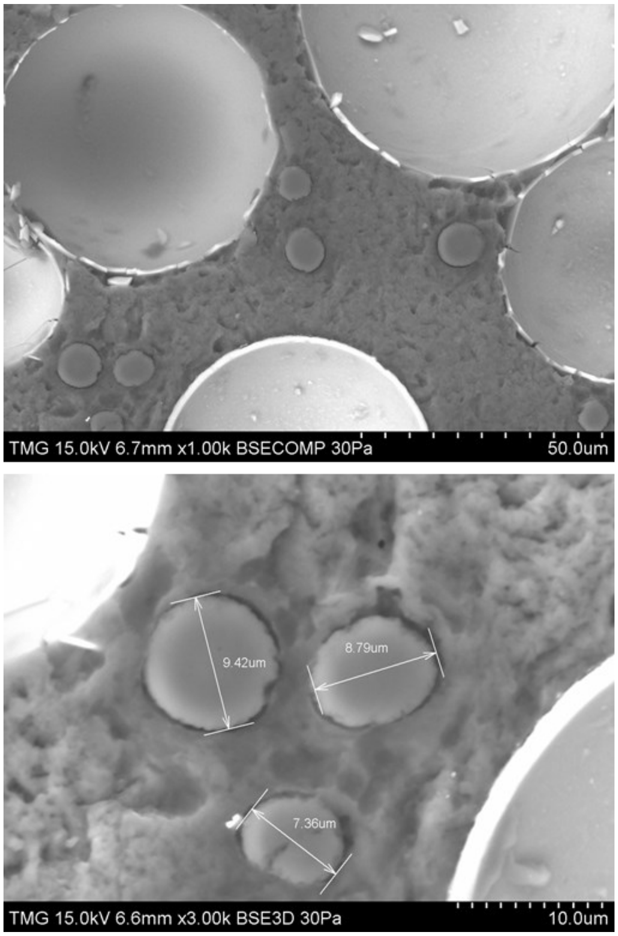

Figure 32. Presence of Small Black Circles Alongside Hollow Glass Microspheres (HGMs).

These particles, noticeably smaller than the previously discussed larger hollow glass microspheres (HGM), display distinct characteristics. EDS analysis of these regions reveals a substantial presence of carbon and oxygen, with slight traces of silicon, indicating that these particles could be carbonaceous fillers rather than silica-based HGMs (Figure 33Figure 33).

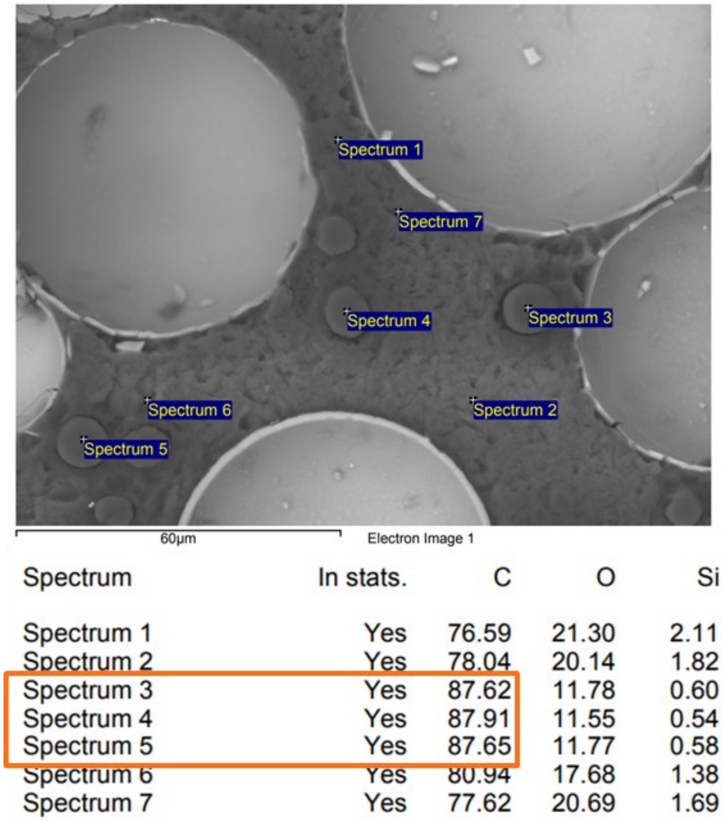

Spectrum	In stats.	C	O	Si
Spectrum 1	Yes	76.59	21.30	2.11
Spectrum 2	Yes	78.04	20.14	1.82
Spectrum 3	Yes	87.62	11.78	0.60
Spectrum 4	Yes	87.91	11.55	0.54
Spectrum 5	Yes	87.65	11.77	0.58
Spectrum 6	Yes	80.94	17.68	1.38
Spectrum 7	Yes	77.62	20.69	1.69

Figure 33. SEM/EDS results for small black circles.

To determine the volume concentration of hollow microspheres (HGM) in reference materials, we employed ImageJ, an image analysis software. Figure 34 displays the results of the HGM volume fraction for both reference materials, alongside the sample produced at Concordia with a predetermined concentration of HGMs.

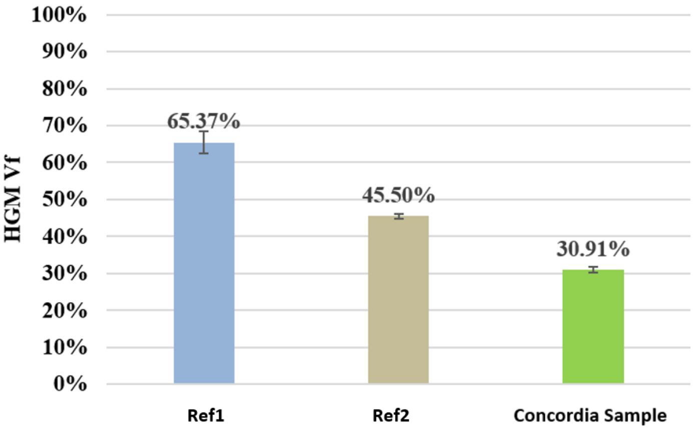

Figure 34. Volume Fraction of Hollow Glass Microspheres (HGMs) in Reference Materials using image analysis.

The bar chart analysis quantifies the concentration of hollow microspheres in the samples, with a significant result for the Concordia University sample. This sample, known to contain a 30%

concentration of microspheres, underwent the same detailed image analysis as the commercial samples, ref1 and ref2. The Concordia sample's resulting data point of 30.91% confirms the accuracy of the analytical process, closely matching the expected value. This outcome not only validates the methodology showing microsphere concentrations observed in ref1 at 65.37% and for ref2 at 45.50%.

2.2.1.1.2 Micrography

Continuing our analysis, we utilized micrography to evaluate the dimensions of the hollow microspheres (HGM), as shown in Figure 35. The top image presents a color-contoured surface profile of a microsphere, showcasing variations in height and curvature that emphasize its three-dimensional structure. The image at right provides a cross-sectional view, highlighted by a line that represents the cut plane through a microsphere. The graph below plots the cross-sectional profile, depicting the depth of the sphere from its surface to its base, which facilitates precise measurement of the HGM dimensions.

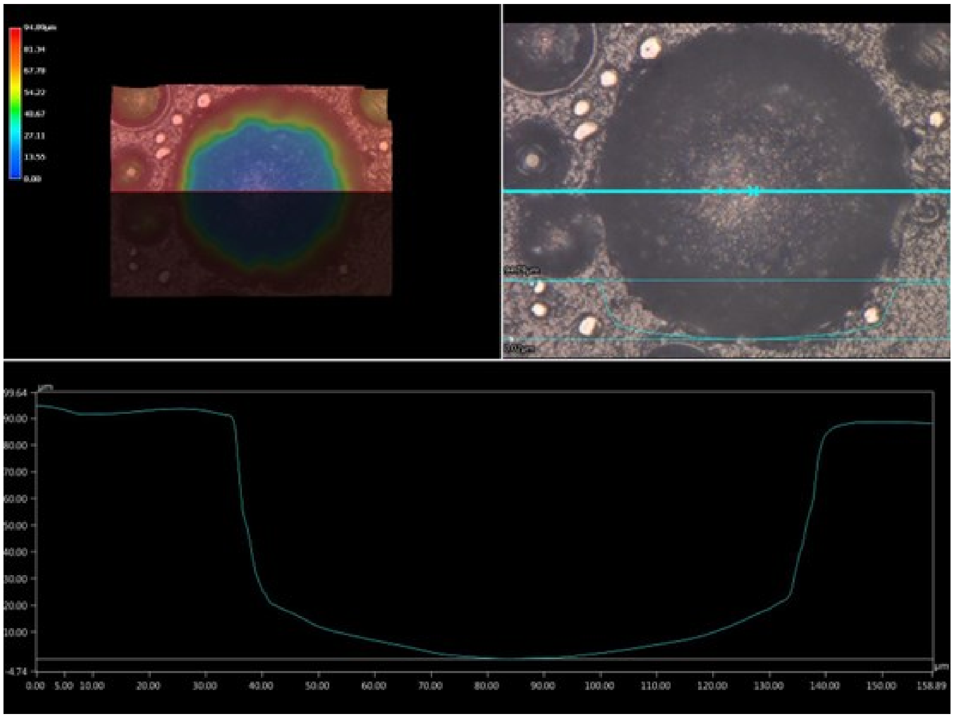

Figure 35. Measurement of the Dimensions of the Hollow Glass Microspheres (HGMs).

The dimensional analysis of hollow microspheres in our two reference materials and the Concordia sample is detailed in Figure 36. The microspheres in the ref1 sample had an average radius of 41.84 µm. In contrast, those in the ref2 sample are larger, with an average radius of 52.10 µm, while the Concordia sample contains smaller microspheres, with an average radius of 30.27 µm.

The typical particle diameter of HGM used in the Concordia sample is reported as 35 µm by the source company, aligning closely with the observed results.

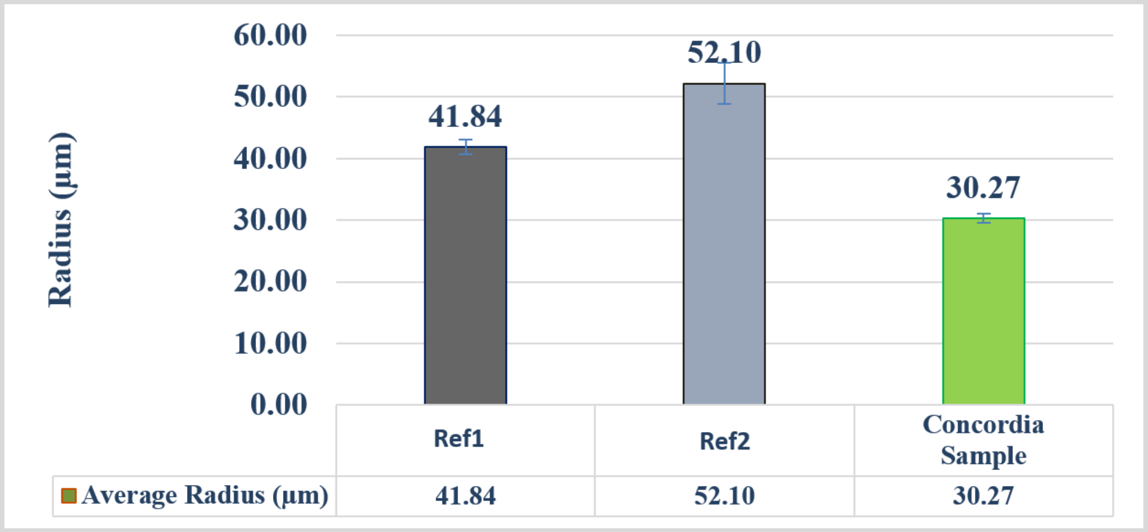

Figure 36. Measurement of the average radius of HGMs.

2.2.1.1.3 Density measurement

Density tests for the ref2, ref1, and the Concordia-made sample were conducted using Archimedes' principle with YDK01 density kit based on ASTM D792-20[42]. Each sample, after being cleaned and sized to approximately 0.5 by 1 square inches, was first weighed in air (W(a)) and then submerged in distilled water at 20.5 °C, which has a known density of 0.99813 g/cm^3. The weight of the submerged sample (W(fl)) was recorded using a setup specifically designed to keep the sample underwater. The density of each sample was calculated based on these weights and the water's density. This method allows for comparison of the samples' densities relative to that of the water (Figure 37).

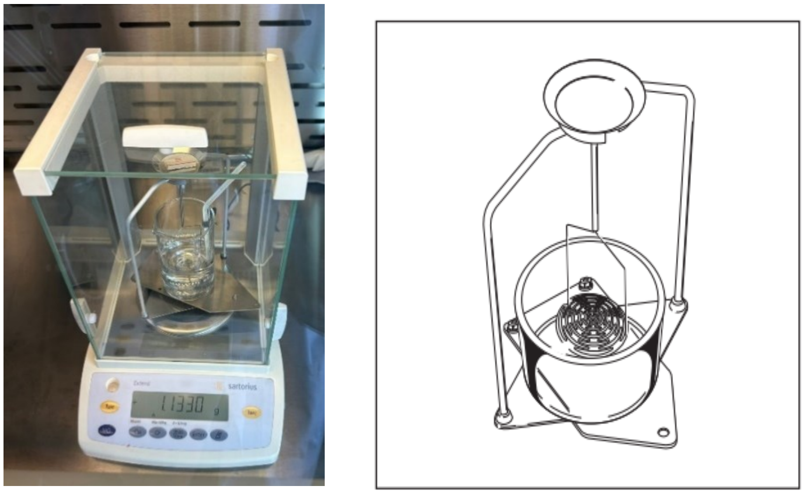

Figure 37. Density measurements setup.

Using the following equation from the kit manual, the density was calculated.

$$\rho = \frac{W(a).[\rho(\mathrm{fl}) - 0.0012 g/cm^3]}{0.99983\, G} + 0.0012\ g/cm^3$$

W (a) and G in g; ρ (fl) in g/cm^3

$$G = W(a) - W(\mathrm{fl})$$

ρ = Specific gravity of the solid.

ρ (fl) = Density of the liquid.

W (a) = Weight of the solid in air.

W (fl) = Weight of the solid in liquid.

G = Buoyancy of the immersed solid.

The volume fraction of hollow glass microspheres (HGM) in the ref1 and ref2 samples was determined using the density method. This method involved testing six samples of each material to calculate an average volume fraction. Using the densities obtained from these samples and applying the rule of mixtures with an assumed resin matrix density of 1.1 g/cm³ and an HGM density of 0.2 g/cm³—the HGM volume fractions were calculated and reported in Figure 38.

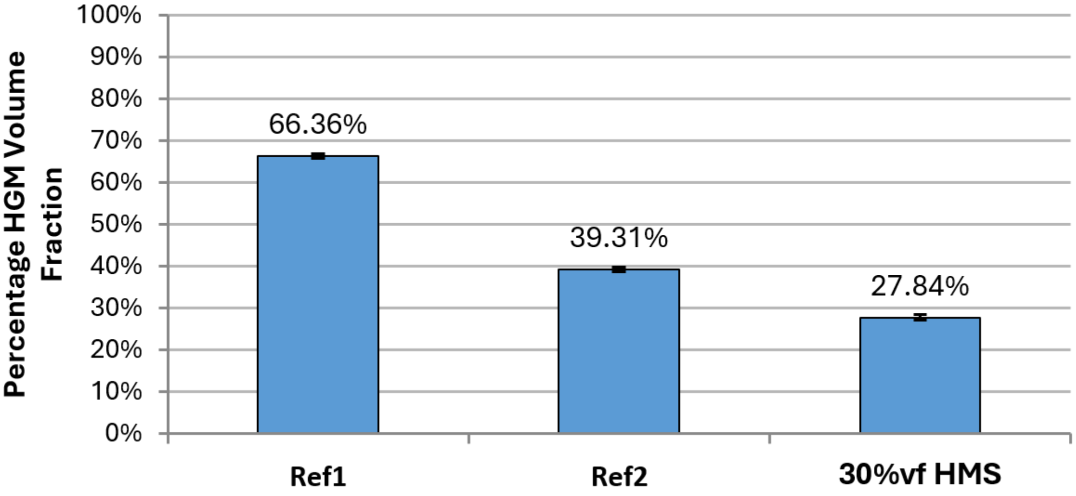

Figure 38. Volume Fraction of Hollow Glass Microspheres (HGMs) in Reference Materials using the density method.

The analysis revealed a substantial presence of hollow glass microspheres (HGM) in the ref1 sample, with an average volume fraction of 66.36%. In contrast, the ref2 sample exhibited a lower average volume fraction of 39.31%, while the Concordia Sample, used for benchmarking, recorded an average volume fraction of 27.84%.

2.2.1.1.4 Thermogravimetric Analysis

Thermogravimetric Analysis (TGA) is a thermal analysis technique used to evaluate material behavior under different temperatures. In a TGA test, a sample is heated at a consistent rate while its weight is continuously recorded, either as a function of temperature or time. TGA enables the determination of a sample's thermal decomposition temperature and quantifies mass loss at various temperatures by analyzing the weight reduction over time. This analysis helps determine the quantity of inorganic material, specifically in our case, hollow glass microspheres (HGM), in the samples.

The objective for performing TGA tests, in this study, was to determine the volume fraction of the HGM in the samples. To do that, two samples, from different locations of each reference material were extracted and were subjected to TGA test. The maximum temperature for this test was set at 750 °C and the test was performed for 100 minutes. The results showed a significant variation in HGM volume fraction of similar samples that were extracted from similar material. This variation is potentially due to the very small size of samples (a few milli grams) that can be analyzed by this test, which makes the samples not to be the representative of the whole material.

For this study, TGA tests were conducted on two samples from each reference materials, as well as on a Concordia-made sample containing a 30% volume fraction of HGM, which served as a benchmark. The outcomes are graphically represented in TGA curves, showing the percentage of mass loss relative to temperature and time, as illustrated in Figure 39, Figure 40, and Figure 41.

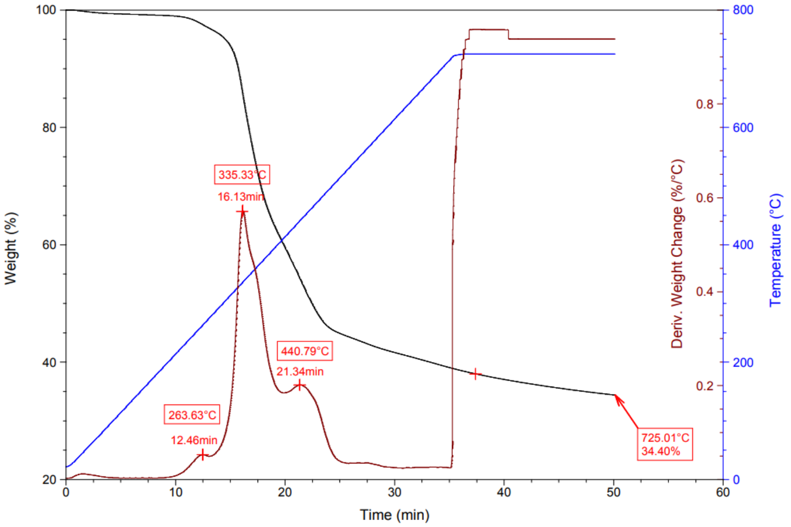

Figure 39. TGA test result for reference 1.

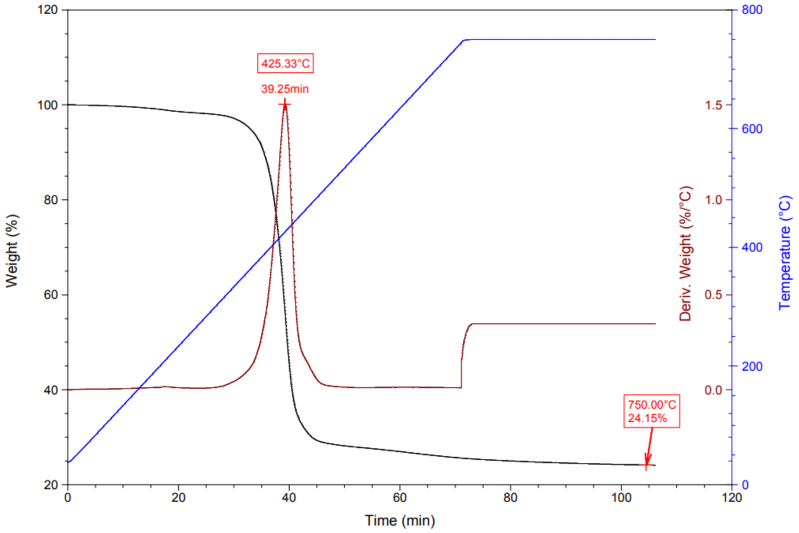

Figure 40. TGA test result for reference 2.

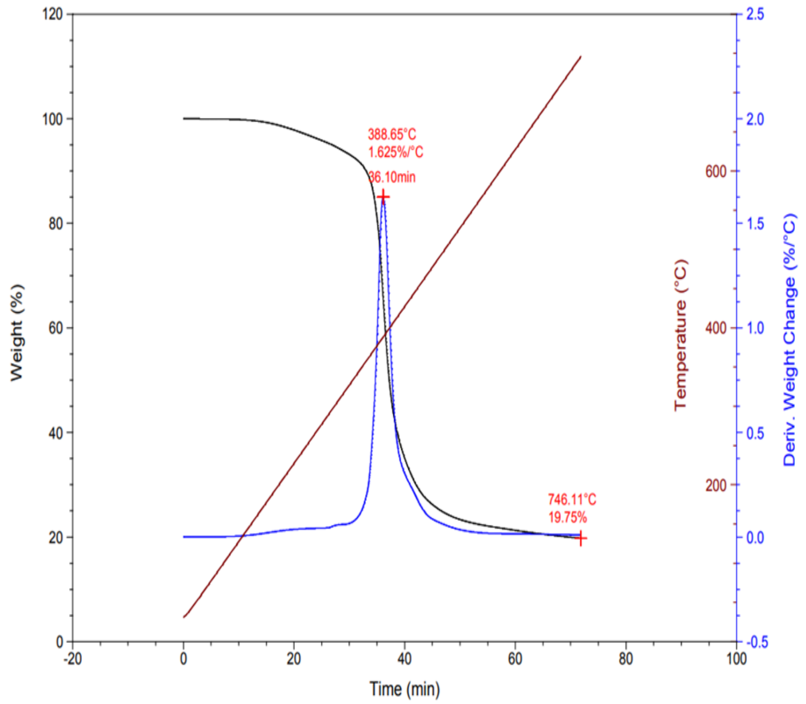

Figure 41. TGA test result for Concordia sample.

2.2.1.1.5 Muffle furnace

The primary objective of muffle furnace test for reference materials was to measure the amount of inorganic material, specifically hollow microspheres, present in each sample. The test as shown in Figure 42, involved heating the samples to high temperatures to combust the organic components, thereby isolating the inorganic residue of glass hollow microspheres. Samples were initially weighed, then heated to specific temperatures, and reweighed to assess the residue.

This analysis was conducted on two samples, ref1 and ref2, and Concordia-made sample containing 30% hollow glass microspheres (HGM), designed for benchmarking purposes. The substantial presence of HGM in the ref1 samples was confirmed, with less detected in ref2 and the Concordia sample showing results that substantiate the test's closeness to the actual value. The findings, detailed in Figure 43, validate the efficacy of this method in quantifying the inorganic content within these materials, providing critical data for further evaluations.

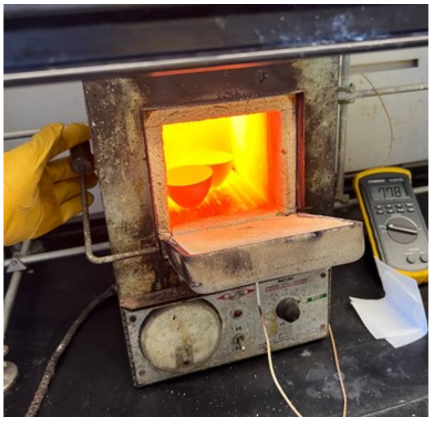

Figure 42. Muffle furnace picture.

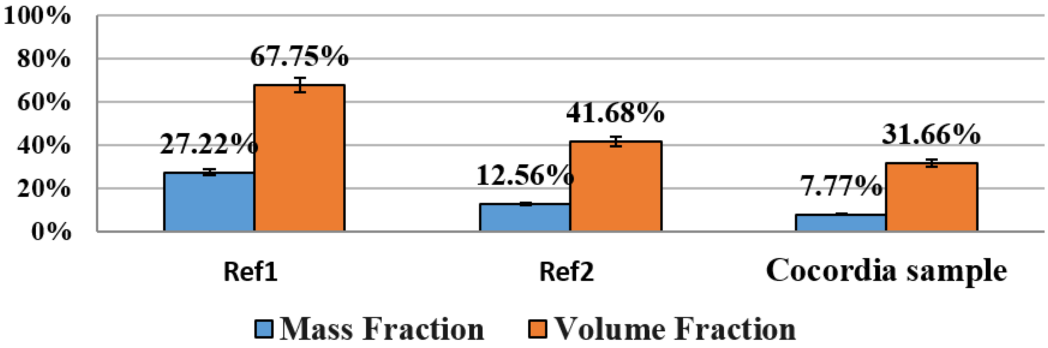

Figure 43. HGM volume fraction from Muffle furnace method.

The results of the HGM volume fraction obtained from the tested analytical methods are illustrated in Figure 44, allowing for a detailed comparison. The muffle furnace, density, and micrography along with SEM tests closely match the benchmark of 30% HGM volume fraction established by the Concordia sample, demonstrating a high degree of methodological accuracy. In contrast, the TGA test results show a notable variance, with a recorded volume fraction of 54.78% for the Concordia sample, indicating potential reliability issues, possibly attributed to the small sample sizes used in the tests. From these comparative analyses of reference materials, it is estimated that the ref1 sample contains approximately 66.5% HGM volume fraction, while the ref12 sample has around 42% HGM.

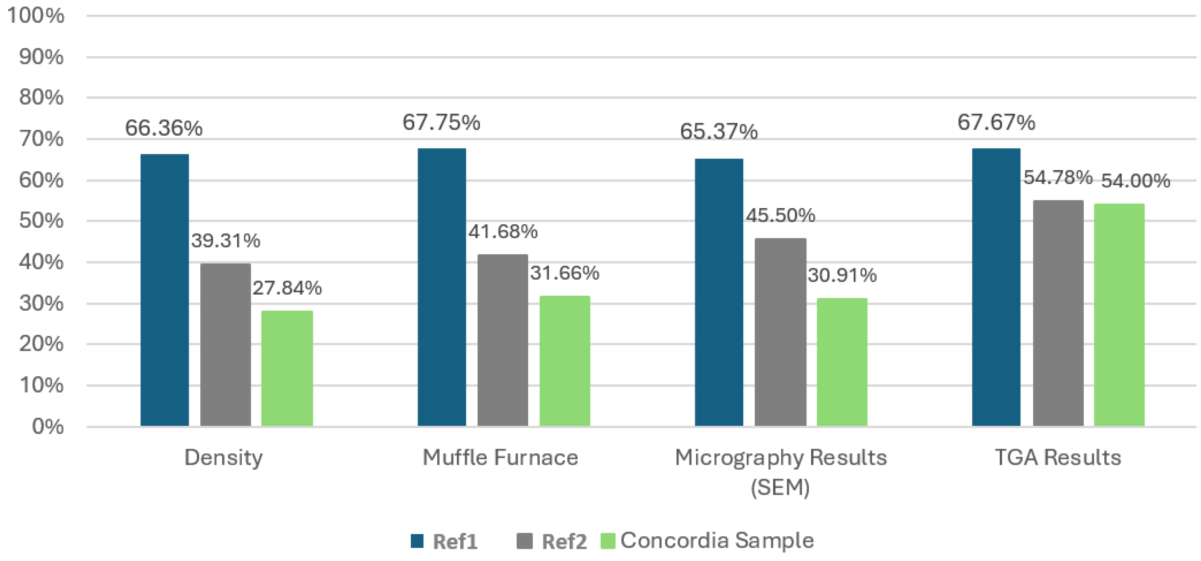

Figure 44. HGM volume fraction based on test results using different methods.

2.2.2 Thermoset Samples

Epoxy resins were the material of choice for this study. We selected two base epoxies, Epon 862 and Epon 828, and combined them with three different curing agents: Epikure 3164, Epikure 3274, and Epikure 3370 all purchased from miller-Stephenson. This combination yielded six distinct resin formulations, all of which were cast and prepared for evaluation in the matrix selection process.

The fabrication process for the epoxy resin samples involved combining Epon with the curing agent at a specified ratio based on their technical data sheet presented in Table 5. Initially, the epoxy and curing agent were manually mixed in an aluminum container as seen in Figure 45, then placed into specially designed 3D printed cups. To avoid air entrapment, the cup with the mixture was processed in a vacuum mixer. Following mixing, the material was allowed to set in room conditions for 24 hours, then post-cured for 2 hours at 100°C. After post-curing, the sample was demolded and cut from the aluminum container to a size of 1×1 inch. The material was cured in the same container without being transferred to another mold, which helped reduce air entrapment and minimized the void content.

Table 5. Mixing ratio for neat resin manufacturing.

Resin Mixing Ratio			
Epon 828/862	100	Epikore 3274	40
		Epikore 3370	38
		Epikore 3164	136

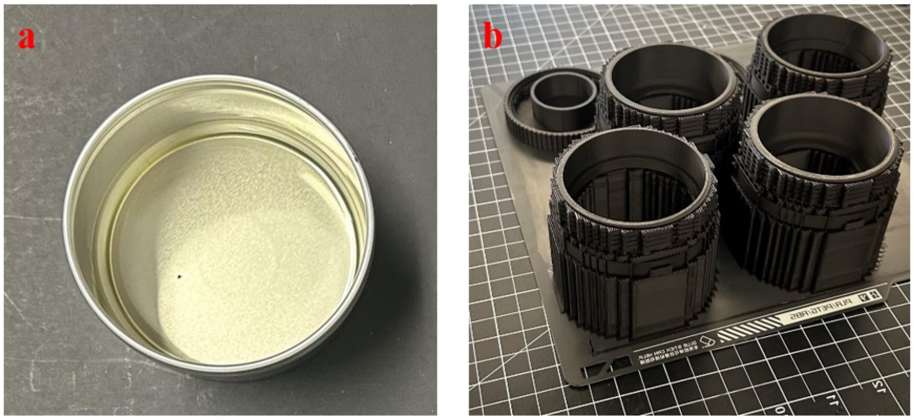

Figure 45. a) Aluminum cup containing neat resin, b) 3D printed cups.

To ensure a uniform surface, the samples were then machined using CNC to remove the upper 2-3 mm of the sample surface, achieving a consistent thickness of 8mm. This step was crucial for standardizing the samples for subsequent testing and analysis.

2.2.3 Thermoset-Filler Samples

To improve the erosion resistance and abradability of the thermoset resins, seven different fillers were tested at two concentration levels. These fillers were chosen based on their potential to enhance lubrication, provide reinforcement, or introduce porosity, such as hollow glass microspheres. Each filler was incorporated into the resins at both low and high concentration, leading to the creation of two groups of filler-enhanced samples for comparative analysis. Consequently, this approach produced a total of 14 testable samples containing fillers.

Table 6 details the seven fillers used, outlining their specific roles, whether for lubrication, reinforcement, or porosity, and their respective concentration levels.

Table 6. Fillers utilized and their concentration levels for sample preparation

Fillers	**Role**	**Levels (VF %)**	
		Lower Concentration	Higher concentration
Graphite	Lubricant	0.5 wt%*	1 wt%*
Silicone Powder	Lubricant	5	10
PTFE Powder	Lubricant	10	20
CNT	Reinforcement	0.1 wt%*	0.3 wt%*
Milled Carbon Fiber	Reinforcement	10	30
Aramid Fiber (Kevlar)	Reinforcement	10	20
HGM	Porosity/impact	30	60

The milled carbon fibers (PX35) were sourced from ZOLTEK, while the hollow glass microspheres were acquired from 3M (Aircraft Spruce Canada), with these HGMs measuring 35 μm in size. The Kevlar pulp (glass bubbles K20 series) and the PTFE micro-powder (POLYFLON PTFE- F104) were also purchased from 3M (Aircraft Spruce Canada) and DAIKIN, respectively. Silicon powders (SI102) came from Atlantic Equipment Engineers (AEE), and the CNT (single-wall carbon nanotubes 75%) was obtained from TUBALL.

To individually assess the impact of each filler on erosion and abradability, samples with a single type of filler were created. These fillers were incorporated into a base resin, composed of Epon 828 and Epikure 3274, with a specified mixing weight ratio of 100 parts Epon to 40 parts Epikure. By knowing the densities of each filler and by measuring the density of neat resin sample (1.1 g/cm³), we were able to resin-cast the samples.

The process involved calculating the masses of Epon 828 (part A), Epikure 3274 (part B), and the fillers based on their densities. After weighing, the fillers were mixed with Epon 828 in an aluminum container. This mixture was then placed in a 3D-printed cup and subjected to a vacuum mixer for 200 seconds. To manage the exothermic reaction, the mixture was cooled on ice before adding Epikure 3274 and returning it to the vacuum mixer for another 100 seconds. The calculations were based on the rule of mixture where m_F is the mass of filler, total mass of resin, v_f is the volume fraction, ρ_F density of filler, and ρ_r is the density of resin [43]

$$m_F = m_r \frac{\rho_F}{\rho_r} \times \frac{v_f}{(1 - v_f)}$$

As an example, in the resin casting of a sample containing 10% milled carbon fiber, where the density of the milled carbon fiber was 1.8 g/cm³ and the density of the resin was 1.1 g/cm³, the process began with measuring 42.857 g of Epoxy (part A) and pouring it into an aluminum cup. Next, 10.909 g of milled carbon fiber was measured and added to the same cup. At this stage, the materials were manually mixed and then placed in a 3D-printed container which was subsequently placed into a vacuum mixer for 200 seconds. After this mixing period, the aluminum cup was removed and cooled on ice. Subsequently, 17.143 g of Epikure 3274 was measured and added to the mixture. This mixture was then returned to a 3D-printed container and vacuum mixed for an additional 100 seconds.

The container was then set aside to cure at room temperature for 24 hours, followed by a 2-hour post-cure in oven at 100°C. After cooling, the sample was demolded from the aluminum container and then went through CNC machining as presented in Figure 46, to have leveled surface and same thickness, then cut into pieces each 1 × 1 inch.

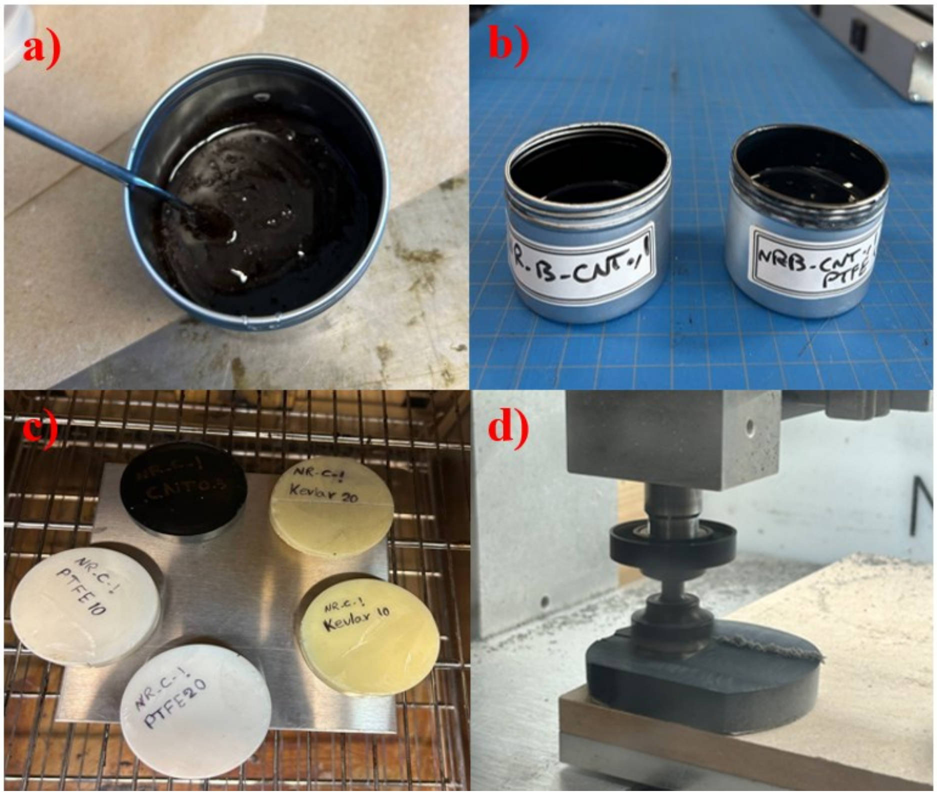

Figure 46. (1) Picture of the sample containing resin and filler (CNT) being hand-mixed, (2) Picture of the samples in aluminum cups prepared to be cured at room temperature, (3) Picture of samples containing fillers being post-cured in oven, and (4) Picture of a sample containing resin and CNT undergoing CNC surface machining.

For manufacturing samples containing Carbon Nanotubes (CNT), the rule of mixture was applied to determine the precise amounts of CNT and resin needed. An initial high-concentration CNT mixture with 0.5 wt% CNT was created by precisely combining 248.24 grams of Epon 828 resin with 1.758 grams of CNTs. This specific ratio ensures that, when mixed with the correct amount of hardener (99.296 grams of Epikure, assuming a 100:40 parts by weight ratio of resin to hardener as specified in the datasheet), the final mixture maintains the 0.5 wt% CNT concentration. The mixture then underwent a three-roll milling process to achieve proper dispersion as in Figure 47.

To prepare a sample with reduced CNT concentrations of 0.1 wt% or 0.3 wt%, calculated portions of the initial mixture were diluted with additional Epon 828. For instance, to achieve a 0.1 wt% CNT concentration, 7.1571 grams of the initial mixture were combined with 28.5714 grams of additional Epon 828. This combination was first hand-mixed to ensure initial blending, then further mixed in a vacuum mixer for 200 seconds. The mixture was cooled using ice to stabilize the viscosity and prevent premature curing. Afterward, 14.2714 grams of Epikure 3274 hardener were added, and the mixture underwent another round of vacuum mixing for 100 seconds. The final curing process involved setting the mixture at room temperature for 24 hours, followed by a 2-hour post-cure at 100 °C to ensure complete polymerization and hardening of the resin.

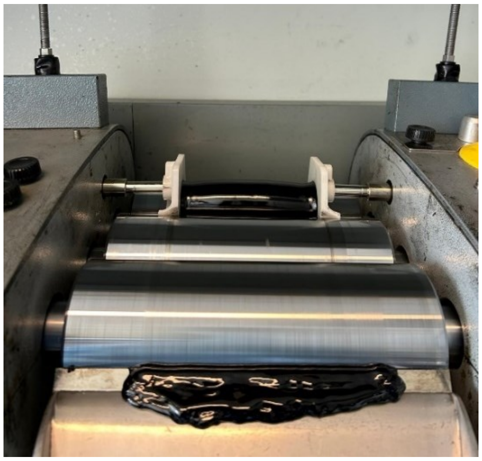

Figure 47. Dispersion of carbon nanotubes in epoxy resin using a three-roll Mill.

2.2.4 Thermoplastic off-the-Shelf Samples

In the thermoplastic category, our study focused on evaluating four distinct materials: Ultra-High Molecular Weight Polyethylene (UHMW-PE), Polyphenylene Sulfide (PPS), Polyetherimide (PEI), and Polyether Ether Ketone (PEEK). These neat thermoplastic materials were specifically chosen for their exceptional chemical resistance, melting temperature as you can find in table 8. Notably, the PEEK samples were fabricated at Concordia using compression molding technique. The remaining samples were received from COALIA, Centre de recherche in Quebec, which also utilized compression molding for their production.

Table 7. List of properties for the thermoplastic samples.

Polymer Name	Tg Min value (°c)	Tg Max value(°c)	Tg Average (°c)	Melting Temp. (°C)	Weak acids	Strong acids	Weak alkalis	Strong alkalis	Organic solvents	Alcohols	Hydrocarbons	Fuels	Gamma radiation	UV radiation	Index
PA 6 - Polyamide 6	60	60	60	268	G	P	E	F	E	G	G	G	F	F	**E: excellent**
PA 66 - Polyamide 6-6	55	58	56.5	268	G	P	E	F	E	G	G	G	F	P	**G: good**
PEEK - Polyetheretherketone	140	145	142.5	349-399	E	E	E	E	E	E	E	G	G	G	**F: Fair**
PPA- Polyphthalamide			135	325	E	G	E	G	E	G	E	G	G	F	**P: poor**
PPS - Polyphenylene Sulfide	88	93	90.5	307-329	E	E	E	E	G	E	E	G	G	G	
PEI- Polyetherimide			215	217	E	E	E	E	G	E	E	G	E	G	
UHMWPE- Ultra-High Molecular Weight Polyethylene				-	E							E			

In addition to four neat thermoplastic samples, other commercially available thermoplastic compounds were also received for further evaluation. These commercially available compounds were sourced from RTP Company, Stratasys, and McMaster-Carr and presented in Table 8. The lineup includes RTP Company samples, which are precision-crafted via injection molding, Stratasys samples fabricated using 3D printing technologies, and McMaster-Carr samples that consist of various silicone rubber compounds known for their exceptional erosion resistance.

Table 8. Off-the-shelf thermoplastic compound materials and their compositions

Code	Material	Main Components
3D-A	Antero 840 CN03	PEKK + CNT
3D-B	Ultem 9085	PEI (polyetherimide)
3D-C	Ultem 1010	PEI (polyetherimide)
RTP-A	RTP 200 AR 15 TFE 15 SI 2	Nylon 6/6 +AR,PTFE,Si
RTP-B	RTP2299x-120345	PEEK + CF,Gr,PTFE
RTP-C	RTP 200 A ABR	Nylon 6 +Abrasion Resistant
RTP-D	RTP 4000 AT	PPA+ Impact Modified
RTP-E	RTP 4083 AR10 TFE 15 SI 2	PPA+ CF,AR,PTFE,Si
SR-A	Silicone rubber hardness: 40a	
SR-B	Silicone rubber hardness: 50a	
SR-C	Silicone rubber hardness: 60a	
SR-D	Silicone rubber hardness: 70a	
SR-E	Silicone rubber, High strength	
SR-F	Silicone rubber chemical resistant	

Chapter 3

Matrix Selection

3. Matrix Selection

3.1 Erosion Test Results

The selection of the optimal abradable coating material begins with the crucial step of matrix identification. Epoxy resin was chosen as the thermoset candidate, and six combinations of resin were subsequently selected. These samples were resin cast and initially subjected to erosion testing. Among these, the resin that exhibited the best performance in terms of erosion resistance was selected and then subjected to an abradability check using a pin-on-flat test. Finally, the selected resin was used as the matrix and combined with chosen fillers.

Erosion rate was evaluated for six neat resin samples as part of this study, aiming to identify the best sample based on the lowest erosion rate, which indicates the highest erosion resistance. Tests were conducted on the samples at 30° and 90° angles to compare these resins with each other and against two commercially used materials, ref11 and ref12, serving as benchmarks. Six neat resin samples, each formulated from combinations of Epon and Epikure resins as detailed in Table 9, underwent erosion testing as illustrated in Figure 48. This figure displays the samples after the erosion test. These tests were specifically designed to assess the erosion resistance of the resins under erosive conditions at both 30-degree and 90-degree angles.

Table 9. Neat epoxy resin sample material.

Code	Material
NR-A	Epon 828, Epikure 3370
NR-B	″ , Epikure 3164
NR-C	″ , Epikure 3274
NR-D	Epon 862, Epikure 3370
NR-E	″ , Epikure 3164
NR-G	″ , Epikure 3274

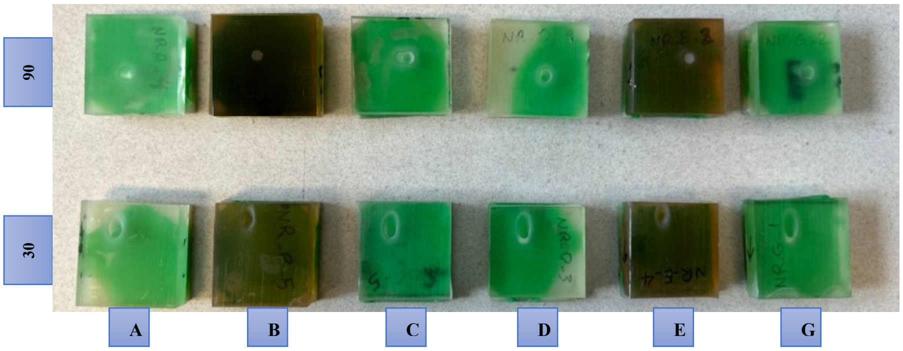

Figure 48. Neat resin samples in 30-degree and 90-degree angles after erosion tests.

The results, presented in Figure 49 show that all samples displayed a wear pattern characteristic of ductile materials, particularly at the 30° angle where erosion rates were higher compared to the 90° angle. This is typical for ductile mode erosion, where maximum material removal occurs at low impingement angles, while at high angles, the erosion mode is more brittle. This pattern was consistent with the commercially used materials as well.

Among all the samples, the resin combinations of NR-B, Epon 828 with Epikure 3164, and NR-E, Epon 862 with Epikure 3164, demonstrated the lowest erosion rates at both angles, outperforming the reference materials and other epoxy samples.

In the ductile erosion observed, the erodent particles strike the surface more obliquely at lower angles (30°), leading to a sliding or scraping action rather than direct impact, which results in higher erosion rates. The neat resin samples, especially those combined with Epikure 3164, showed superior resilience by effectively dissipating the kinetic energy of the impacting particles through their structure.

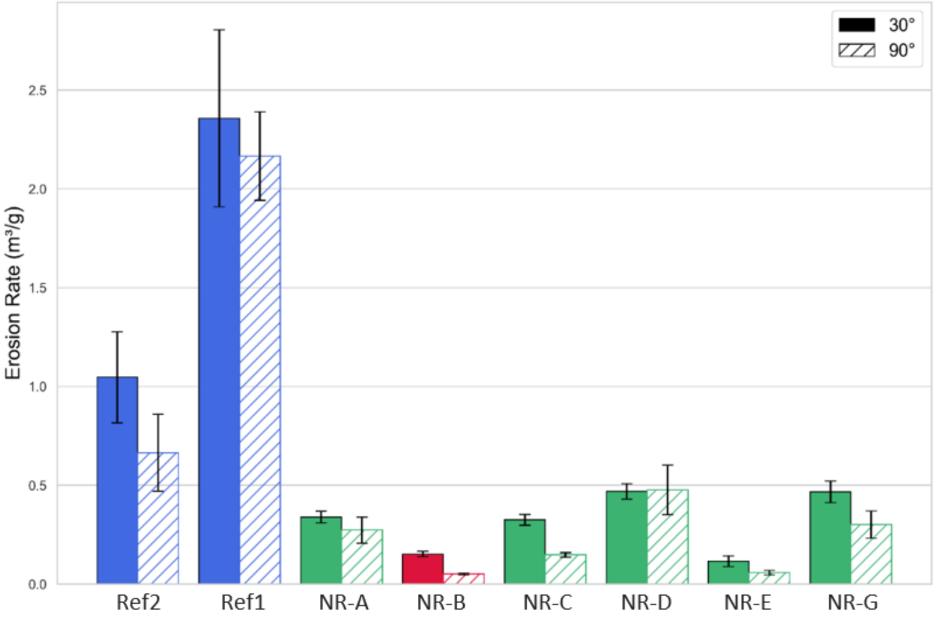

Figure 49. Erosion test results for neat resin samples in 30-degree and 90-degree angles (SOD=10mm).

Among all neat resins, neat resin B, with an approximate density of 1.14 g/cm³, was identified as the best-performing neat resin in the thermoset category and subsequently underwent further tribology testing due to its favorable erosion properties.

Looking at Figure 49, all the neat resins performed better at normal angles, showing lower erosion rates at a 90° angle compared to higher erosion rates at oblique (30°) angles, indicating behavior similar to ductile erosion. Neat Resin B demonstrated the lowest erosion rate among the tested samples, despite having the lowest hardness compared to the others, which is contrary to typical expectations where harder materials perform better against wear. This behavior can be explained by the resin's ability to effectively absorb and dissipate impact energy. It has a greater capacity for plastic deformation, meaning the epoxy can deform under impact, spreading the energy over a larger area rather than allowing it to concentrate at a point, thereby reducing material removal. Additionally, harder materials can be more brittle and susceptible to fracture under stress, so the epoxy's softer nature minimizes the risk of such fractures.

Based on the observations of the samples at normal angles after erosion tests, we noticed that some erodent particles became embedded in the material. Furthermore, since the impact velocity is considered moderate, both observations align with the mechanism of multiple plastic deformations described in Figure 3 (Mechanism c), indicating that this is the dominant mechanism.

3.2 Abradability (Pin-on-Flat Tribometer) Test Results

The results of the coefficient of friction over 5000 cycles of the pin-on-flat tribology test for commercially used polymeric samples, ref1 and ref2, along with a selected neat epoxy resin sample (Epon 828, Epikure 3164), are presented in Figure 50.

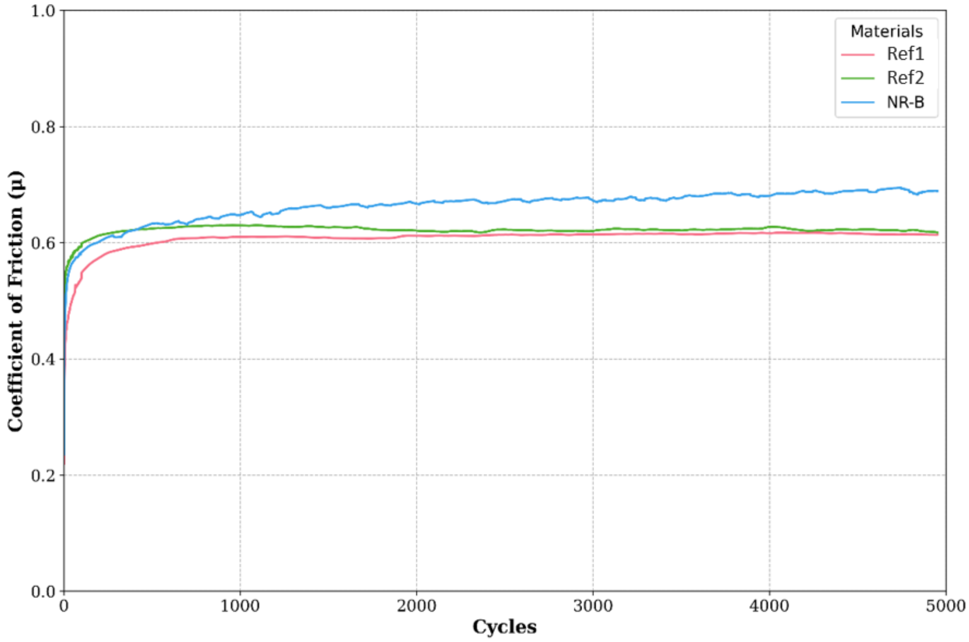

Figure 50. Tribology test results: Coefficient of friction for neat resin B (Epon 828, Epikure 3164) compared with commercial polymer materials at 1Hz and 5N load,

In the results from the pin-on-flat tribology test, the materials ref1, ref2, and the selected neat epoxy resin all show an initial increase in the coefficient of friction, which quickly stabilizes as the materials reach a consistent state of wear. Throughout the test, the coefficient of friction (CoF) was observed to stabilize. This stabilization of friction values for the samples is documented in Table 10. Notably, the epoxy resin exhibited a low coefficient of friction, comparable to that of the commercial polymer samples.

Table 10. The results of the coefficients of friction for NR-B and reference materials after pin-on-flat test

Sample Code	Main Components	μ
Ref1	Reference Material	0.61
Ref2	Reference Material	0.62
NR-B	Selected Epoxy Sample	0.68

The results from the confocal microscopy analysis of samples after the tribology test are presented in Figure 51.

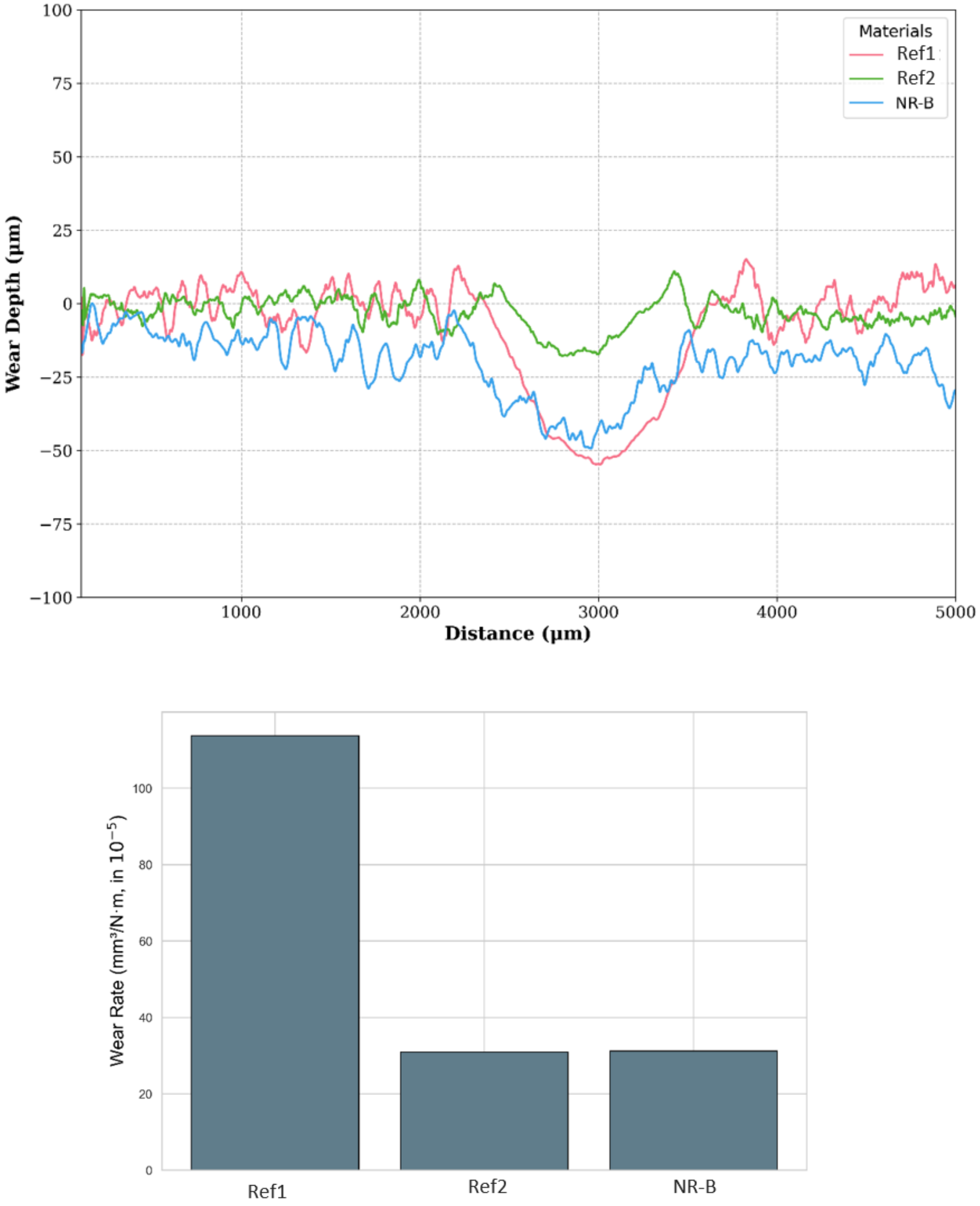

Figure 51. Wear track results, and wear rate results, after pin-on-flat tribology test using confocal microscope, for the best neat resin (NR-B: Epon 828, Epikure 3164) along with polymeric references.

Figure 51 presents the wear track depths for the selected neat resin (NR-B) alongside reference materials, showing a comparable level of material removal across these samples. In the wear depth graph, ref1 exhibits a higher wear volume, measured by a confocal microscope, at approximately 50 µm, while the wear depth for the neat epoxy resin sample (NR-B) is around 45 µm. Additionally, the wear rate results in Figure 51 reveal that ref1 has a higher wear rate at (113 mm^3/N.m, in 10^{-5}), whereas ref2 demonstrates a substantially lower wear rate at 31 mm^3/N.m, in

10^{-5}. NR-B displays a wear rate closely matching that of ref2 at 30 $mm^3/N.m$, in 10^{-5}, indicating similar wear resistance.

3.3 Hardness (Shore D)

The results of hardness test for neat resins are presented in Figure 52.

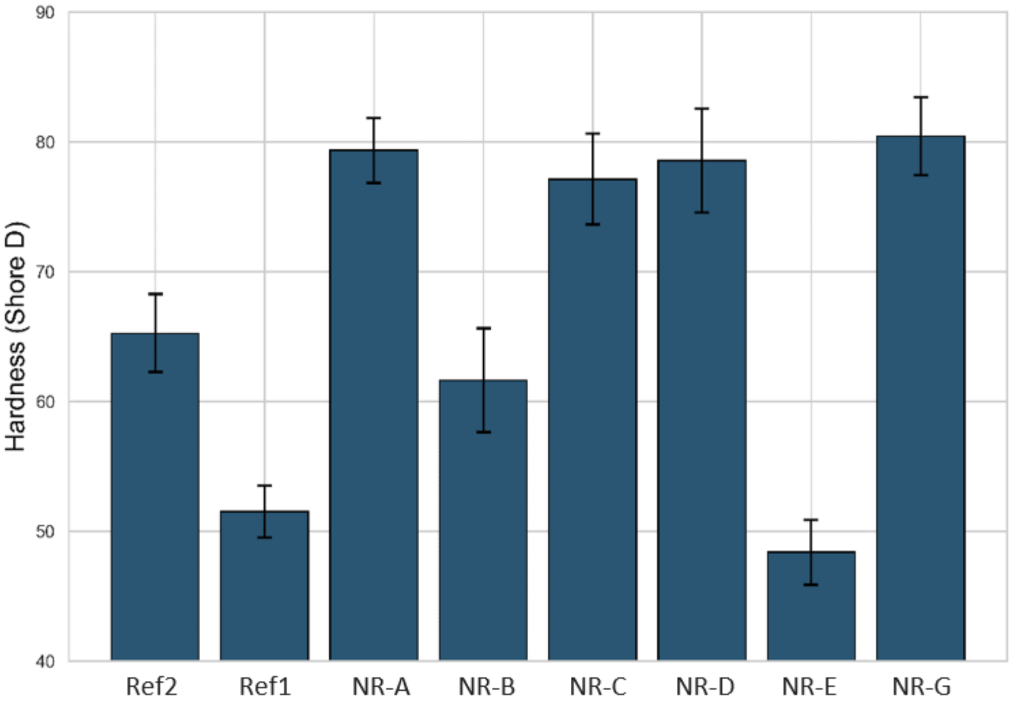

Figure 52. Hardness test Results using Shore Durometers, for neat resins.

Hardness measurements for the neat resin samples were conducted using Shore Durometers (Type D). The results reveal that, except for neat resin E, all neat resin samples exhibit higher Shore D hardness values than the reference materials, ref1 and ref2, which have hardness values of 51 and 65, respectively. Specifically, neat resin B is measured at approximately 61 Shore D.

The environmental temperature and material hardness significantly influence the wear characteristics of these materials. Although the direct relationship between hardness and erosion performance has not been thoroughly explored, it is generally observed that materials with lower Shore D hardness are softer and more flexible. This flexibility allows the materials to better absorb and dissipate energy from impacting particles during erosion through elastic deformation. As the material deforms elastically, it tends to minimize the amount of material lost during the erosion process. Conversely, harder materials are more likely to crack or chip, which can lead to higher erosion rates.

Chapter 4

Fillers Optimization

4. Fillers Optimization

Seven fillers, graphite, silicone powder, PTFE powder, carbon nanotubes (CNT), milled carbon fiber, aramid fiber, and hollow glass microspheres (HGM), were utilized, each selected for its reinforcement or lubrication properties. Additionally, HGM was used to introduce porosity, mirroring the high porosity found in the reference samples. For each filler, two levels of weight percentage were chosen to evaluate their effects on the material properties as presented in Table 11.

Table 11. Fillers utilized and their concentration levels for sample preparation

Fillers	Role	Levels (VF %)	
		Nea	
		Lower Concentration	Higher concentration
Graphite	Lubricant	0.5 wt%*	1 wt%*
Silicone Powder	Lubricant	5	10
PTFE Powder	Lubricant	10	20
CNT	Reinforcement	0.1 wt%*	0.3 wt%*
Milled Carbon Fiber	Reinforcement	10	30
Aramid Fiber (Kevlar)	Reinforcement	10	20
HGM	Porosity/impact	30	60

4.1 Erosion Test Results

The erosion test results for polymeric reference materials and thermoset composite materials (epoxy with fillers), which include two concentrations of fillers (level 1 and level 2), at 30-degree and 90-degree angles, are depicted in Figure 53 and Figure 54. The materials tested for erosion are detailed in Table 12 and Table 13, where each sample is listed with its corresponding code and material composition.

Table 12. Filler samples tested (level 1), their codes and materials.

Sample Code	Material
Ref1	Reference Material
Ref2	Reference Material
NR	Neat Resin C (Epon 828, Epikure 3274)
NR-CNT 0.1	Neat Resin + Carbon Nano Tubes 0.1wt%
NR-MC 10	Neat Resin + Milled Carbon Fiber 10Vf%
NR-Gr 0.5	Neat Resin + Graphite 0.5wf%
NR-Kev 10	Neat Resin + Aramid Fiber 0.5Vf%
NR-Si 5	Neat Resin + Silicone Powder 5Vf%
NR-PTFE 10	Neat Resin + PolyTetraFluoroEthylene Powder 10Vf%
NR-HGM 30	Neat Resin + Hollow Glass Microspheres 10Vf%

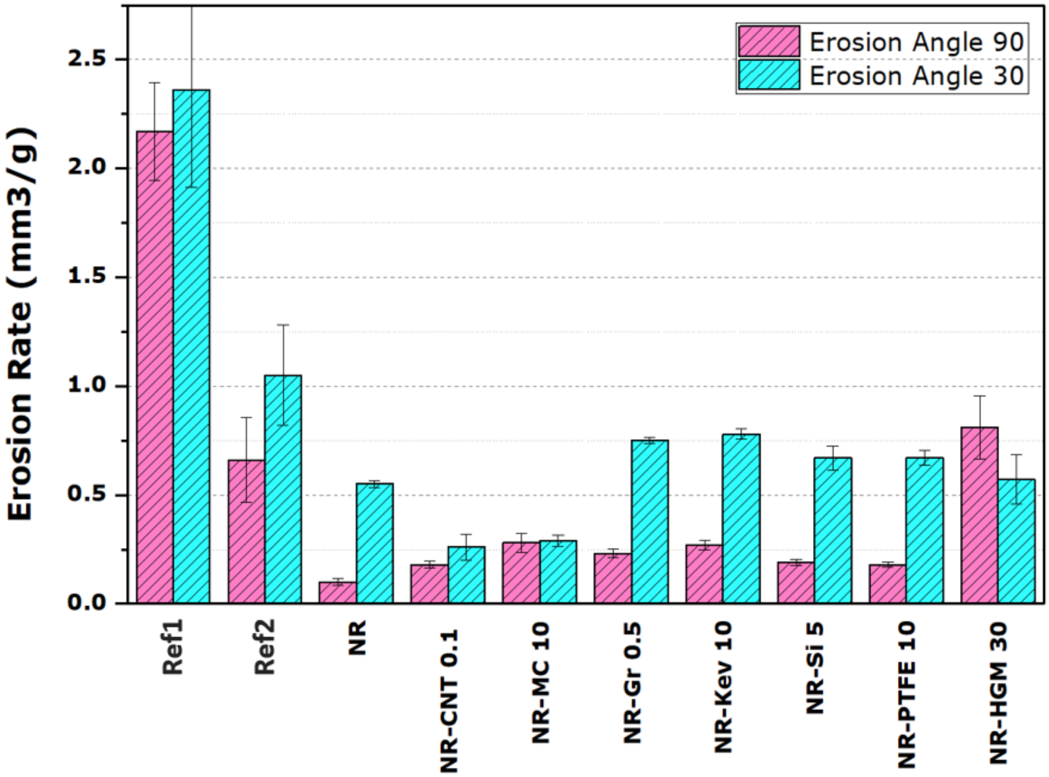

Figure 53. Erosion test results for polymeric reference materials (ref1, ref2), neat resin C, and composite samples for level 1 concentration of fillers, in 30-degree and 90-degree angles (SOD=25mm).

Table 13. Filler samples tested (level 2), their codes and materials.

Sample Code	Material
Ref1	Reference Material
Ref2	Reference Material
NR	Neat Resin C (Epon 828, Epikure 3274)
NR-CNT 0.3	Neat Resin + Carbon Nano Tubes 0.3wt%
NR-MC 30	Neat Resin + Milled Carbon Fiber 30Vf%
NR-Gr 1	Neat Resin + Graphite 1wf%
NR-Kev 20	Neat Resin + Aramid Fiber 20Vf%
NR-Si 10	Neat Resin + Silicone Powder 10Vf%
NR-PTFE 20	Neat Resin + PolyTetraFluoroEthylene Powder 20Vf%
NR-HGM 60	Neat Resin + Hollow Glass Microspheres 60Vf%

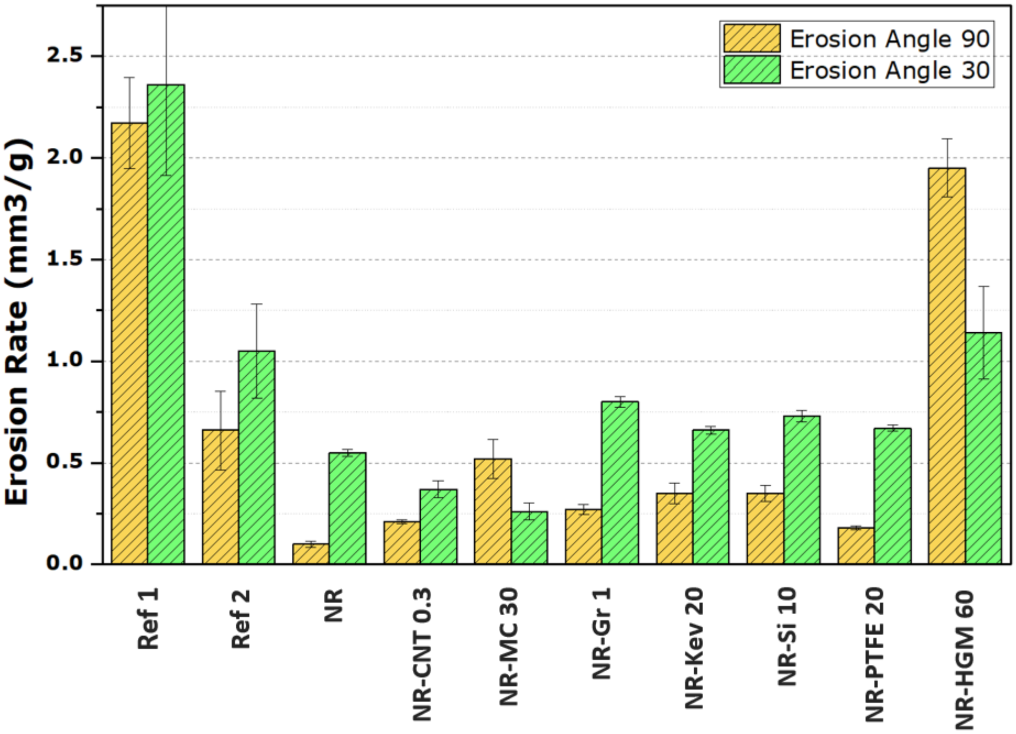

Figure 54. Erosion test results for polymeric reference materials (ref1, ref2), neat resin C, and composite samples for level 2 concentration of fillers, in 30-degree and 90-degree angles (SOD=25mm).

For nearly all the materials tested, the erosion rate at the 30° angle is consistently higher than at the 90° angle, indicating that these materials are more vulnerable to erosion when impacted at an angle.

Incorporating Carbon Nanotubes (CNT) and Milled Carbon (MC) enhances the erosion performance at 30° angles compared to neat resin. Conversely, the addition of graphite (Gr), Kevlar pulp (Kev), and silicone powder (Si) results in increased erosion rates, which negatively affects the compound's erosion performance. The inclusion of PTFE does not markedly change erosion performance. Comparatively, level 1 concentrations (lower concentration of fillers) typically show better erosion performance than level 2. Figure 53 illustrates that the NR-CNT0.1 sample, containing carbon nanotubes, exhibit the lowest erosion rates among the materials tested at 30° angles.

4.2 Fillers samples Abradability (Pin-on-Flat) Test

The outcomes of the pin-on-flat tests for polymeric reference samples, specifically ref1 and ref2, along with filler composite specimens at two different filler concentrations—level 1 and level 2—are presented in Figure 55 and Figure 56. These figures offer a comparative analysis of the wear characteristics of each sample under the specified test conditions. Additionally, Table 14and Table 15 display the results of the coefficients of friction derived from these experiments.

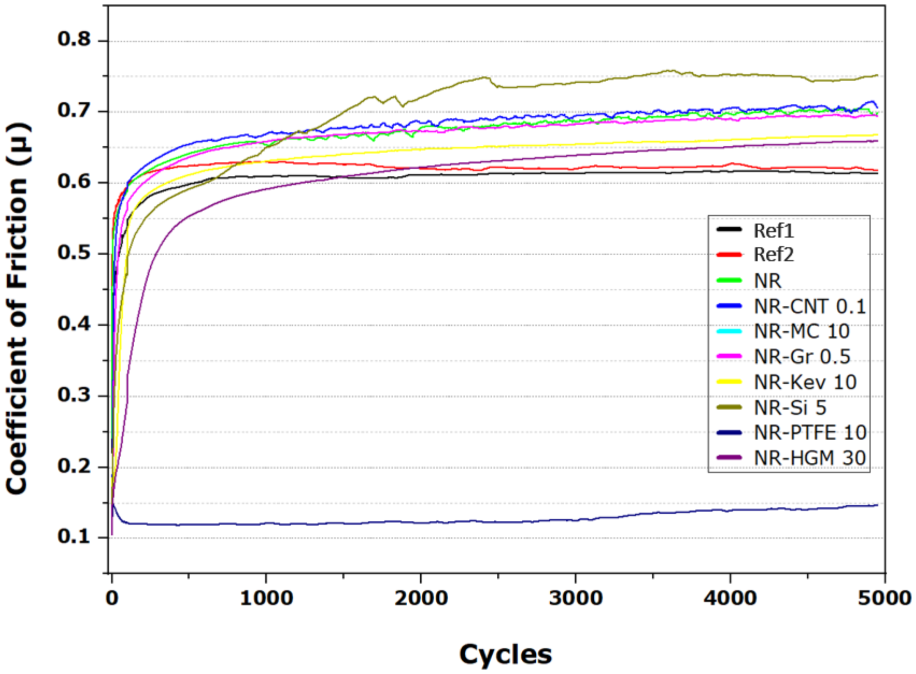

Figure 55. Pin on flat test results for polymeric commercially available samples (ref1 and ref2) and selected composite samples for level 1 concentration of fillers.

Table 14. The results of the coefficients of friction of level 1 filler samples

Sample Code		*μ*
Ref1	Reference Material	0.61
Ref2	Reference Material	0.62
NR	Neat Resin C (Epon 828, Epikure 3274)	0.70
NR-CNT 0.1	Neat Resin + Carbon Nano Tubes 0.1wt%	0.70
NR-MC 10	Neat Resin + Milled Carbon Fiber 10Vf%	0.58
NR-Gr 0.5	Neat Resin + Graphite 0.5wf%	0.69
NR-Kev 10	Neat Resin + Aramid Fiber 0.5Vf%	0.66
NR-Si 5	Neat Resin + Silicone Powder 5Vf%	0.74
NR-PTFE 10	Neat Resin + PolyTetraFluoroEthylene Powder 10Vf%	0.14
NR-HGM 30	Neat Resin + Hollow Glass Microspheres 10Vf%	0.65

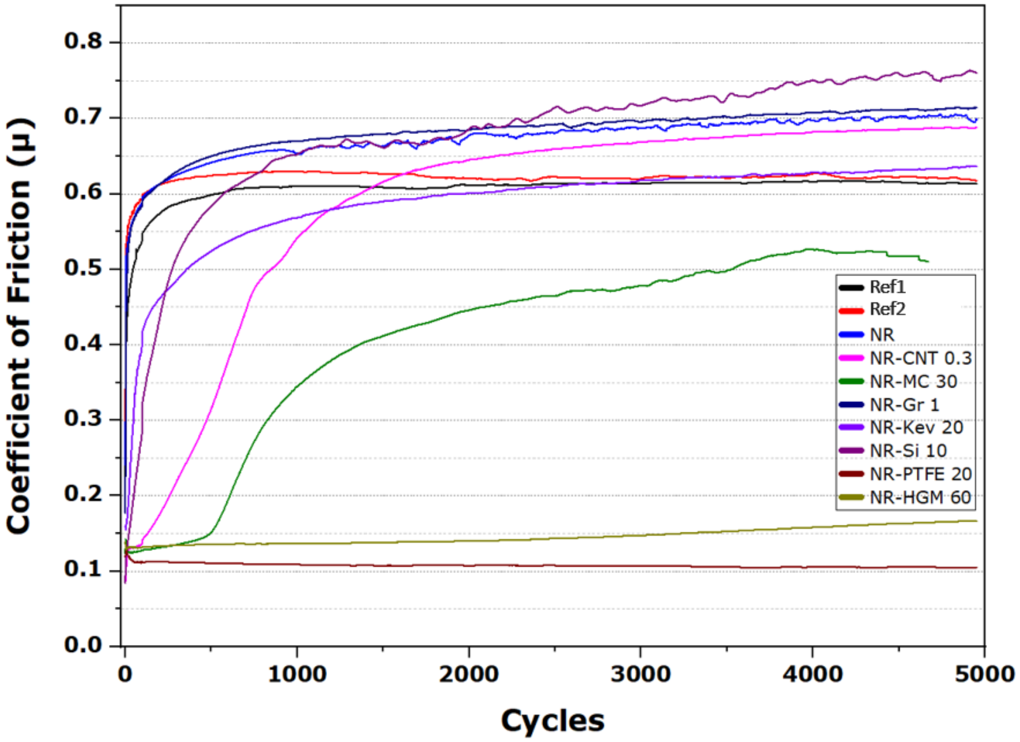

Figure 56. Pin on flat test results for polymeric commercially available samples (ref1 and ref2) and selected composite samples for level 2 concentration of fillers.

Table 15. The results of the coefficients of friction of level 2 samples.

Sample Code		μ
Ref1	Reference Material	0.61
Ref2	Reference Material	0.62
NR	Neat Resin C (Epon 828, Epikure 3274)	0.70
NR-CNT 0.3	Neat Resin + Carbon Nano Tubes 0.3wt%	0.68
NR-MC 30	Neat Resin + Milled Carbon Fiber 30Vf%	0.51
NR-Gr 1	Neat Resin + Graphite 1wf%	0.71
NR-Kev 20	Neat Resin + Aramid Fiber 20Vf%	0.63
NR-Si 10	Neat Resin + Silicone Powder 10Vf%	0.75
NR-PTFE 20	Neat Resin + PolyTetraFluoroEthylene Powder 20Vf%	0.11
NR-HGM 60	Neat Resin + Hollow Glass Microspheres 60Vf%	0.16

For samples containing carbon nanotubes, the frictional behavior remains similar between the two levels, in Figure 55 (NR-CNT 0.1), the coefficient of friction starts at approximately 0.70, similar to the neat resin, and stabilizes throughout the test. In contrast, Figure 56 (NR-CNT 0.3) shows the friction coefficient beginning at a slightly lower value of 0.68, but it trends upwards over time, reaching around 0.72.

The NR-MC samples demonstrate improvement in frictional behavior with an increase in filler concentration. In Figure 55 (NR-MC 10), the coefficient of friction is approximately 0.58, relatively low and stable. In Figure 56 (NR-MC 30), this value drops further to about 0.51, but not stable. These results suggest that milled carbon fibers might be beneficial in enhancing the composite's abradability.

Graphite-enhanced samples show consistent frictional behavior across both concentration levels. In Figure 55 (NR-Gr 0.5), the coefficient of friction is about 0.69, while in Figure 56 (NR-Gr 1), it remains close to 0.71. The consistent friction behavior suggests that increasing graphite concentration does not significantly change the tribological performance of the composite, indicating graphite's benefits may lie more in thermal management or lubrication rather than directly reducing friction.

Kevlar-enhanced samples exhibit noticeable differences in frictional behavior between the two concentration levels. In Figure 55 (NR-Kev 10), the coefficient of friction is around 0.66 and remains relatively stable. However, in Figure 56 (NR-Kev 20), the friction coefficient starts at 0.63 but increases to about 0.75 over time. This pattern suggests that while Kevlar provides favorable initial performance, its not effective in reducing friction at higher concentrations, potentially due to fiber breakdown or increased roughness with prolonged wear.

Silicone powder displays the highest coefficient of friction among the tested composites. In Figure 56 (NR-Si 10), the friction coefficient starts at a much lower value of 0.12 but then rapidly increases to about 0.6. This steep rise indicates that while silicone powder offers excellent initial lubricity, its effectiveness significantly diminishes over time, particularly at higher concentrations.

The PTFE-enhanced samples show the most significant reduction in friction across both levels. In Figure 55 (NR-PTFE 10), the coefficient of friction is about 0.14, already low. In Figure 56 (NR-PTFE 20), it drops further to approximately 0.11 and remains stable throughout the test, underscoring PTFE's exceptional lubricating properties and its ability to sustain low friction.

Hollow glass microspheres exhibit not much change in friction across both levels. In Figure 55 (NR-HGM 30), the coefficient of friction is around 0.65, while in Figure 56 (NR-HGM 60), it slightly decreases to about 0.16. This reduction suggests that higher concentrations of hollow glass microspheres contribute to lower friction, though the effect is less pronounced compared to fillers like PTFE.

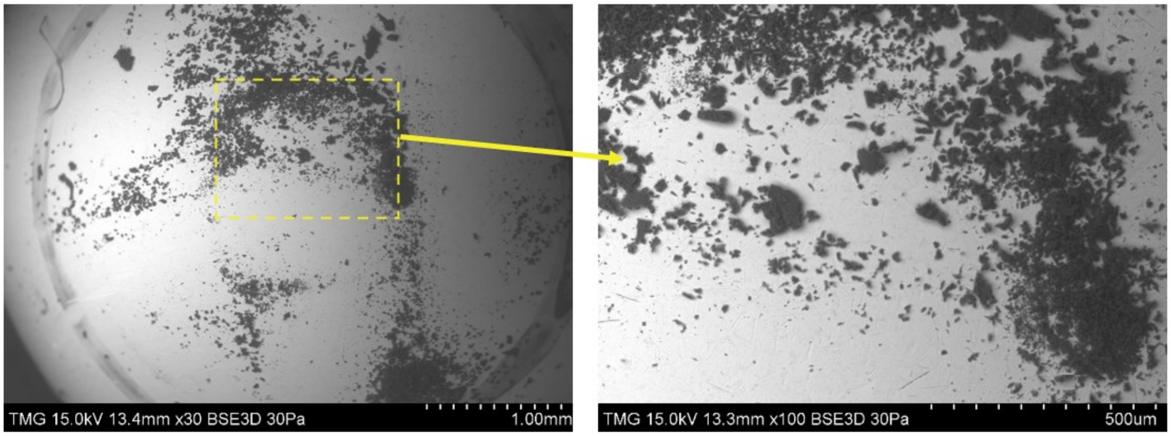

Figure 57. SEM images of the ball used in the pin-on-flat test for the NR-C sample.

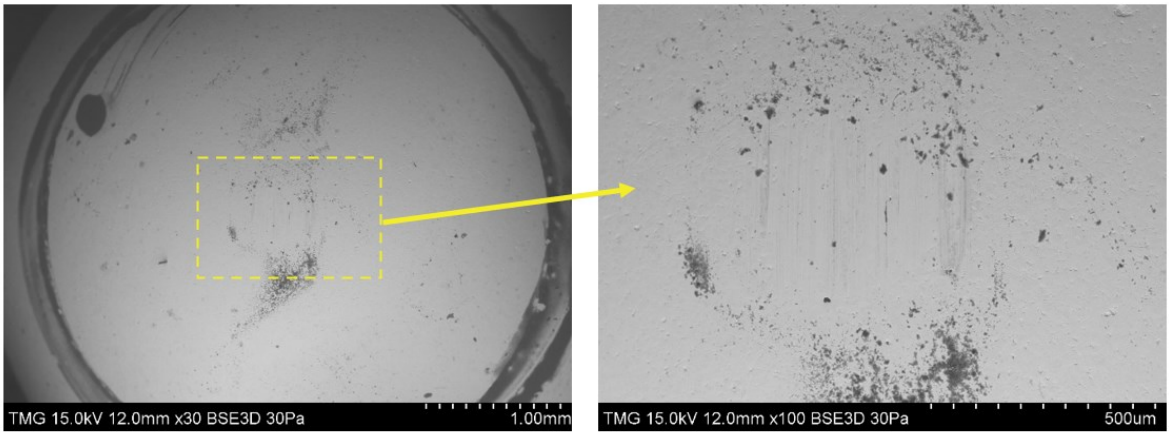

Figure 58. SEM images of the ball used in the pin-on-flat test for the 30% HGM sample.

In Figure 57 and Figure 58, the titanium balls used in the pin-on-flat test for samples of neat resin and resin with 30% HGM were observed under SEM. The images show that the balls tested with neat resin exhibit few scratches but considerable debris. Conversely, the balls tested with the HGM-containing sample display many scratches but less debris. This difference may be attributed to the fact that neat resin, being softer and stickier, undergoes more adhesive wear, leading to material transfer to the titanium ball. In contrast, the addition of HGM increases the composite's hardness, making it more resistant to adhesive wear but more susceptible to abrasive wear, as indicated by the increased scratch marks on the ball used in the test. The higher coefficient of friction (COF) observed with the neat resin is likely due to more direct contact with the titanium ball, resulting in increased friction. This adhesive interaction requires more force to slide the ball over the resin. Meanwhile, the inclusion of HGM reduces the overall stickiness of the resin, resulting in a smoother sliding surface.

Chapter 5

Thermoplastic Selection

5. Thermoplastic Selection

For selecting the most suitable thermoplastic material, erosion testing will be conducted on all thermoplastic samples. The best-performing samples from the erosion test will undergo a pin-on-flat abradability test. The final decision on selecting thermoplastic candidates will be based on the results of these two tests, thus ensuring that the chosen material excels in both erosion resistance and abradability.

Four neat thermoplastic samples were fabricated and evaluated to assess their erosion and pin-on-flat performance. They include Ultra-High Molecular Weight Polyethylene (UHMWPE), Polyphenylene Sulfide (PPS), Polyetherimide (PEI), and Polyetheretherketone (PEEK).

In addition to these, three distinct groups of commercially available products were also acquired for testing. The first group includes engineered thermoplastic compounds purchased from RTP Company. These compounds are referred to as RTP-A, RTP-B, RTP-C, RTP-D, and RTP-E, and their compositions listed in Table 16. They were manufactured using injection molding techniques. The second group comprised samples from Stratasys Company, produced through 3D printing and labeled as 3D-A, 3D-B, and 3D-C listed in Table 17. The third group consisted of silicone rubber samples SR-A, SR-B, SR-C, SR-D, SR-E, and SR-F were obtained from McMaster Carr listed in Table 18. Both erosion tests and pin-on-flat tests were conducted on all these samples to compare their performance.

5.1 Thermoplastic Erosion Test

To compare the erosion behavior of thermoplastic samples, four samples were characterized: (UHMWPE), (PPS), (PEI), and (PEEK). The samples were manufactured using compression molding at COALIA and PEEK sample at Concordia. Figure 59 shows the erosion test results for thermoplastic samples in 30-degree and 90-degree angles compared to reference materials.

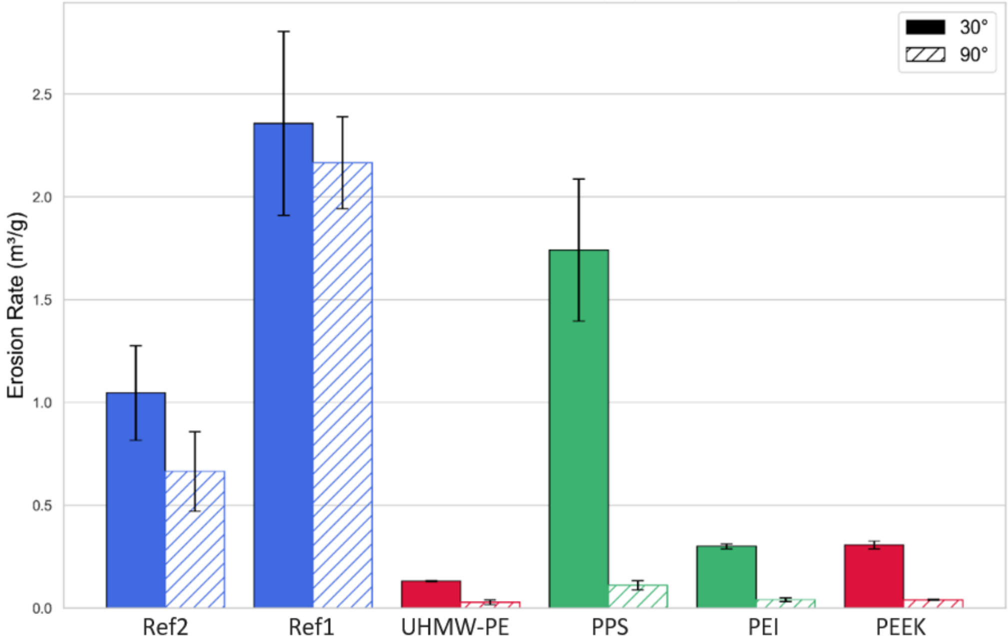

Figure 59. Erosion test results for neat thermoplastic samples in 30-degree and 90-degree angles (SOD=25mm).

The results from the erosion tests show that all materials experienced higher erosion rates at a 30° angle compared to a 90° angle. Notably, the ref1 sample had the highest erosion rate, indicating it has the least erosion resistance among the materials tested. In contrast, PEEK and UHMWPE displayed the lowest erosion rates at both tested angles, suggesting they possess superior erosion resistance. This quality makes them particularly beneficial for coating applications where erosion resistance is critical. Therefore, among all the thermoplastic samples tested, PEEK and UHMWPE were selected as the most suitable candidates for further evaluation and use.

Figure 60, Figure 62, and Figure 64 represent erosion test samples for the RTP samples, 3D-printed samples, and silicone rubber samples at 30-degree and 90-degree angles. The erosion results for the RTP samples, 3D-printed samples, silicone rubber samples, and their selected samples from each group are presented subsequently in Figure 61, Figure 63, Figure 65, and Figure 66 respectively. Five samples from RTP are listed in Table 16.

Table 16. Of-the-shelf thermoplastic compounds from RTP company with their materials and compositions

Code	Material	Main Components
RTP-A	RTP 200 AR 15 TFE 15 SI 2	Nylon 6/6 +AR,PTFE,Si
RTP-B	RTP2299x-120345	PEEK + CF,Gr,PTFE
RTP-C	RTP 200 A ABR	Nylon 6 +Abrasion Resistant
RTP-D	RTP 4000 AT	PPA+ Impact Modified
RTP-E	RTP 4083 AR10 TFE 15 SI 2	PPA+ CF,AR,PTFE,Si

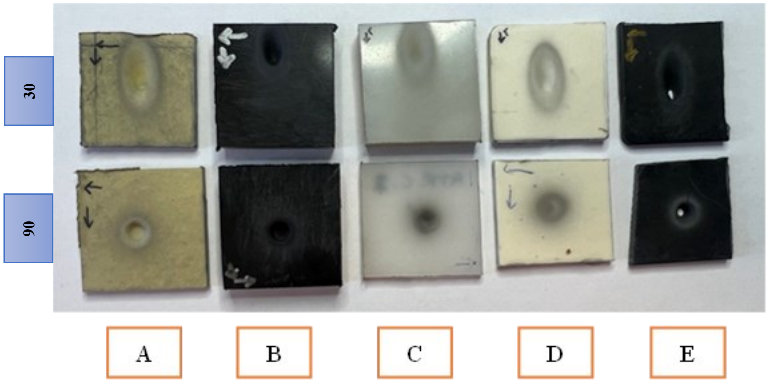

Figure 60. Erosion test samples of RTP at 30° and 90° angles.

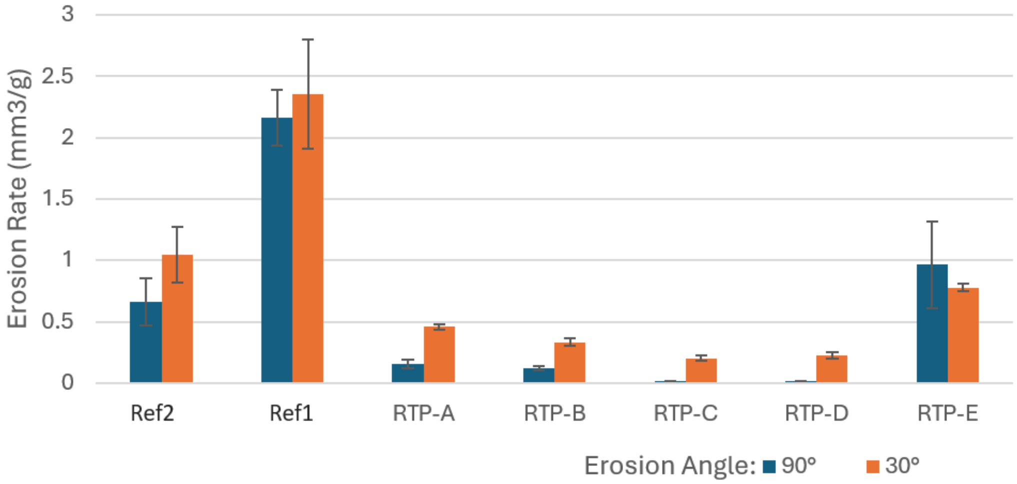

Figure 61. Erosion test results for RTP samples at 30° and 90° angles (SOD=25mm).

The diagram illustrates a comparison of the erosion rates of various RTP compound materials against the polymeric reference materials, ref1 and ref2. The reference materials exhibit a relatively high erosion rate at a 30-degree angle, which notably decreases when measured at a 90-degree angle. Among the RTP compounds, RTP-A and RTP-B show significantly lower erosion rates at both angles, indicating they have superior erosion resistance compared to references.

RTP-C and RTP-D stand out with lowest erosion rates among the RTP compounds. The data clearly suggests that the RTP compounds, especially RTP-C and RTP-D, offer more effective erosion resistance than the reference materials. The angle of impact plays a crucial role in their performance, with different materials showing varying resistance depending on the angle of erosion testing. This highlights the importance of considering the angle of impact in the design and selection of materials for erosion-prone applications. Three samples fabricated using a 3D printing method are presented in Table 17.

Table 17. Of-the-shelf 3D printed thermoplastic compounds with their materials and compositions

Code	Material	Main Components
3D-A	Antero 840 CN03	PEKK + CNT
3D-B	Ultem 9085	PEI (polyetherimide)
3D-C	Ultem 1010	PEI (polyetherimide)

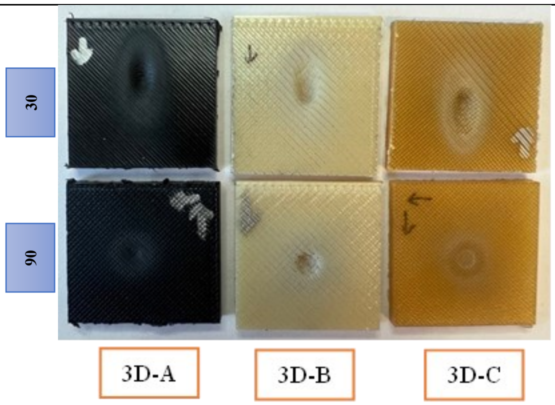

Figure 62. Erosion test samples for the 3D-printed samples at 30° and 90° angles.

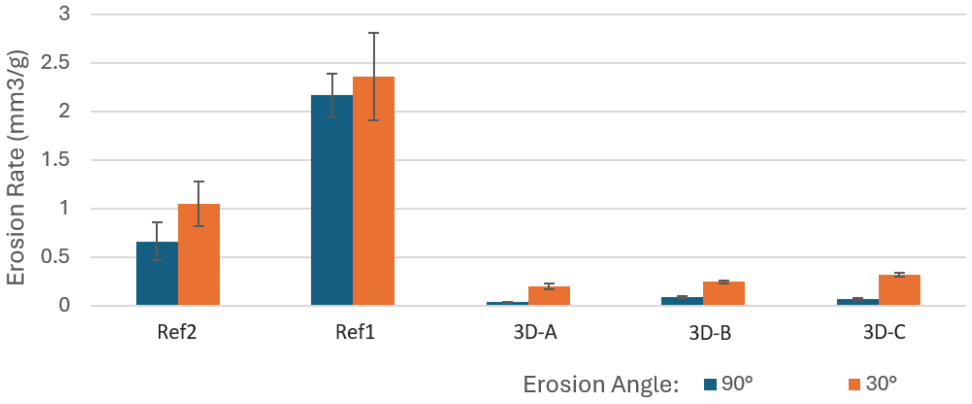

Figure 63. Erosion test results for 3D printed samples at 30° and 90° angles (SOD=25mm).

The erosion test results for the 3D printed materials, when compared to the reference materials, ref1 and ref2, demonstrate that all 3D samples exhibit excellent erosion resistance. The erosion rate is higher at the 30-degree angle for all materials and lower at the 90-degree angle. Among the 3D printed samples, 3D-A stands out by offering the best erosion resistance, showing significantly lower erosion rates than other samples including references. Table 14 Shows the silicon rubber samples considered for this project.

Table 18. Of-the-shelf silicone samples with their hardness.

Code	Material
SR-A	Silicone rubber hardness: 40a
SR-B	Silicone rubber hardness: 50a
SR-C	Silicone rubber hardness: 60a
SR-D	Silicone rubber hardness: 70a
SR-E	Silicone rubber, High strength
SR-F	Silicone rubber chemical resistant

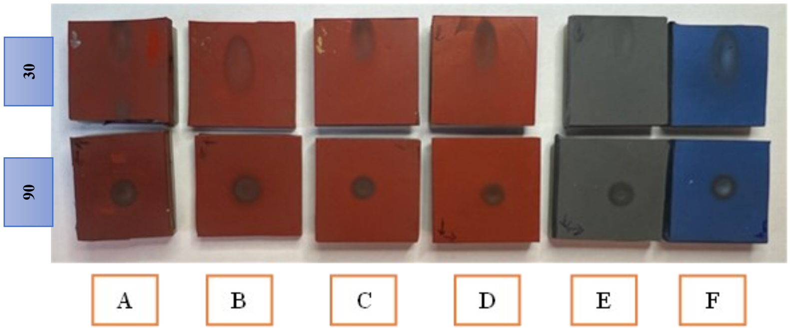

Figure 64. Erosion test samples for the silicone rubber samples at 30° and 90° angles.

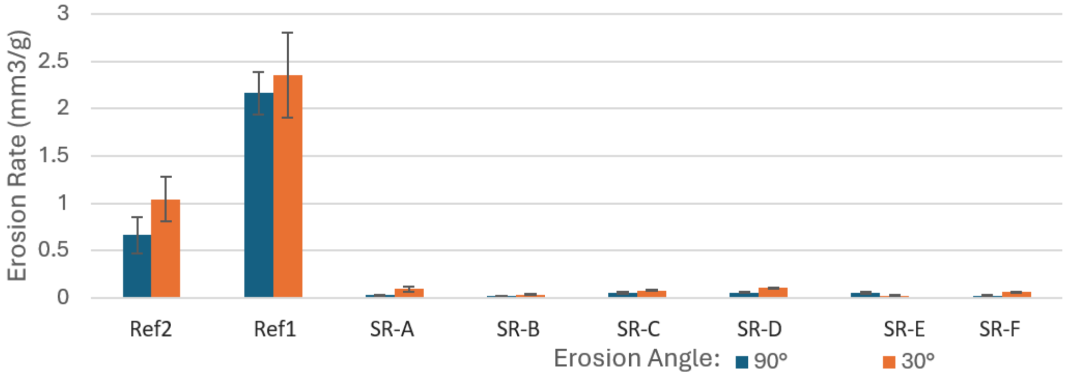

Figure 65. Erosion test results for silicon rubber samples at 30° and 90° angles (SOD=25mm).

The erosion test results for silicone rubber samples (Figure 65) indicate superior resistance compared to the reference materials, across all samples at both angles. Samples SR-B and SR-C have the lowest erosion rates among the silicone rubber samples at both the 30-degree and 90-degree angles, indicating that they offer the best erosion resistance.

Figure 66 shows the erosion test results for selected off-the-shelf Compounds samples in 30-degree and 90-degree angles.

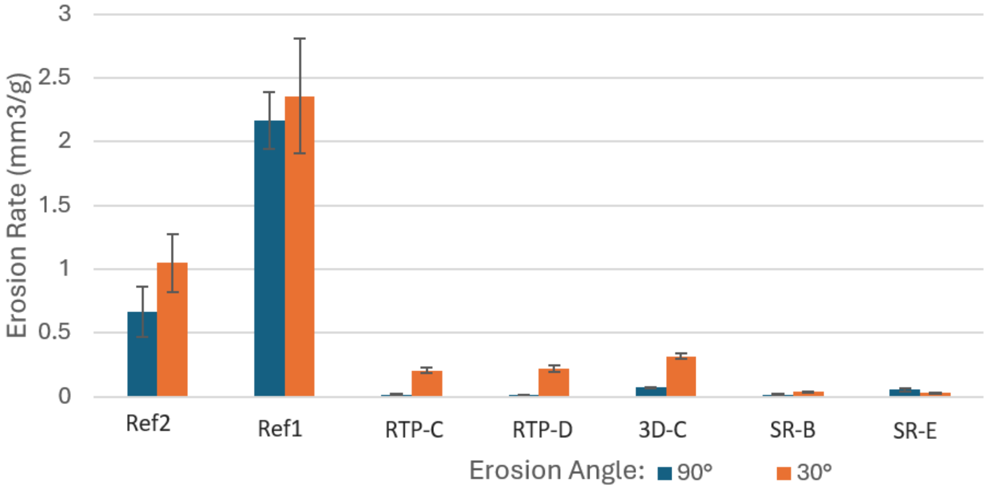

Figure 66. Erosion test results for selected off-the-shelf Compounds samples in 30° and 90° angles (SOD=25mm).

The Figure 66 presents erosion rates for selected thermoplastic compound materials and benchmarks against reference materials. Ref1 and ref2, used as reference materials, exhibit higher erosion rates compared to all. In comparison, RTP-C and RTP-D, along with 3D-C, SR-B, and SR-E, demonstrate significantly lower erosion rates at both tested angles, indicating enhanced erosion resistance. Notably, SR-B and SR-E, which are presumably silicone rubber samples, exhibit the lowest erosion rates among all the materials tested. This suggests that SR-B and SR-E possess the highest erosion resistance, making them particularly suitable for applications where reducing material degradation due to erosive forces is critical.

5.2 Thermoplastic Abradability (Pin-on-Flat) Test

PEEK and UHMW-PE were selected as the top-performing neat thermoplastic materials in terms of erosion resistance. To further validate their performance, a pin-on-flat test was conducted on these samples. The results of the coefficient of friction, obtained from these tests, are presented alongside polymeric reference samples, namely ref1 and ref2. The findings are presented in Figure 67.

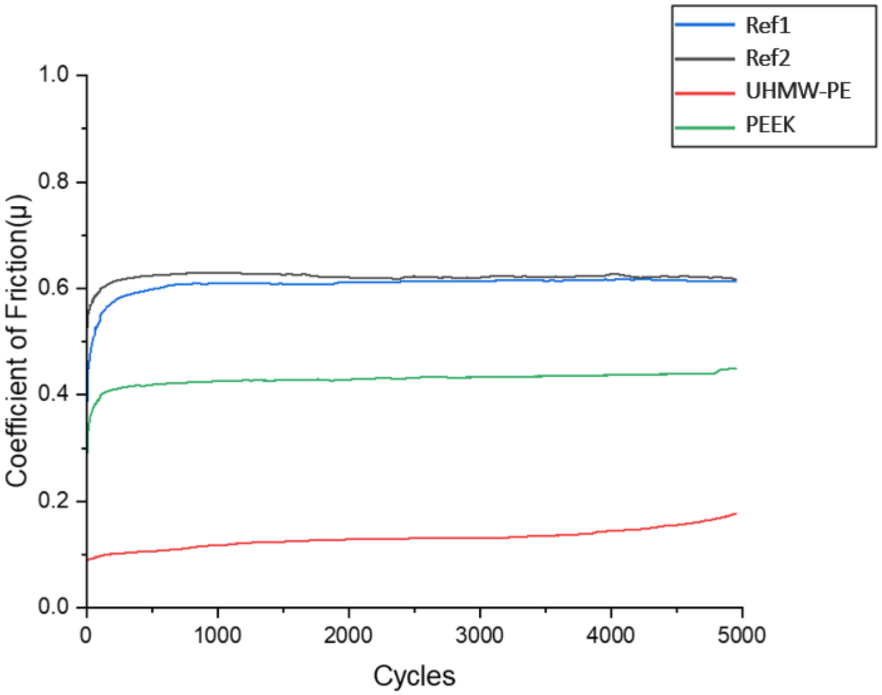

Figure 67. COF results after Pin-on-flat test for polymeric reference (ref1 and ref2) and top selected neat thermoplastic samples, 1Hz and 5N.

Ref2 begins with the highest coefficient of friction, which quickly stabilizes. Ref1 has a slightly lower friction coefficient that also stabilizes rapidly. PEEK starts with a consistently low coefficient of friction, suggesting minimal wear and stable frictional properties. UHMW PE displays the lowest coefficient of friction throughout the cycles, indicating excellent wear resistance and minimal frictional interaction. The coefficients of friction for all materials stabilize early in the cycling, demonstrating that they adapt quickly to the wear conditions and maintain consistent performance over extended periods.

For use as an abradable coating at temperatures around 90°C, PEEK is significantly more suitable than HMWPE. PEEK's superior chemical resistance and stability at elevated temperatures, coupled with its high Tg (143°C), make it an excellent choice for maintaining performance in demanding environments. HMWPE, while beneficial for its properties at lower temperatures and in specific applications, is likely to face challenges due to its lower Tg (-125°C to -100°C) and, making it less ideal for high-temperature abradable coating applications. Table 19 displays the results of the coefficients of friction from the experiments after stabilizing.

Table 19. The results of the COF of selected neat thermoplastic materials Vs. reference materials

Sample Code	Material	Main Components	*μ*
Ref1	-	Reference Material	0.61
Ref2	-	Reference Material	0.62
PEEK	PEEK	Neat PEEK	0.42
UHMW-PE	Ultra-High Molecular Weight Polyethylene	Polyethylene	0.16

Ref1 and ref2, both reference materials, exhibit similar coefficients of friction, measuring 0.61 and 0.62 respectively. PEEK, a neat form of polyether ether ketone, shows a moderate coefficient of 0.42, while UHMW-PE, an ultra-high molecular weight polyethylene, presents the lowest coefficient among the materials tested at 0.16, indicative of its very low friction properties.

In addition to the neat thermoplastic materials discussed in the previous chapter, four of-the-shelf thermoplastic compounds were selected for their superior erosion behavior. The results of the coefficient of friction (CoF) during the pin-on-flat test for these samples (RTP-C, RTP-D, SR-B, and SR-E), along with the polymeric reference samples (ref1 and ref2), are presented in Figure 68.

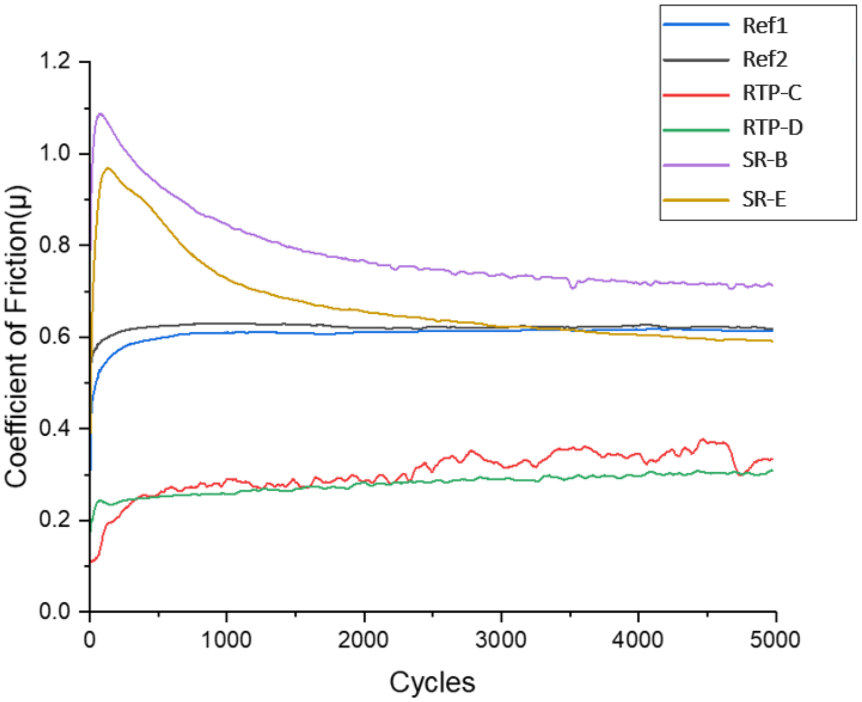

Figure 68. COF results during Pin on flat test for polymeric reference samples (ref1, and ref2) and top selected off-the-shelf thermoplastic compounds (RTP-C, RTP-D, SR-B, and SR-E), 1Hz and 5N.

Ref1 and ref2 show similar CoF patterns. Both RTP-C and RTP-D materials start with lower coefficients of friction and exhibit only a slight decrease, maintaining a relatively stable value throughout the test. SR-B and SR-E maintain the highest and stable coefficients of friction from start to finish, indicating minimal change in their wear characteristics over time. Table 20 shows the results of the coefficients of friction extracted from the experiments.

Table 20. The results of the coefficients of friction for selected off-the-shelf materials

Sample Code	Material	Main Components	μ
Ref1	-	Reference Material	0.61
Ref2	-	Reference Material	0.62
RTP-C	RTP 200 A ABR	Nylon 6 +Abrasion Resistant	0.16
RTP-D	RTP 4000 AT	PPA+ Impact Modified	0.29
SR-B	Hardness: 50A	Silicon Rubber	0.74
SR-E	High Strength	Silicon Rubber	0.60

Ref1 and ref2, both reference materials, show similar coefficients at 0.61 and 0.62 respectively. RTP-C and RTP-D have coefficients of 0.16 and 0.29, highlighting their lower friction properties. SR-B has the highest coefficient at 0.74, while SR-E shows a coefficient of 0.60, slightly less than SR-B but still on the higher side among the materials listed. Based on the coefficient of friction (CoF) results for the thermoplastic samples, UHMW-PE and PEEK were chosen as the best-performing neat thermoplastics, and RTP-D (PPA-Impact modified) was selected from the thermoplastic compound samples.

Chapter 6

Final Candidates

6. Final Candidates

The experimental results presented in this study in thermoset group, highlight the effects of integrating Carbon Nanotubes (CNT) and Polytetrafluoroethylene (PTFE) into Epoxy polymer matrix Epon 828 and Epikure 3164, to improve erosion resistance and reduce friction coefficients. PTFE was selected, due to its low friction properties, for minimizing surface wear, especially under conditions of sliding contact. Based on these findings, a composite sample incorporating both CNT and PTFE was carefully developed to leverage the synergistic effects of these fillers. The sample, designated NR-CNT0.1-PTFE10, contains Epon 828 with Epikure 3164 with 0.1 wt% Carbon Nanotubes and 10 vf% Polytetrafluoroethylene. This blend was made to explore how the combined properties of these fillers could elevate performance beyond what might be achieved individually. The composite with dual fillers underwent testing, including erosion testing at two different angles, pin-on-flat wear assessments, and a thorough investigation during rub-rig test.

In the thermoplastic category of the study, polyetheretherketone (PEEK), ultrahigh molecular weight polyethylene (UHMW-PE), and RTP-D (impact-modified polyphthalamide, or PPA) emerged as the top performers. These materials were notably effective in terms of their erosion resistance and coefficient of friction (COF) during abradability test.

6.1 Thermoset Final Candidate

Based on the erosion and pin-on-flat tests conducted, for thermosets, NR-B resin was selected as the preferred resin for adding fillers to enhance properties among the various resins tested. This selection was influenced by its superior performance in these tests compared to other resins. The addition of fillers is aimed at further improving these qualities, making NR-B an ideal candidate for applications requiring abradability.

Among all the fillers tested, CNT (Carbon Nanotubes) and PTFE (Polytetrafluoroethylene) were selected as the best performers in the erosion and pin-on-flat tests. It is important to note that these fillers were added to the NR-C resin (Epon 828-Epikure 3274) to study the effect of fillers. CNT was found to enhance performance in erosion resistance, while PTFE served as a lubricant to reduce the coefficient of friction. However, subsequent use of CNT in the selected NR-B resin (Epon 828 with Epikure 3164) did not result in significant improvements. This variation might be due to different CNT dispersions in NR-C samples compared to NR-B or their differences in structure. Further studies are necessary to comprehensively understand the effects of different erosion test parameters and the inclusion of CNT.

6.1.1 Thermoset Final Candidate Erosion Test

Figure 69 illustrates the erosion rates of the NR-CNT0.1-PTFE10 composite sample relative to the neat resin B (Epon 828 Epikure 3164) and commercially available samples, ref2 and ref1, under impact angles of 30 and 90 degrees.

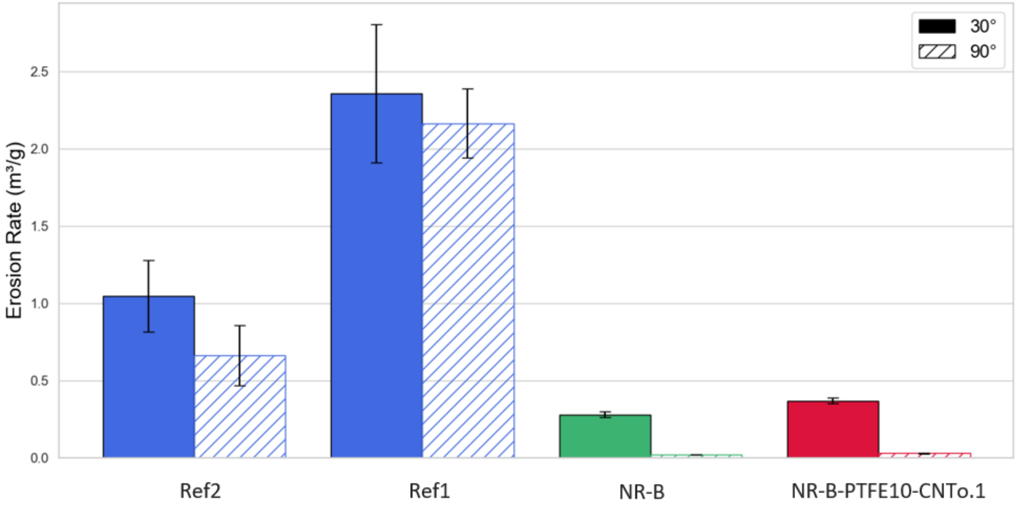

Figure 69. Erosion test results for the NR-CNT0.1-PTFE10 composite sample alongside the neat resin (NR-B) and commercially available samples, ref1 and ref2, in 30-degree and 90-degree angles (SOD=25mm).

The results presented in Figure 69 indicate that the ref1 sample exhibited the highest erosion rates at both tested angles, followed by the ref2 sample which showed better erosion resistance than ref1 but still underperformed compared to the neat resin and the NR-CNT0.1-PTFE10 composite. The ref1 and ref2 samples were found to have around 60% and 40% HGM, respectively. The highest erosion rate for these commercially available samples can be correlated to their high content of HGM. All samples show a higher rate of erosion at the 30-degree angle, suggesting that they exhibit ductile erosion behavior.

Based on the results, the NR-CNT0.1-PTFE10 composite outperforms the commercially available samples, exhibiting superior erosion resistance. The main erosion mechanism observed for this composite is considered to be plastic deformation, as mentioned in Chapter 3, according to this mechanism, material experience multiple plastic deformations due to repeated particle impacts. This leads to energy absorption through plastic strain, reducing the rate of material removal. However, the neat resin NR-B (Epon 828, Epikure 3164) shows an erosion rate similar to that of the NR-CNT0.1-PTFE10 composite. This indicates that incorporating carbon nanotubes (CNT) and polytetrafluoroethylene (PTFE) into the NR-B resin matrix does not enhance its erosion resistance. This contrasts with the findings for neat resin NR-C (Epon 828, Epikure 3274), where incorporating CNT resulted in a reduction in erosion rate. This discrepancy might be due to differences in the resin structures.

6.1.2 Thermoset Final Candidate Abradability Pin-on-Flat Test

Regarding the evaluation of abradability, the pin-on-flat test was utilized to assess the NR-CNT0.1-PTFE10 composite sample. Figure 70 displays the results of the coefficient of friction during the pin-on-flat tests for this composite, comparing it with the neat resin (NR) and two commercially available polymeric samples, ref1 and ref2. This figure illustrates the relative performance of the composite versus the baseline neat resin and the commercial samples under controlled wear testing conditions, providing a clear visual representation of how each material withstands abrasive wear.

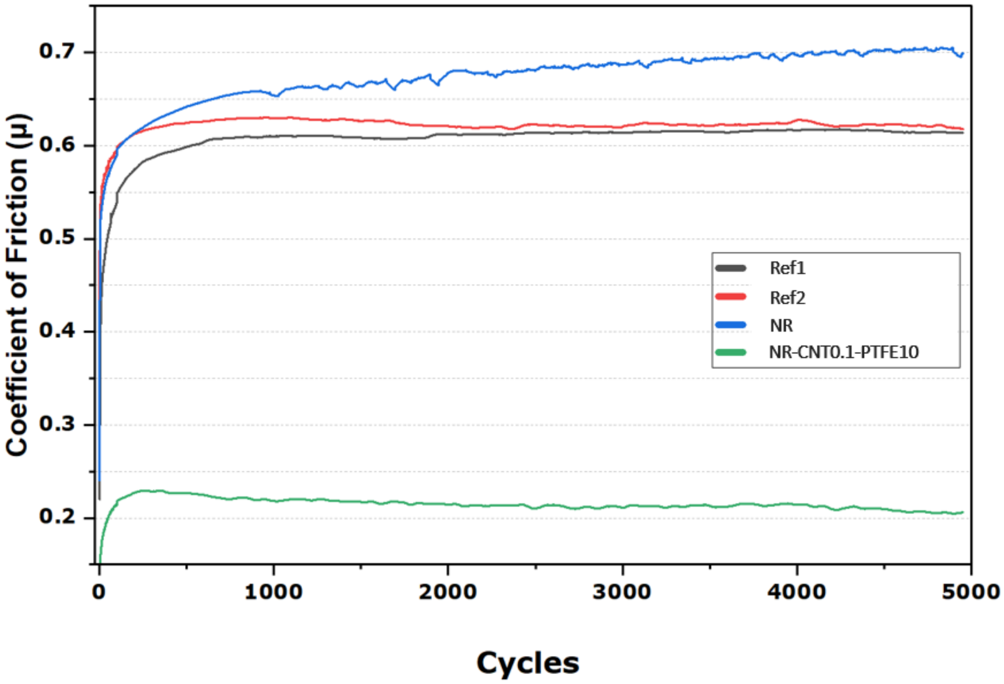

Figure 70. Pin on flat COF test results for NR-CNT0.1-PTFE10 composite sample alongside comparisons with the neat resin (NR) and commercially available samples, ref1 and ref2, 1Hz and 5N.

In the assessment of coefficient of friction, the NR-CNT0.1-PTFE10 composite sample, indicated by the green line, demonstrates a markedly lower and more stable coefficient of friction compared to the neat resin and other commercially available samples. It begins with a coefficient of around 0.18, quickly stabilizes at approximately 0.2, and maintains this level throughout the test duration. This represents a significant improvement over the neat resin (NR), which exhibits a peak friction coefficient of about 0.67, translating to a 70% reduction in friction for the composite sample. Additionally, compared to the ref1 and ref2 samples, which show coefficients of 0.61 and 0.62 respectively, the NR-CNT0.1-PTFE10 sample displays a reduction of roughly 67%. This substantial decrease in friction is attributed to the effect of polytetrafluoroethylene (PTFE), the incorporated filler.

Furthermore, Figure 71 presents the wear depth results from a pin-on-flat test, as analyzed using a confocal LEXT OLS 4100 Olympus microscope. The graph compares the wear performance of the NR-CNT0.1-PTFE10 composite sample to that of the neat resin (NR) and two commercially available polymeric samples, ref1 and ref2. The wear depth, measured in micrometers (μm), is plotted against the distance traversed by the pin, offering a detailed view of each sample's surface wear behavior over a sliding distance of 5000 μm.

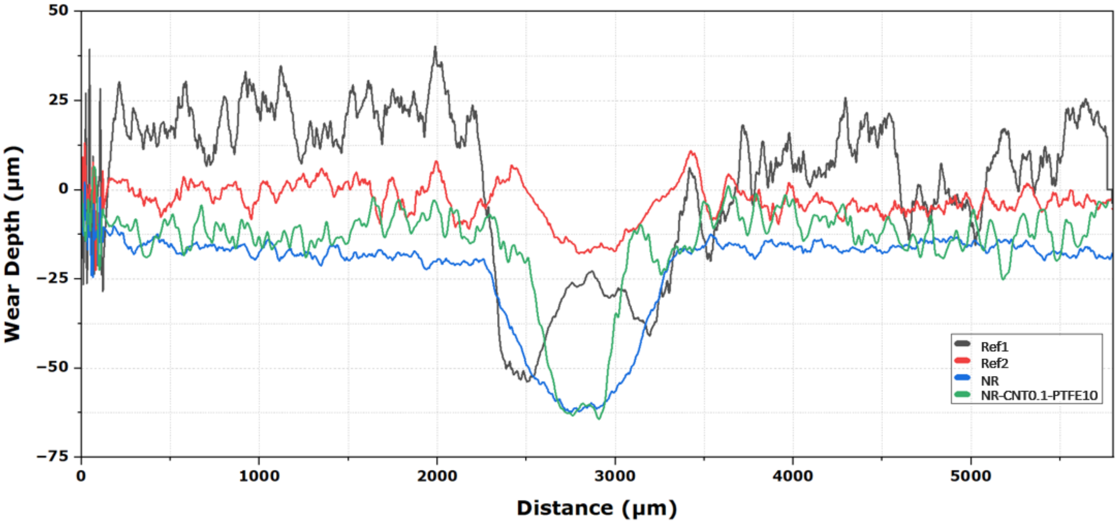

Figure 71. Wear depth results after pin-on-flat test using confocal microscope, for NR-CNT0.1-PTFE10 composite sample alongside comparisons with the neat resin (NR) and commercially available samples, ref1 and ref2.

The wear depth profiles of the tested samples reveal significant differences in their resistance to wear, each indicated by distinct colored lines in the graphical data.

The ref1 sample, represented by the black line, shows notable fluctuations in wear depth due to its transparency under microscope. The deepest wear occurring at around the 3000 μm, reaching approximately 70 μm in depth. This indicates substantial material removal during the test, suggesting low wear resistance for ref1. These characteristics imply that ref1 offer moderate frictional performance, with insufficient wear resistance showing higher abradability.

In contrast, the ref2 sample, depicted by the red line, demonstrates a more stable wear profile, with a peak wear depth of about 20 μm at the 2500 μm point. Despite this, ref2 exhibits higher wear resistance than ref1.

The neat resin (NR), shown with the blue line, shows a maximum depth of about 60 μm, which is modest compared to the commercially available samples. The consistent wear depth across the sliding distance also suggests gradual material loss.

Remarkably, the NR-CNT0.1-PTFE10 composite sample, illustrated wear depth maximum around 60 µm, showing probable higher abradability with lower wear resistance. This reduction in friction and wear prevents the generation of heat and wear debris.

The wear rates of the samples were calculated from $w_s = \frac{\Delta V}{F.d}\left(\frac{\mu m^3}{N.m}\right)$, where $\varDelta V$ is the volume loss in μm^3 (measured from the worn area of cross-section in Figure 71) having the density of each sample using Sartorius YDK01 density kit with distilled water based on ASTM D792. F is the applied load in "*N*" and d is the sliding distance in "m" [41]. The findings are presented in Figure 72.

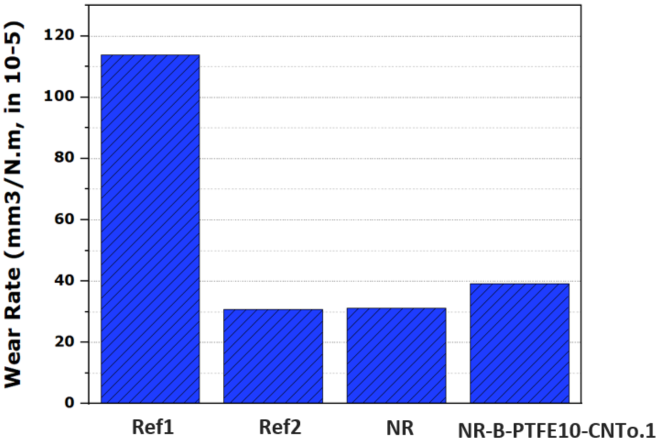

Figure 72. Wear rate results after pin-onflat test using confocal microscope, for NR-CNT0.1-PTFE10 composite sample alongside comparisons with the neat resin (NR) and commercially available samples, ref1 and ref2.

Figure 72 presents the wear rate results from pin-on-flat tests conducted on samples, including the NR-CNT0.1-PTFE10 composite, alongside the neat resin (NR) and commercially available samples, ref1 and ref2. The wear rates, quantified in cubic millimeters per Newton-meter (mm^3/Nm).

The graph illustrates that the ref1 sample exhibits a significantly higher wear rate compared to the other samples, and after that NR-CNT0.1-PTFE10 composite. This performance suggests that the synergistic interaction between CNT, reinforces the material's structural integrity, and PTFE, which reduces surface friction, effectively contributes to a proper wear rate, showing the abradability and durability of the composite under operational stress.

The analysis Scanning Electron Microscope (SEM) images obtained from the pins after the tests offers essential insights into the characteristics of the materials tested, particularly in terms of material transfer and the formation of surface scratches on the ball specimen. These observations are indicators of the underlying wear mechanisms and are valuable for understanding the tribological performance of the materials being studied. SEM images documenting the condition of the ball surfaces after the pin-on-flat tests are presented in Figure 73 through Figure 76.

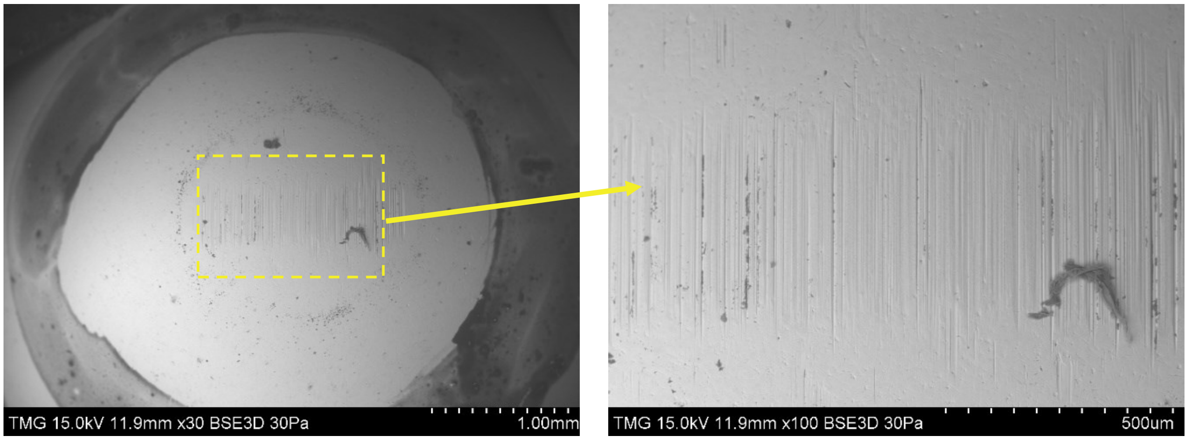

Figure 73. SEM images of the ball used in the pin-on-flat test for the ref1 commercially available sample in different magnifications.

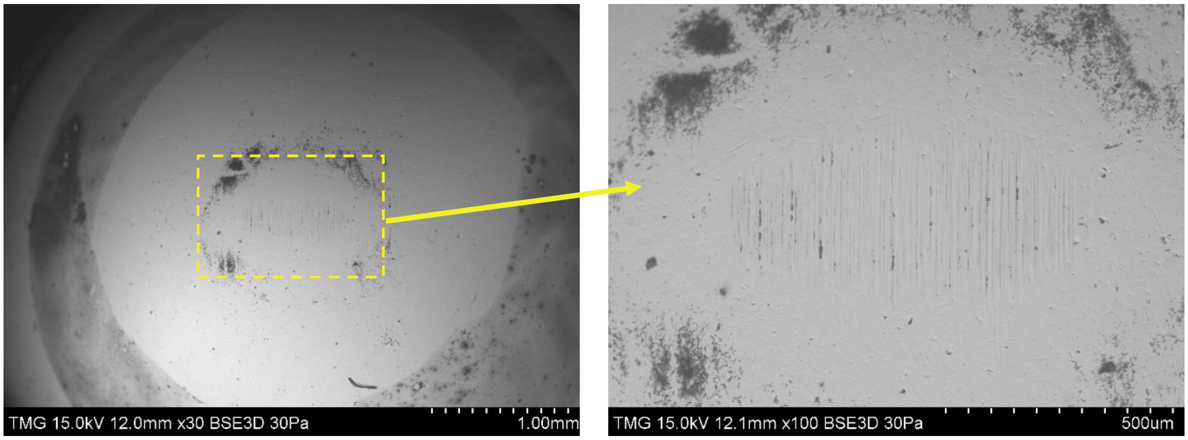

Figure 74. SEM images of the ball used in the pin-on-flat test for the ref2 commercially available sample in different magnifications.

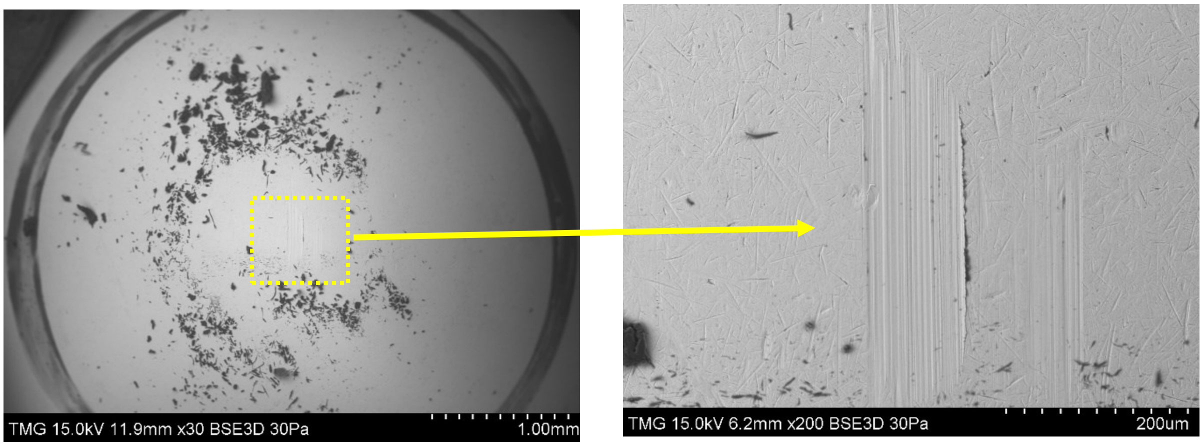

Figure 75. SEM images of the ball used in the pin-on-flat test for the NR-B sample.

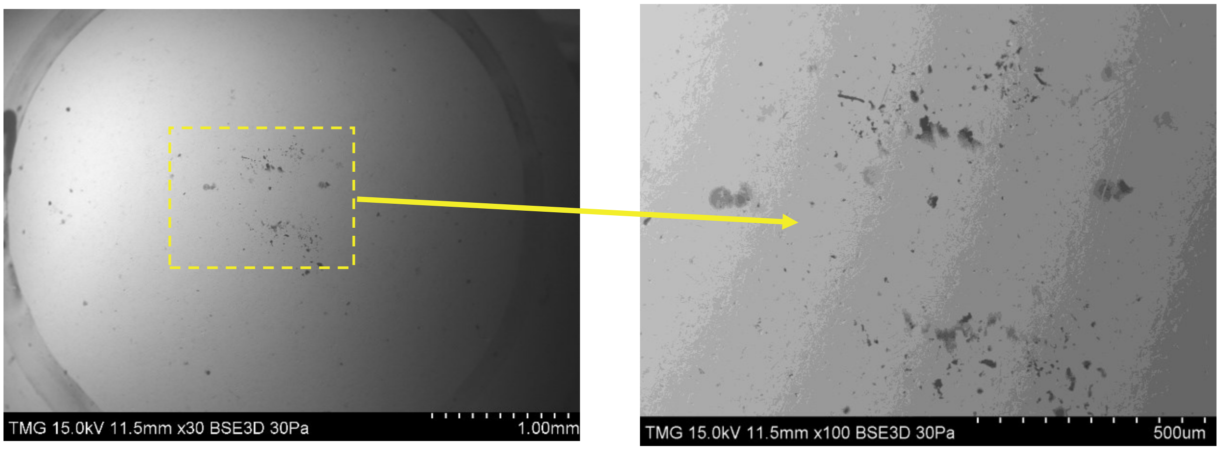

Figure 76. SEM images of the ball used in the pin-on-flat test for the NR-B-CNT0.1-PTFE10 sample.

The SEM analysis reveals that the extent of material adherence to the ball surfaces varies significantly based on the composition of the tested samples. For instance, in commercially available samples like ref1 and ref2, only minimal material transfer occurred, with faint traces of adhered material visible on the ball's surface.

The scratching patterns observed in the SEM images provide additional insights into the wear mechanisms at play. The ref1 and ref2 samples, which exhibited only minor material adherence, showed more pronounced and widespread scratching on the ball surface, suggesting hard HMS or embedded particles on the sliding surfaces scratch the counter face, leading to material removal through micro-cutting. The relatively uniform and directional scratches indicate stable sliding conditions with consistent contact stresses.

The NR sample, with a higher coefficient of friction (0.73), exhibited substantial material transfer and scratching, indicative of severe adhesive wear. In contrast, the addition of CNT and PTFE in the NR-CNT0.1-PTFE10 sample significantly altered the wear behavior, showing much less material adherence and fewer scratches. This improvement can be attributed to the lubricating effects of PTFE and the reinforcing properties of CNTs, which collectively reduce friction and wear, resulting in a smoother and less damaged counter face.

Overall, the interplay between abrasive and adhesive wear processes is complex, as illustrated by the material adherence and scratching patterns on the ball surfaces. Materials like ref1 and ref2 exhibit stable wear behavior characterized by moderate friction and minimal material transfer, typical of abrasive wear. Introducing CNTs and PTFE into the NR-B matrix substantially reduces both material transfer and surface damage. These findings highlight the crucial role of filler selection in optimizing the tribological properties of composite materials for specific applications.

6.1.3 Thermoset Final Candidate Rub Rig Test

The wear track results obtained from the confocal microscopy after the rub-rig test for the final sample NR-CNT0.1-PTFE10 with commercially reference materials are presented in Figure 77 to Figure 79.

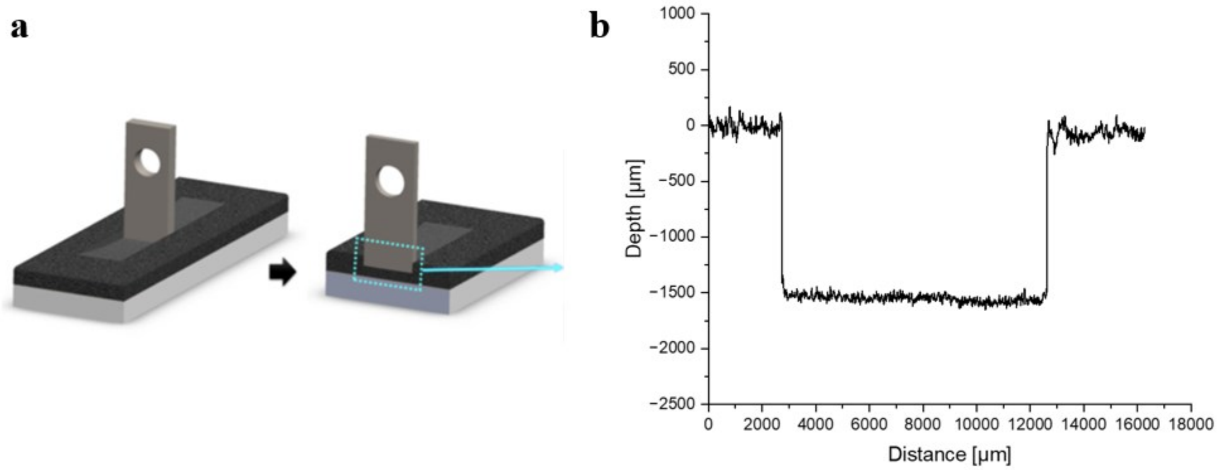

Figure 77. a) Schematic of rub-rig testing wear tracks and blades.[40] **b) Wear track results after rub-rig test using confocal microscope, for the ref2 commercially available sample.**

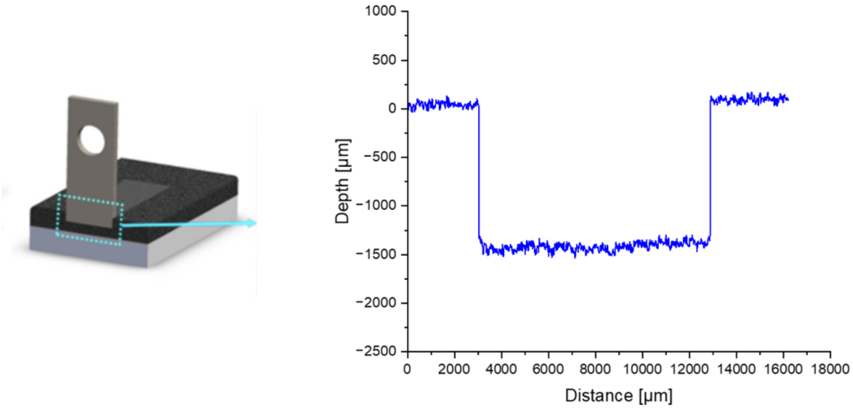

Figure 78. Wear track results after rub-rig test using confocal microscope, for the ref1 commercially available sample.

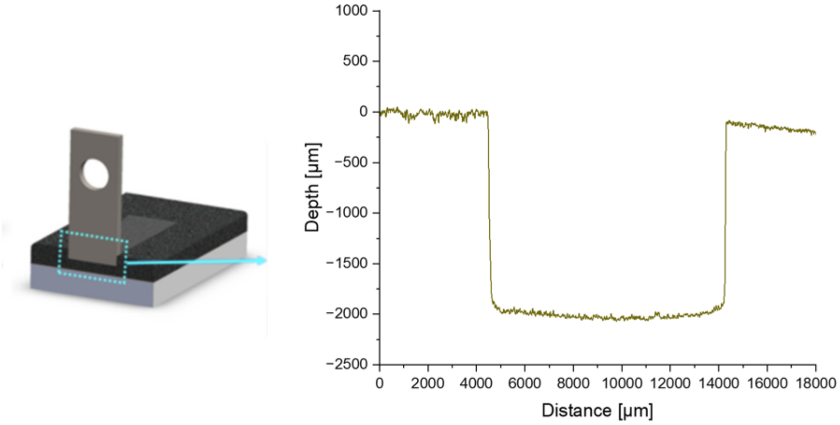

Figure 79. Wear track results after rub-rig test using confocal microscope, for the final thermoset candidate NR-B-CNT0.1-PTFE10 (Epon 828, Epikure 3164 with fillers CNT 0.1% and PTFE 10%).

The confocal microscopy results from the rub-rig test offer detailed insights into the wear characteristics of each sample. Figure 79 shows a very smooth wear track, suggesting that it abrades easily. The smoothness of the surface after testing indicates its abradability, making it suitable for applications where material removal is desired without excessive force.

6.1.3.1 Temperature Results for Thermoset Final Candidate Rub Rig Test

The temperature variations during the rub-rig tests, as recorded by a thermal camera, have been presented in Figure 80 to Figure 82 for the reference materials and final candidates.

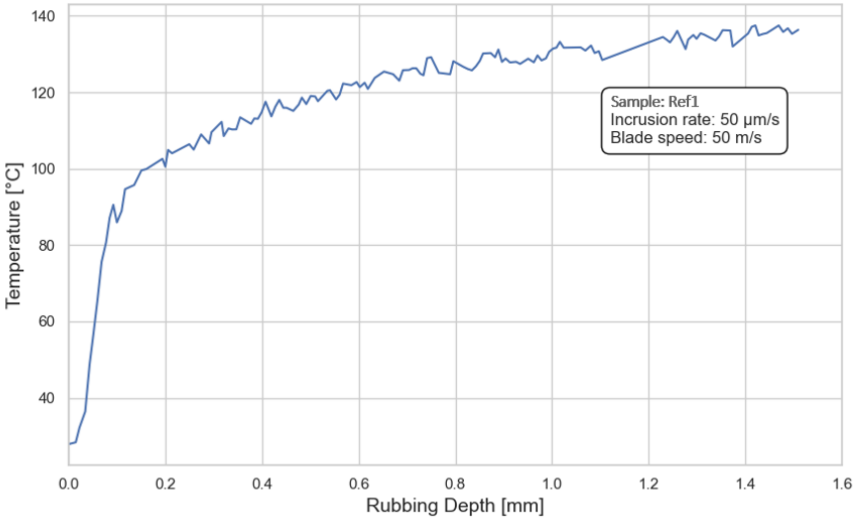

Figure 80.Temperature variation during the rub-rig test, recorded by a thermal camera, for, ref1.

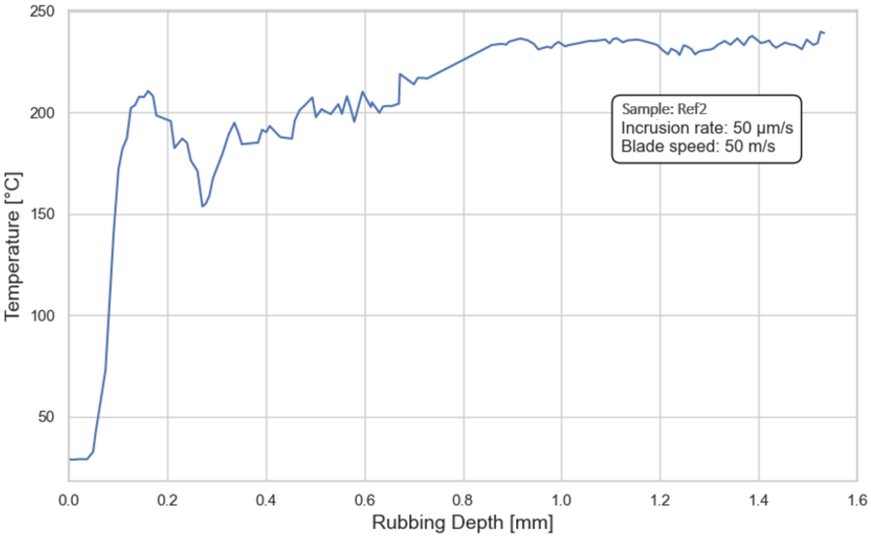

Figure 81. Temperature variation during the rub-rig test, recorded by a thermal camera, for, ref2.

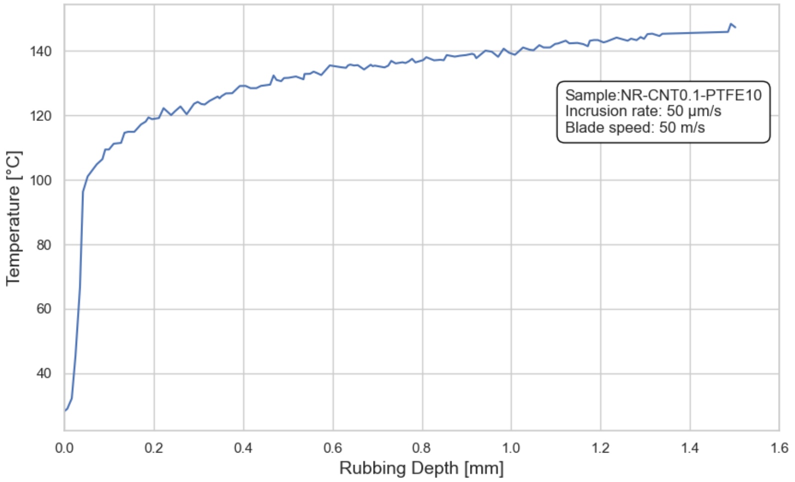

Figure 82. Temperature variation during the rub-rig test, recorded by a thermal camera, for, the final thermoset candidate NR-B-CNT0.1-PTFE10 (Epon 828, Epikure 3164 with fillers CNT 0.1% and PTFE 10).

the NR-B-CNT0.1-PTFE10 (final thermoset candidate) sample, which includes CNT (0.1%) and PTFE (10%), exhibited a maximum temperature of 147°C which is between the maximum temperatures of the two polymeric reference materials.

Since reaching higher temperatures is not desirable for our purposes, and maintaining lower temperatures is preferable, the results indicate that the NR-B-CNT0.1-PTFE10 (final thermoset candidate) sample generates less heat compared to the reference material ref2, making it a potential candidate.

6.1.3.2 SEM/EDS Characterization of Blades after Rub Rig Test, Thermoset Final Candidate

Figure 83 depicts a blade after a rub rig test to highlight the area analyzed in subsequent SEM/EDS images (Figure 84 to Figure 86).

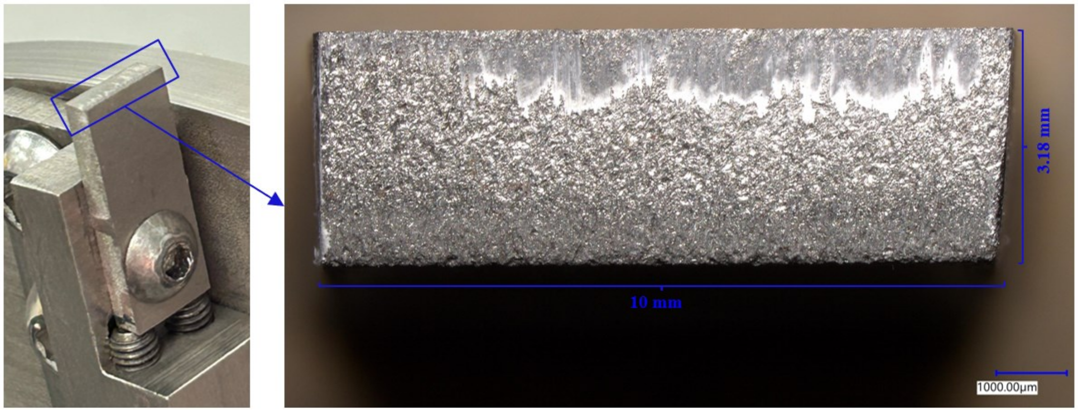

Figure 83. Photo of the blade tip with its dimensions after rub rig test

Figure 84 to Figure 86 show SEM/EDS images of blades from the top view after conducting rub rig tests on references and final thermoset candidate. In these images, the green color indicates the Ti-6Al-4V blades, while the reddish color shows the polymeric material that has adhered to the blades from the tests. These images help us see how much and where the material has stuck to the blades, giving insights into how these materials interact during the test.

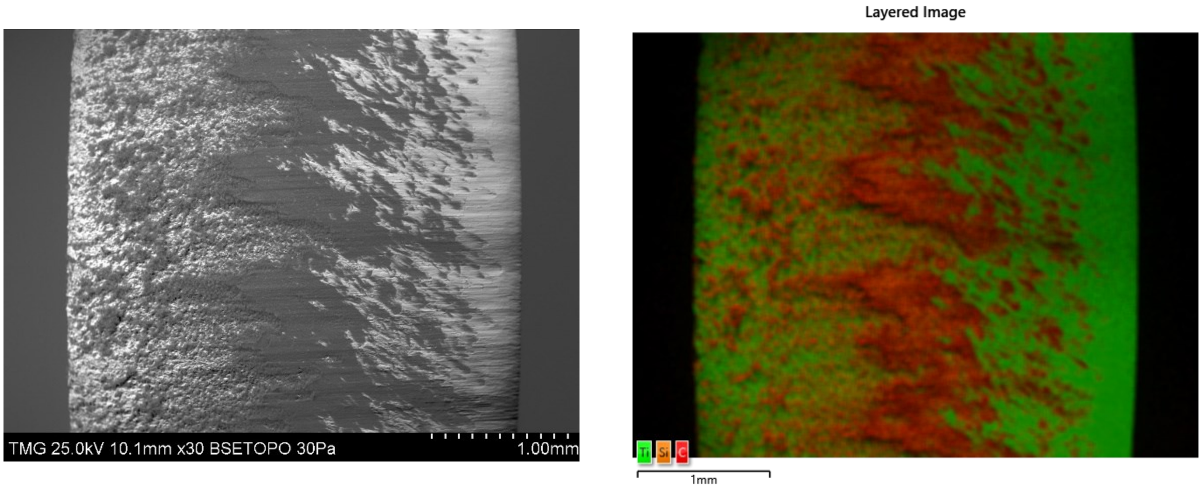

Figure 84. Materials that adhered to the top blade after the rub rig test for reference 2.

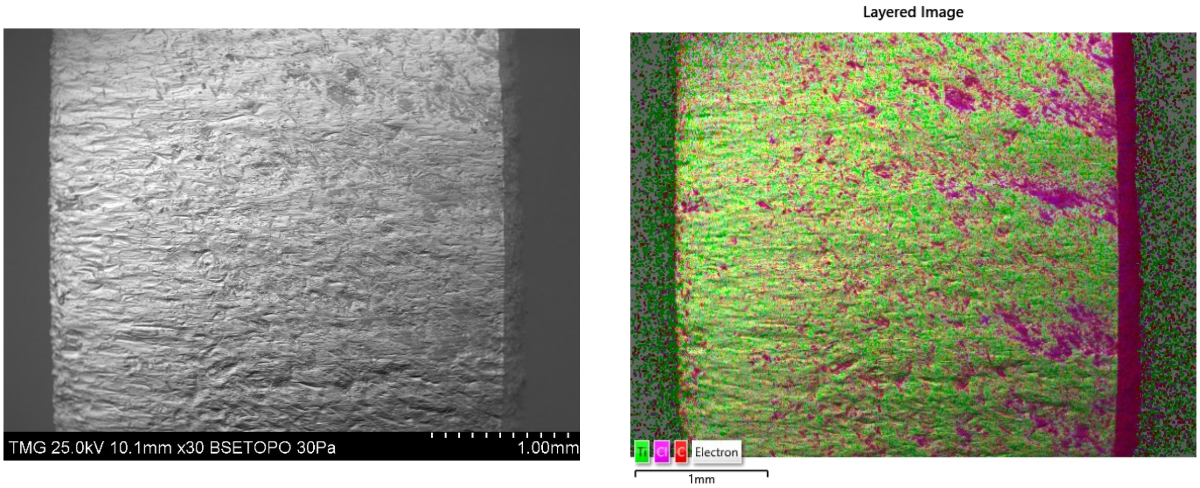

Figure 85. Materials that adhered to the top blade after the rub rig test for reference 1.

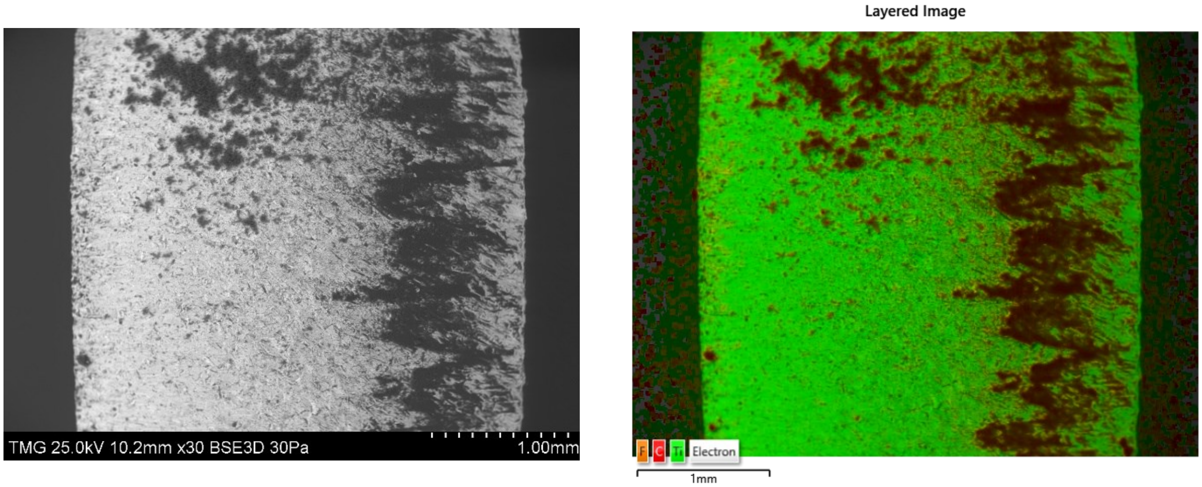

Figure 86. Materials that adhered to the top blade after the rub rig test for sample: NR-B-CNT0.1-PTFE10.

Based on observations of the blades after testing with the ref2 sample in Figure 84, significant adherence of the polymeric material to the Ti-6Al-4V blades was visible. The material adhered appears coarser in texture and large in size.

The SEM image of the blade after the test for ref1 shows a cleaner blade surface with less polymeric material sticking to it. The debris appears finer and more evenly distributed, with minimal coarse particle formation.

For the final thermoset sample, SEM image of the blade shows a moderate adherence of material to the blade, with a mix of fine and coarse particles. The presence of carbon nanotubes and PTFE likely influences the wear characteristics.

6.2 Thermoplastic Final Candidate

Among the neat thermoplastic samples, neat PEEK and neat UHMW-PE emerged as the top-performing materials in our sample set. Additionally, within the thermoplastic compound samples, RTP-D (PPA-impact modified) was identified as the best-performing material based on the results from the erosion and pin-on-flat tests. These findings highlight the superior wear and erosion resistance of these selected materials under the conditions tested.

6.2.1 Erosion Results

The erosion rate results for the three top-selected thermoplastic samples, neat PEEK, neat UHMW-PE, and the compound RTP-D (PPA-impact modified), indicated exceptionally low erosion rates, significantly lower than reference materials tested. These findings are illustrated in Figure 87, emphasizing the superior erosion resistance of these selected thermoplastic materials under test conditions.

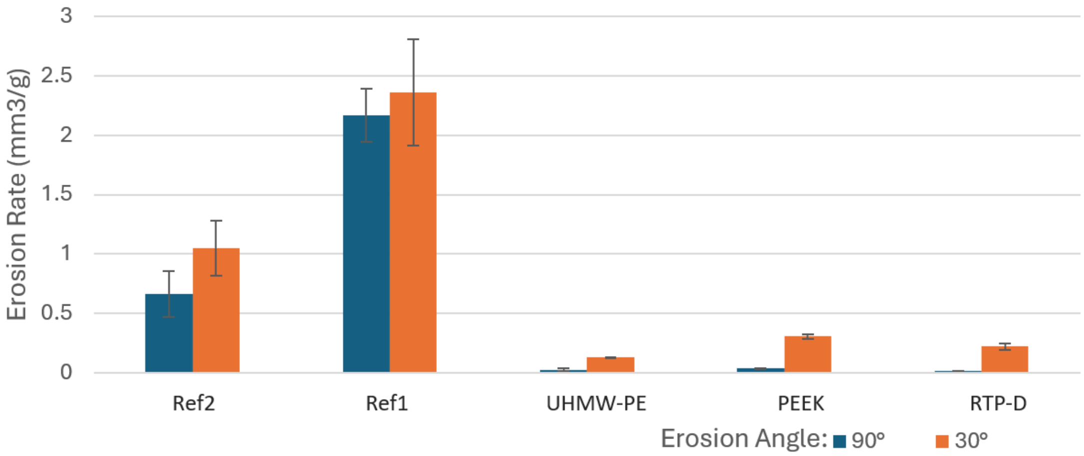

Figure 87. Erosion test results for polymeric reference samples (ref1 and ref2), and thermoplastic final candidate samples, PEEK, UHMW-PE, and RTP-D (PPA-impact modified), in 30-degree and 90-degree angles (SOD=25mm).

6.2.2 Thermoplastic Final Candidate Abradability (Pin-on-Flat Tribometer) Test

The pin-on-flat test was also conducted on selected thermoplastic candidates, and the results for the coefficient of friction (COF) were all better than those of the two polymeric reference materials, ref1 and ref2. These results demonstrate a 1.5 times lower COF for PEEK, 4 times better for the UHMW-PE sample, and 2 times lower COF for the RTP-D (PPA-impact modified) sample. (Figure 88)

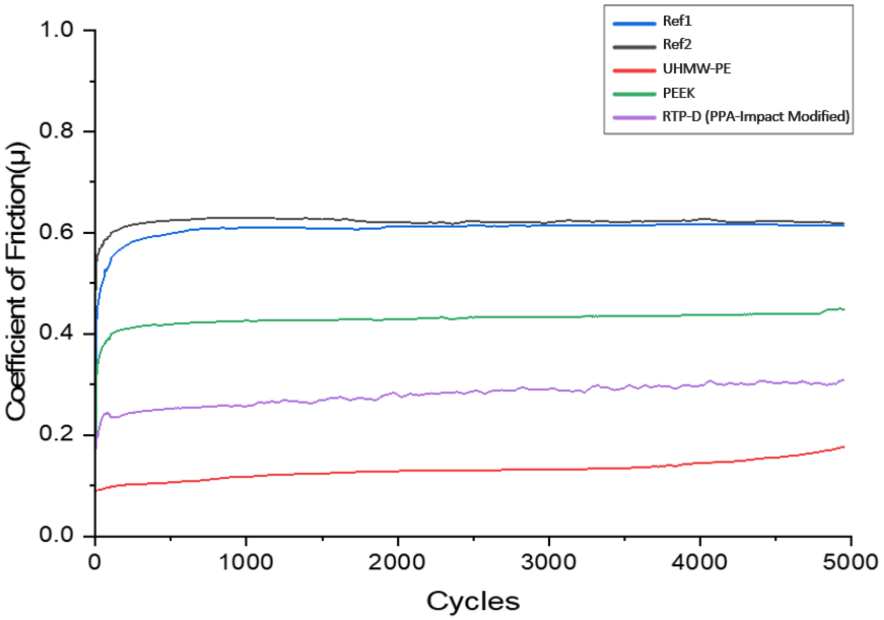

Figure 88. Pin on flat test results for polymeric reference samples (ref1 and ref2) and thermoplastic final candidates, 1Hz and 5N.

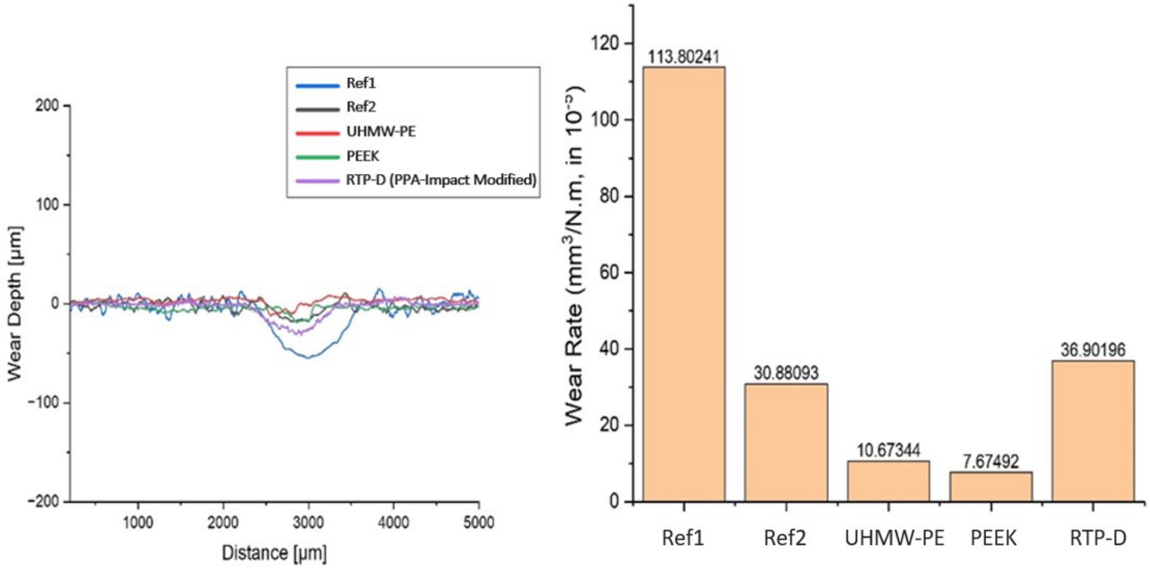

Figure 89. Wear track results after pin-onflat test using confocal microscope, for the final sample UHMWPE, PEEK, and RTP-D (PPA impact modified) in thermoplastic group.

Figure 89, presents wear depth and wear rates for selected materials, including UHMW-PE, PEEK, RTP-D, and the reference materials ref1 and ref2, following a pin-on-flat test analyzed using a confocal microscope.

However, the wear rate data highlight significant differences in material performance. Ref1 displayed the highest wear rate, indicating that it is the least wear-resistant with highest abradability. Conversely, ref2 demonstrated much lower wear rate. Both UHMW-PE and PEEK showed considerably lower wear rates than the reference materials. RTP-D, in terms of abradability, stands more abradable than ref2 lower than ref1.

The analysis Scanning Electron Microscope (SEM) images obtained from the pins after the tests offers showing material transfer presented in Figure 90 to Figure 92.

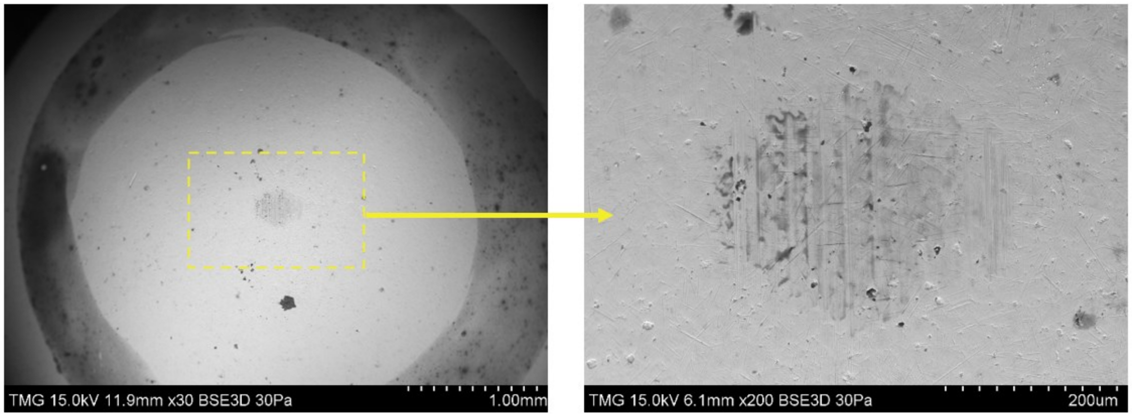

Figure 90. SEM images of the ball used in the pin-on-flat test for the PEEK sample in different magnifications.

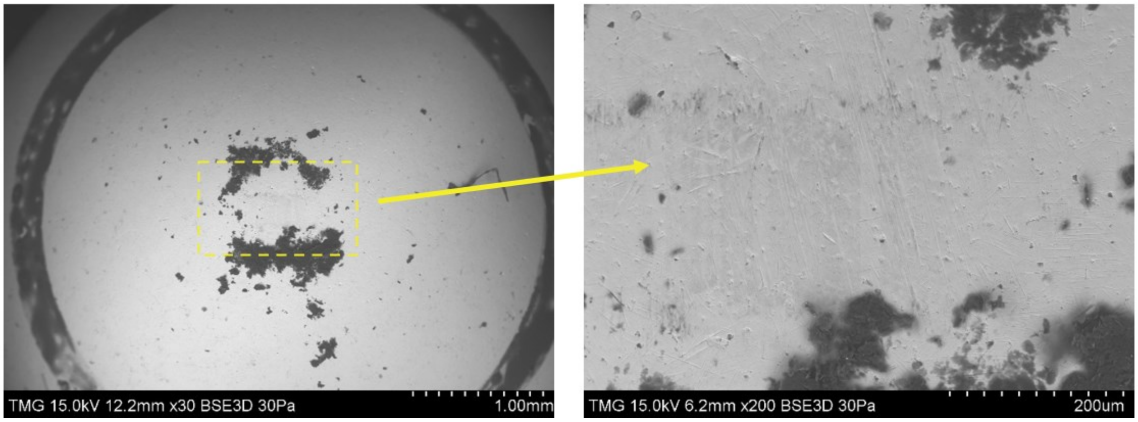

Figure 91. SEM images of the ball used in the pin-on-flat test for the RTP-D sample in different magnifications.

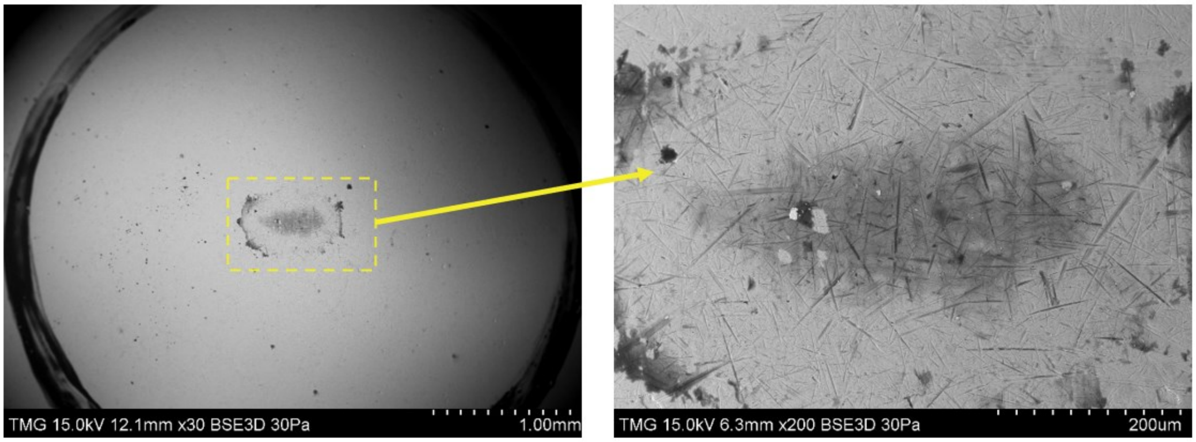

Figure 92. SEM images of the ball used in the pin-on-flat test for the UHMW-PE sample in different magnifications.

The candidate materials showed varied behaviors. The SEM images for balls after pin-on-flat test on PEEK sample indicated minimal to no scratches, showcasing excellent surface integrity under the testing conditions. In contrast, RTP-D exhibited significant material adhesion, suggesting a potential for debris accumulation that could adversely affect performance, especially in environments where maintaining surface cleanliness is critical. UHMW-PE (Ultra High Molecular Weight Polyethylene) also showed material adhesion, but to a lesser extent than RTP-D.

6.2.3 Rub Rig Test Results

The wear track results obtained from the confocal microscopy after the rub-rig test for the final thermoplastic samples are presented in Figure 93 and Figure 94.

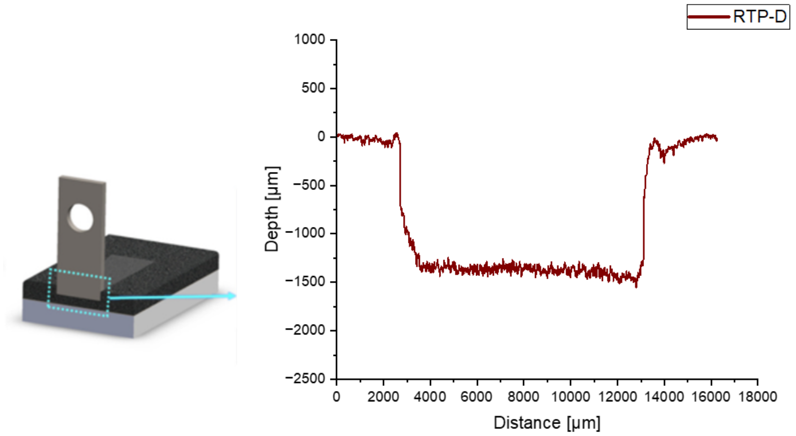

Figure 93. Wear track results after rub-rig test using confocal microscope, for the selected sample RTP-D (PPA impact modified) in thermoplastic group.

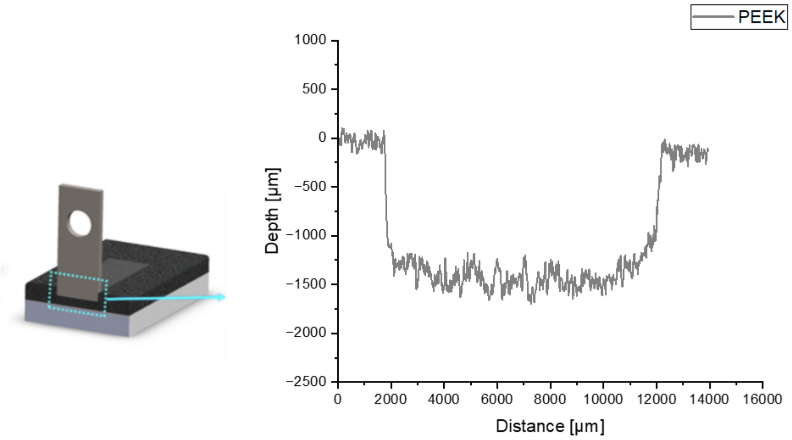

Figure 94. Wear track results after rub-rig test using confocal microscope, for the neat PEEK, selected sample in thermoplastic group.

Figure 93 shows smooth rubbed surface of RTP-D (PPA-impact modified) indicating good abradability, but Figure 94 demonstrates a rough wear track for PEEK suggests that there is potential for improvement. The performance of PEEK can be further enhanced by incorporating fillers.

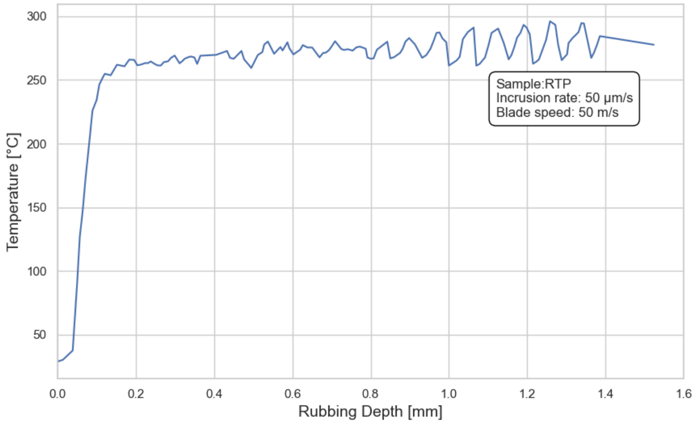

Figure 95. Temperature variation during the rub-rig test, recorded by a thermal camera, for, RTP-D (PPA impact modified) sample.

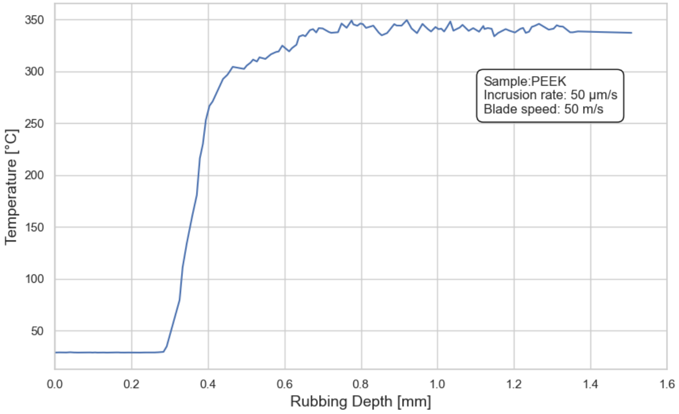

Figure 96. Temperature variation during the rub-rig test, recorded by a thermal camera, for, neat PEEK sample.

For both samples the rubbing temperature increases as a function of rubbing depth. For the RTP-D (PPA impact modified) sample, a temperature variation was observed with a maximum temperature of 291℃ (Figure 95). This result highlights the material's significantly higher sensitivity to the frictional heat generated during the test, same as for PEEK sample (Figure 96) with 339℃.

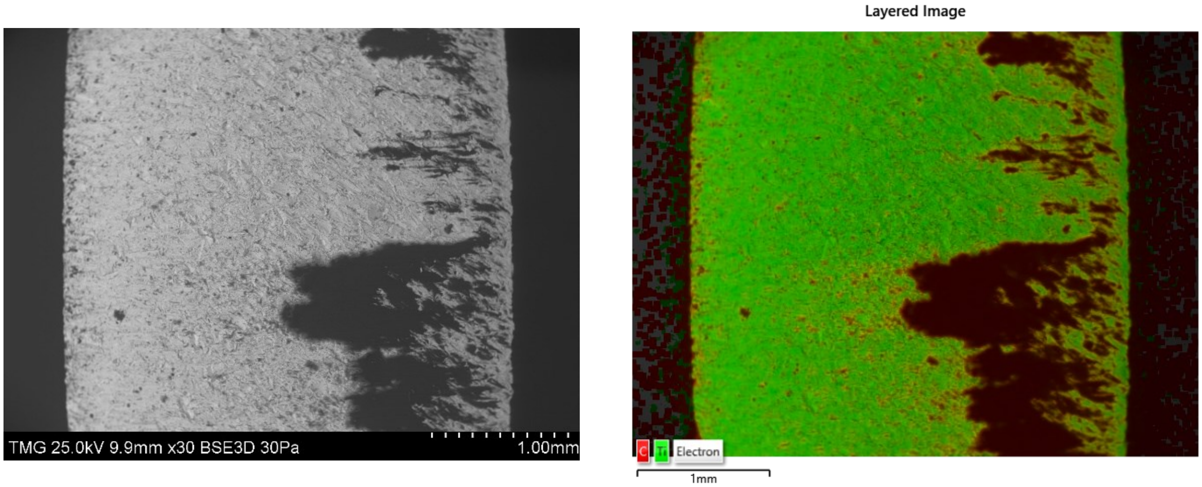

Figure 97. Materials that adhered to the top blade after the rub rig test for sample PEEK.

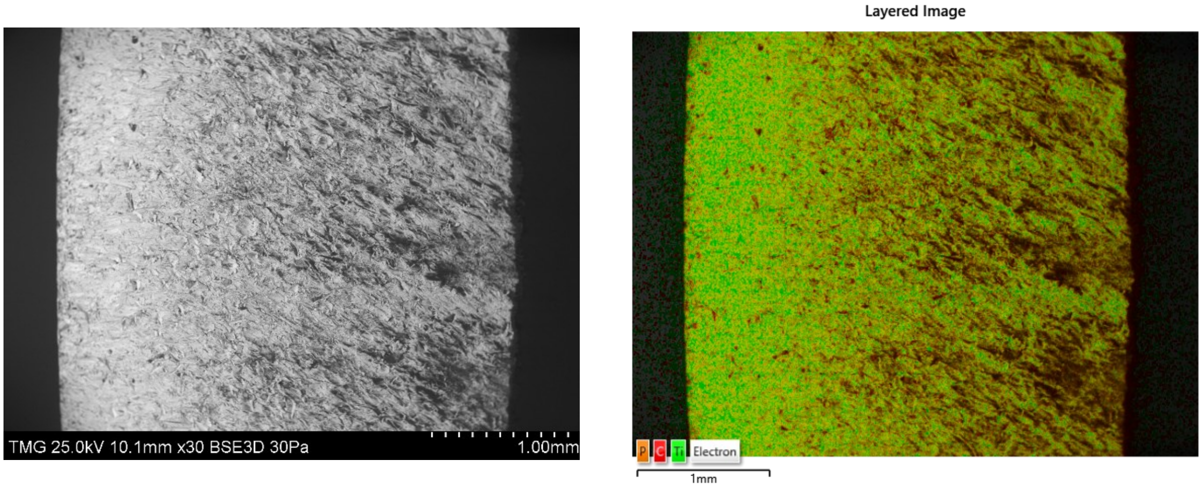

Figure 98. Materials that adhered to the top blade after the rub rig test for sample RTP-D.

The PEEK sample demonstrates noticeable material adherence to the blade, as shown in Figure 97, although it is less than that observed with the ref2 sample (Figure 84). Meanwhile, the RTP-D (PPA-impact-modified) sample exhibits the least amount of material transfer to the blade.

In the context of abradable coatings, the ideal characteristic is that the coating allows for easy cutting by the blade with minimal resistance. Both, the ref1 and RTP-D samples displayed properties indicative of lower wear resistance, which is advantageous for abradable coatings since it facilitates smoother blade interaction.

For effective engine performance, it is crucial that minimal debris adheres to the blade as this can impact engine efficiency and operation. Both the ref1 and RTP-D samples have demonstrated finer and less adhesion, contributing to cleaner blade surfaces and reducing potential for engine wear or damage.

Conversely, the ref2 and PEEK samples show a higher wear rate, characterized by more substantial and coarser debris adhesion. This characteristic might not be ideal for applications that require low wear resistance, as it could lead to quicker degradation of the coating and increase the frequency of maintenance needs.

The differences observed in the SEM images of the balls after the pin-on-flat test and the SEM images of the blade after rub rig test for the PEEK sample, can be attributed to the contrasting mechanisms of the two tests. The pin-on-flat test, primarily involving rubbing, generates friction that typically leads to less material transfer and lower wear rates. In contrast, the rub rig test involves cutting through the material, which typically results in higher wear rates and more substantial material transfer. This distinction in testing methods and their mechanical interactions explains the differing outcomes observed in the SEM images.

6.2.4 Performance Comparison: Rub Rig Tests

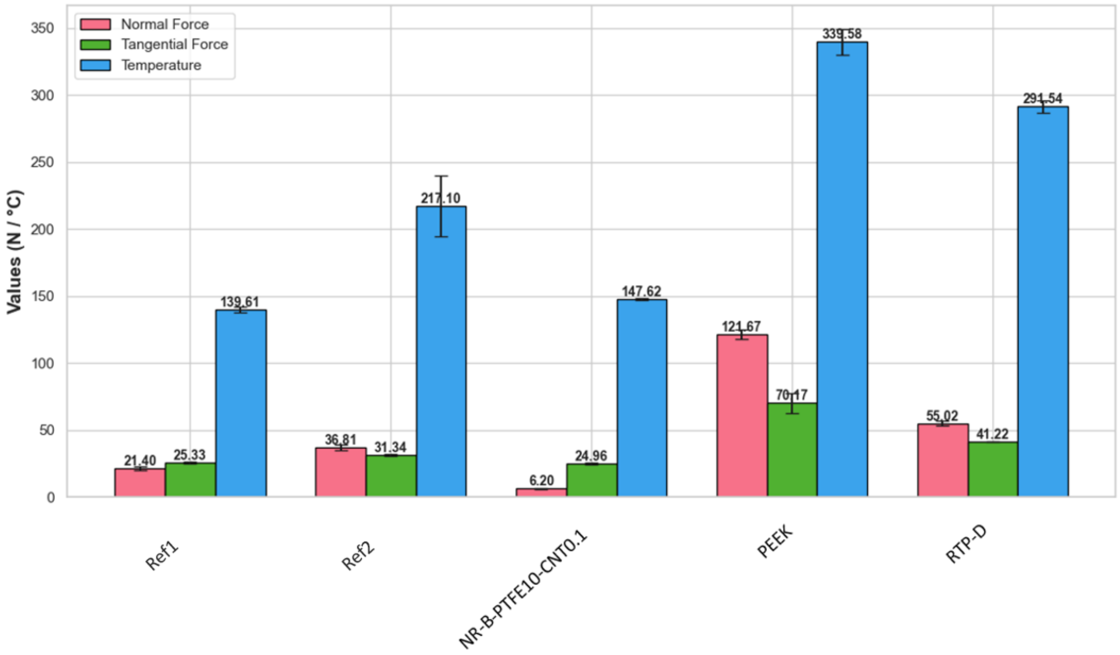

Figure 99. Bar graph of maximum reaction forces and maximum rubbing temperature of final candidates during rub rig abradability test.

In the rub rig tests, temperatures and reaction forces were measured for candidates and reference material coatings under abrasion. Figure 99 highlights the maximum reaction forces and maximum temperatures while reaching the maximum rubbing depth. Notably, the RTP-D (PPA-impact modified) and PEEK samples exhibited higher temperature compared to the NR-B-PTFE 10-CNT 0.1 coating. This increase correlates with the reaction forces observed, where the PEEK and RTP-D samples showed the highest maximum normal and tangential forces. It has been recorded for them the highest maximum temperatures against reference materials and the final thermoset candidate. This is due to that despite variations in thermal conductivity and applied forces, higher friction forces led to increased temperatures. As this test indicates the real application, lower force correlates with lower force on the blade. Therefore, thermoplastic candidates may require improvements, whereas the final thermoset candidate maintained a low and comparable maximum temperature and exhibited the lowest forces compared to reference materials.

Chapter 7

Conclusion

7. Conclusion

This investigation assessed the erosion resistance and abradability of thermoset and thermoplastic materials as abradable coatings for potential use in aircraft engine fan core and Low-Pressure Compressor stage. Among the tested materials, an epoxy resin mix of Epon 828 and Epikure 3164 showed outstanding performance in erosion resistance, exhibiting low erosion rates and ductile erosion patterns at low and 90° impingement angles. This highlights its appropriateness as a clearance control material.

The study also found promising outcomes with certain thermoplastics, specifically PEEK and UHMW-PE, which demonstrated excellent erosion resistance, indicating their viability for erosive conditions within aerospace engines. PEEK as a preferable choice for abradable coating applications at temperatures around 90°C was selected, due to its superior chemical resistance and stability at high temperatures, along with its high glass transition temperature (Tg) of 143°C. In contrast, HMWPE might encounter performance issues at these temperatures due to its lower Tg (ranging from -125°C to -100°C), making it less suitable for high-temperature applications but adequate for cooler conditions at the engine's initial stages.

The study also conducted an analysis of the effects of various fillers on the erosion resistance and abradability of polymer coatings. It examined seven fillers—Graphite, Silicone Powder, PTFE Powder, CNT, Milled Carbon Fiber, Aramid Fiber (Kevlar), and HGM (Hollow Glass Microspheres)—each incorporated into an epoxy resin matrix at two concentrations. These composite materials were then compared against two commercially available epoxy based abradable materials.

The findings emphasize the importance of selecting the right fillers and concentrations to enhance the properties of polymeric coatings. Notably, CNT and Milled Carbon Fiber improved erosion resistance, while PTFE was most effective in reducing friction, thereby enhancing the coatings' abradability. These improvements are vital for the enhanced performance and longevity of the parts, where erosion resistance and low friction are essential.

The composite formulation containing 10% PTFE and 0.1% CNT in the epoxy matrix of Epon 828 and Epikure 3164 displayed superior performance, with a notably lower erosion rate and reduced friction coefficient compared to commercial benchmarks. This presents a promising approach for extending the operational life and efficiency of engine components. However, the erosion resistance behavior of this sample was mostly attributable to the resin selection, as incorporating CNT into this specific resin did not seem to improve erosion resistance as expected.

Additionally, the composite sample named RTP-D with a PPA matrix, demonstrated a low erosion rate and an acceptable coefficient of friction, producing smaller and finer debris during the rub rig test, indicating its suitability for the intended application. However, it caused a high application force to the blade and significantly increased the temperature during the rub-rig test, which could present challenges in practical applications.

In conclusion, this study highlights the importance of carefully choosing and balancing filler concentrations to enhance the mechanical and tribological properties of polymeric coatings. The findings contribute valuable knowledge towards developing durable polymeric coatings suitable for aerospace applications, which are anticipated to improve engine performance and efficiency while lowering maintenance demands.

7.1 Future Works

Future work will focus on refining these formulations further, emphasizing the evaluation of their performance under high-temperature conditions to understand the impact of temperature on their practical applications. Additionally, the next phase will involve examining the adhesion properties of these materials through pull-off tests to assess their bond strength. Another critical step will be testing the materials' sensitivity to various fluids to evaluate their chemical resistance and compatibility in diverse environments. Finally, large-scale abradability tests over extended periods will be conducted to better simulate the application of these materials.

References

[1] N. Karak, *Fundamentals of polymers: raw materials to finish products*. PHI Learning Pvt. Ltd., 2009.

[2] M. Bounazef, S. Guessasma, and B. A. Saadi, "The wear, deterioration and transformation phenomena of abradable coating BN–SiAl–bounding organic element, caused by the friction between the blades and the turbine casing," *Mater Lett*, vol. 58, no. 27–28, pp. 3375–3380, 2004.

[3] Mike Arnot, "The Most Fascinating Machines Ever Made: How Jet Engines Work," The Points Guy.

[4] N.-M. Barkoula and J. Karger-Kocsis, "Review processes and influencing parameters of the solid particle erosion of polymers and their composites," *J Mater Sci*, vol. 37, pp. 3807–3820, 2002.

[5] A. Patnaik, A. Satapathy, N. Chand, N. M. Barkoula, and S. Biswas, "Solid particle erosion wear characteristics of fiber and particulate filled polymer composites: A review," *Wear*, vol. 268, no. 1–2, pp. 249–263, 2010.

[6] N. Miyazaki, "Solid particle erosion of composite materials: A critical review," *J Compos Mater*, vol. 50, no. 23, pp. 3175–3217, 2016.

[7] D. Acar, M. H. Danesh, and Ö. N. Cora, "Effect of Process Parameters on the Solid Particle Erosion Resistance of Transparent Materials," *Tribology in Industry*, vol. 45, no. 4, p. 604, 2023.

[8] H. Ashrafizadeh, A. McDonald, and P. Mertiny, "Erosive and abrasive wear resistance of polyurethane liners," *Aspects of polyurethanes*, vol. 6, p. 131, 2017.

[9] S. Demski, K. Dydek, K. Bartnicka, K. Majchrowicz, R. Kozera, and A. Boczkowska, "Introduction of SWCNTs as a method of improvement of electrical and mechanical properties of CFRPs based on thermoplastic acrylic resin," *Polymers (Basel)*, vol. 15, no. 3, p. 506, 2023.

[10] R. I. Trezona, M. J. Pickles, and I. M. Hutchings, "A full factorial investigation of the erosion durability of automotive clearcoats," *Tribol Int*, vol. 33, no. 8, pp. 559–571, 2000.

[11] Z. U. Nisa, L. K. Chuan, B. H. Guan, S. Ayub, and F. Ahmad, "Anti-Wear and Anti-Erosive Properties of Polymers and Their Hybrid Composites: A Critical Review of Findings and Needs," *Nanomaterials*, vol. 12, no. 13, p. 2194, 2022.

[12] H. Guo, F. Li, S. Wen, H. Yang, and L. Zhang, "Characterization and quantitative analysis of crack precursor size for rubber composites," *Materials*, vol. 12, no. 20, p. 3442, 2019.

[13] N.-M. Barkoula, J. Gremmels, and J. Karger-Kocsis, “Dependence of solid particle erosion on the cross-link density in an epoxy resin modified by hygrothermally decomposed polyurethane,” *Wear*, vol. 247, no. 1, pp. 100–108, 2001.

[14] M. Fernández-Álvarez, F. Velasco, A. Bautista, and J. Abenojar, “Effect of silica nanoparticles on the curing kinetics and erosion wear of an epoxy powder coating,” *Journal of Materials Research and Technology*, vol. 9, no. 1, pp. 455–464, 2020.

[15] N. Song and A. Benmeddour, “Erosion resistant hydrophobic coatings for passive ice protection of aircraft,” *Applied Sciences*, vol. 12, no. 19, p. 9589, 2022.

[16] İ. Özen, H. Gedikli, and B. Öztürk, “Improvement of solid particle erosion resistance of helicopter rotor blade with hybrid composite shield,” *Eng Fail Anal*, vol. 121, p. 105175, 2021.

[17] S. M. Kulkarni and Kishore, “Influence of matrix modification on the solid particle erosion of glass/epoxy composites,” *Polymers and polymer composites*, vol. 9, no. 1, pp. 25–30, 2001.

[18] K. Shahapurkar *et al.*, “Effect of crump rubber on the solid particle erosion response of epoxy composites,” *J Appl Polym Sci*, vol. 139, no. 2, p. 51470, 2022.

[19] L. BAO, D. QIAN, G. WANG, and K. KEMMOCHI, “Solid Particle Erosion Characteristics of Composites Filled with Nano Carbon Fibers,” *Journal of textile engineering*, vol. 58, no. 2, pp. 13–19, 2012.

[20] D. Pinisetty, V. C. Shunmugasamy, and N. Gupta, “Hollow glass microspheres in thermosets—epoxy syntactic foams,” in *Hollow glass microspheres for plastics, elastomers, and adhesives compounds*, Elsevier, 2015, pp. 147–174.

[21] K.-T. Lau, S.-Q. Shi, L.-M. Zhou, and H.-M. Cheng, “Micro-hardness and flexural properties of randomly-oriented carbon nanotube composites,” *J Compos Mater*, vol. 37, no. 4, pp. 365–376, 2003.

[22] M. J. Biercuk, M. C. Llaguno, M. Radosavljevic, J. K. Hyun, A. T. Johnson, and J. E. Fischer, “Carbon nanotube composites for thermal management,” *Appl Phys Lett*, vol. 80, no. 15, pp. 2767–2769, 2002.

[23] T. Kuzumaki, O. Ujiie, H. Ichinose, and K. Ito, “Mechanical characteristics and preparation of carbon nanotube fiber-reinforced Ti composite,” *Adv Eng Mater*, vol. 2, no. 7, pp. 416–418, 2000.

[24] S. C. Shit and P. Shah, “A review on silicone rubber,” *National academy science letters*, vol. 36, no. 4, pp. 355–365, 2013.

[25] Y.-Q. Tong, W. Li, Q.-S. Shi, L. Chen, and G.-J. Yang, “Self-lubricating epoxy-based composite abradable seal coating eliminating adhesive transfer via hierarchical design,” *J Mater Sci Technol*, vol. 104, pp. 145–154, 2022.

[26] M. W. Keller, S. R. White, and N. R. Sottos, “Torsion fatigue response of self-healing poly (dimethylsiloxane) elastomers,” *Polymer (Guildf)*, vol. 49, no. 13–14, pp. 3136–3145, 2008.

[27] X. Haijun, N. Zhang, L. U. Bin, L. Cheng, and H. Weirong, “Investigation of high-speed abrasion behavior of an abradable seal rubber in aero-engine fan application,” *Chinese Journal of Aeronautics*, vol. 30, no. 4, pp. 1615–1623, 2017.

[28] V. Kumar, M. N. Alam, A. Manikkavel, M. Song, D.-J. Lee, and S.-S. Park, “Silicone rubber composites reinforced by carbon nanofillers and their hybrids for various applications: A review,” *Polymers (Basel)*, vol. 13, no. 14, p. 2322, 2021.

[29] P. S. Sarath *et al.*, “Fabrication of exfoliated graphite reinforced silicone rubber composites-Mechanical, tribological and dielectric properties,” *Polym Test*, vol. 89, p. 106601, 2020.

[30] P. S. Sarath, G. Moni, J. J. George, J. T. Haponiuk, S. Thomas, and S. C. George, “A study on the influence of reduced graphene oxide on the mechanical, dynamic mechanical and tribological properties of silicone rubber nanocomposites,” *J Compos Mater*, vol. 55, no. 15, pp. 2011–2024, 2021.

[31] A. P. Harsha, U. S. Tewari, and B. Venkatraman, “Solid particle erosion behaviour of various polyaryletherketone composites,” *Wear*, vol. 254, no. 7–8, pp. 693–712, 2003.

[32] T. Sınmazçelik and İ. Taşkıran, “Erosive wear behaviour of polyphenylenesulphide (PPS) composites,” *Mater Des*, vol. 28, no. 9, pp. 2471–2477, 2007.

[33] M. Dong *et al.*, “Enhanced solid particle erosion properties of thermoplastic polyurethane-carbon nanotube nanocomposites,” *Macromol Mater Eng*, vol. 304, no. 5, p. 1900010, 2019.

[34] S. Arjula, A. P. Harsha, and M. K. Ghosh, “Solid-particle erosion behavior of high-performance thermoplastic polymers,” *J Mater Sci*, vol. 43, pp. 1757–1768, 2008.

[35] M. Dong *et al.*, “Thermoplastic polyurethane-carbon black nanocomposite coating: Fabrication and solid particle erosion resistance,” *Polymer (Guildf)*, vol. 158, pp. 381–390, 2018.

[36] N. Miyazaki and T. Hamao, “Effect of interfacial strength on erosion behavior of FRPs,” *J Compos Mater*, vol. 30, no. 1, pp. 35–50, 1996.

[37] N. Miyazaki and N. Takeda, “Solid particle erosion of fiber reinforced plastics,” *J Compos Mater*, vol. 27, no. 1, pp. 21–31, 1993.

[38] N. Miyazaki and T. Hamao, “Solid particle erosion of thermoplastic resins reinforced by short fibers,” *J Compos Mater*, vol. 28, no. 9, pp. 871–883, 1994.

[39] K. Bertuol, F. Rivadeneira, R. B. Nair, B. Barnett, C. Moreau, and P. Stoyanov, “Influence of hBN on the abradable performance of AlSi-based coatings: Bridging the gap between tribological assessment and abradability testing,” *Surf Coat Technol*, p. 131060, 2024.

[40] B. Bhushan, *Principles and applications of tribology*. John wiley & sons, 2013.

[41] Sartorius AG, "User's manual for Sartorius YDK01, YDK01-0D, YDK01B, YDK01LP, YDK01MS, YDK02MS Density Determination Kit."

[42] K. K. Chawla, *Composite materials: science and engineering*, vol. 1. Springer, 2012.